Development of Silica-based Aerogels for Super-insulating Glazing Application(Dissertation_全文)

AUTHOR(S):

Kugimiya, Kazuma

CITATION:

Kugimiya, Kazuma. Development of Silica-based Aerogels for Super-insulating Glazing Application. 京都大学, 2011, 博士(工学)

ISSUE DATE:

2011-03-23

URL:

https://doi.org/10.14989/doctor.k16098

Development of Silica-based Aerogels for Super-insulating Glazing Application

Kazuma Kugimiya

2011

Contents

GENERAL INTRODUCTION

Energy conservation in private households or industry is a crucial parameter in reducing the consumption of primary energy carrier, causing a reduced output of greenhouse gases such as carbon dioxide. One key parameter for reducing the energy consumption for heating or cooling purpose is, for example, to improve the insulation in buildings, vehicles, heating system or refrigeration system. For industrial needs such as ships for liquid natural gas transport or the design of production furnaces, the use of high performance insulations can help to reduce the energy consumption of the system significantly.

Considering the insulation in building, window have a major influence on space heating demand and indoor environment both with respect to climate and daylight. Windows are still thermally weakest part of the thermal envelope but on the other hand allow the use of solar heat and daylight. In the continuing effort to lower the heat loss from buildings window glazing have been significantly improved. The *U*-value has been reduced by the introduction of insulating gas fillings or reducing the gas pressure and almost invisible low-E coatings to reduce heat transfer by long-wave infra-red radiation[1, 2]. In the search for further energetic improvement of window glazing, especially evacuated aerogel glazing solutions have been investigated[3-5].

Since the first preparation by Kistler in 1931[6], aerogels with a variety of chemical compositions ranging from inorganic oxides to organic cross linked polymers have been explored to date[7-11]. Aerogel is generally regarded as a transparent ultra-porous material[12]. Typically silica aerogels contain small

pores with 50 nm and high porosity higher than 90%. Owing to the small sizes (less than the mean free path of air, ~ 67 nm) and the intricate geometry of the pores, together with very low solid fractions, aerogels exhibit excellent thermal insulation properties. Low refractive index, low dielectric constant, and high specific surface area are highly important properties as well. As the skeletons that comprise their porous morphology are too thin, aerogels are brittle, and they must be dried with the utmost care by using supercritical drying, for example, to preserve their fragile pore structure. The usage of supercritical drying process leads to the increase in cost of aerogel, which confines the application field except for particular purpose such as high energy physics[13] and space science[14]. In 1985, Prakash et al. have obtained films with porosity up to 98.5 % by ambient pressure drying, for the first time [15]. In addition, highly transparent monolithic aerogels and xerogels has been prepared by Kanamori et al. using methyltrimethoxysilane as a single precursor by sol-gel in 2007[16-18]. Establishment of synthetic process for transparent monolithic aerogels by ambient pressure drying will advance to practical stage of aerogels in many fields.

In the present study, in order to improve the thermal insulating performance of the weakest part in house, the possibility of applying aerogel to the newly high performance thermal insulation window are investigated. As candidate insulating window, evacuated aerogel glazing is studied. In addition, the suitable aerogels for the application of evacuated aerogel glazing are also studied. The contents of respective chapters are summarized as follows.

In chapter 1, pressure dependence of thermal conductivities of porous material

(porous silica powder and transparent silica aerogel) were evaluated. For comparison, pressure dependence of thermal conductivity of nitrogen gas was also examined. It was clarified that the thermal conductivity of the porous ceramic material was lowered than that of simple vacuum at lower vacuum region (higher pressure), indicating the porous ceramic materials had an advantage for the application of thermal insulator.

In chapter 2, transparent aerogels were prepared using commercially available silicon oligomer and methyltrimethoxysilane precursor to examine their mechanical and optical properties. The preparation of highly transparent silica-based aerogel was successfully achieved by tuning the starting composition and appropriate treatment.

In chapter 3, thermal conductivity of silica aerogel, derived from silicon oligomer as silica precursor, as a function of density and thickness under atmospheric and evacuated condition was examined. Thermal conductivity under atmospheric and evacuated condition showed minimum value at the density of 0.14 and 0.10 $g \cdot cm^{-3}$, respectively. This shift of optimal density for minimum thermal conductivity indicated that the gaseous conduction increases with decreasing density. For evacuated aerogel as well as non-evacuated aerogel, thickness dependence of thermal conductivity was observed, which was caused by low extinction coefficient of silica aerogel.

In chapter 4, Prototypes of evacuated aerogel glazing have been assembled in a vacuum chamber and its optical and thermal property was examined. The glazing prototypes with aerogel's thickness of 10 mm had a measured *U*-value of 0.62 W/ ($m^2 \cdot K$) and optical transmittance of 64%.

In chapter 5, $EuTiO_{3-\delta}$ epitaxial thin films have been prepared on $SrTiO_3$ substrates by a pulsed laser deposition technique and their magnetic properties have been examined. By controlling the oxygen pressure and substrate temperature, $EuTiO_{3-\delta}$ films were epitaxially grown on the substrates. The resultant films exhibited ferromagnetic behavior with Curie temperature of 5 K. Such magnetic properties were similar to those for La- and Gd- substituted $EuTiO_3$ single crystal, in which the Ruderman-Kittel-Kasuya-Yoshida (RKKY) interaction between localized spins of magnetic ions brought about the ferromagnetic ordering.

In chapter 6, amorphous $EuTiO_3$ thin films have been prepared by a pulsed laser deposition method, and their structural and magnetic properties have been investigated. High-resolution transmission electron microscopy image and selected-area electron diffraction pattern as well as x-ray diffraction pattern confirmed the amorphous nature of as-deposited thin film. ^{151}Eu conversion-electron Mössbauer spectrum showed that almost all of the europium ions in the thin films were present as Eu^{2+}. The signature of a ferromagnetic-like transition was observed at around 5 K.

Reference

[1] P. W. Griffiths, P. C. Eames, T. J. Hyde, Y. Fang and B. Norton, *Journal of Solar Energy Engineering* **128** (2006), p. 199.

[2] R. E. Collins and T. M. Simko, *Solar Energy* **62** (1998), p. 189.

[3] K. Duer and S. Svendsen, *Solar Energy* **63** (1998), p. 259.

[4] K. I. Jensen, *Journal of Non-Crystalline Solids* **145** (1992), p. 237.

[5] K. I. Jensen, J. M. Schultz and F. H. Kristiansen, *Journal of Non-Crystalline Solids* **350** (2004), p. 351.

[6] S. S. Kistler, *Nature* **127** (1931), p. 741.

[7] N. Hüsing and U. Schubert, *Journal of Sol-Gel Science and Technology* **8** (1997), p. 807.

[8] N. Hüsing, U. Schubert, R. Mezei, P. Fratzl, B. Riegel, W. Kiefer, D. Kohler and W. Mader, *Chemistry of Materials* **11** (1999), p. 451.

[9] K.-H. Lee, S.-Y. Kim and K.-P. Yoo, *Journal of Non-Crystalline Solids* **186** (1995), p. 18.

[10] M. A. B. Meador, E. F. Fabrizio, F. Ilhan, A. Dass, G. Zhang, P. Vassilaras, J. C. Johnston and N. Leventis, *Chemistry of Materials* **17** (2005), p. 1085.

[11] B. M. Novak, D. Auerbach and C. Verrier, *Chemistry of Materials* **6** (1994), p. 282.

[12] J. Fricke and A. Emmerling, *Journal of the American Ceramic Society* **75** (1992), p. 2027.

[13] T. Sumiyoshi, I. Adachi, R. Enomoto, T. Iijima, R. Suda, M. Yokoyama and H. Yokogawa, *Journal of Non-Crystalline Solids* **225** (1998), p. 369.

[14] P. Tsou, *Journal of Non-Crystalline Solids* **186** (1995), p. 415.

[15] S. S. Prakash, C. J. Brinker, A. J. Hurd and S. M. Rao, *Nature* **374** (1995), p. 439.

[16] K. Kanamori, M. Aizawa, K. Nakanishi and T. Hanada, *Advanced Materials* **19** (2007), p. 1589.

[17] K. Kanamori, M. Aizawa, K. Nakanishi and T. Hanada, *Journal of Sol-Gel Science and Technology* **48** (2008), p. 172.

[18] K. Kanamori, K. Nakanishi and T. Hanada, *Journal of the Ceramic Society of Japan* **117** (2009), p. 1333.

CHAPTER 1

Thermal conductivity of porous materials

1. Mechanism of heat transfer

The physics of the total heat transfer through an insulation material are well known. The mechanism of heat transfer is shown in Figure.1. The total density of heat flow rate in such porous materials can be explained by four different heat transfer processes; heat transfer q_r (W/m^2) via radiation, heat transfer q_{cd} via conduction of the solid skeleton of the core and heat transfer via the gas inside the material. This last mentioned transfer via the internal gasses can be divided in heat transfer q_g due to gas conduction and heat transfer q_{cv} due to gas convection. The thermal transport through a material according to the thermal gradient can be quantified by the thermal conductivity λ_{tot} (W/(m·K)). A standard simplified approach for this λ_{tot} is to assume that the value represents a sum of single values which describe on their own one of the above mentioned ways of thermal transfer, but they have to be considered simultaneously to be correct. The total thermal conductivity λ_{tot} can be expressed as follows:

$$\lambda_{tot} = \lambda_g + \lambda_{cd} + \lambda_{cv} + \lambda_{rad} \quad (1),$$

where λ_g is the gas conduction within the material pores and λ_{cd} is the solid conduction within the material skeleton, λ_{cv} is the air and moisture convection within the pore, and λ_{rad} is the radiation transfer between internal pore surfaces, respectively. For building insulation materials, all these parameters should be minimized to result in a low overall thermal conductivity λ_{tot} of the material in

general.

The most effective reduction of the gas thermal conduction λ_g appears in a theoretical perfect vacuum, as proposed by James Dewar in 1892. Here, the λ_g achieves its limit value of 'zero'. A vacuum can be used to reduce the thermal conductivity of most traditional insulation materials, while the gaseous thermal conductivity λ_g of an evacuated material will not only be a function of the applied pressure but also from the core materials characteristics. The gaseous thermal conductivity of a porous medium at lower pressure is determined by the number of gas molecules (determined by the particle frequency of the vacuum or the internal pressure) as well as by the number of obstructions for the gas on the way from the hot to the cold side. While reducing the gas pressure in a material, the gas conductivity of the non-convective gas remains almost unaffected until the mean free path of the gas molecules reaches values in the same order of size as the largest pores in the medium. When the pore diameter of the material becomes less than the average free length of path of gas molecules, the air molecules will only collide with the pore surfaces without transferring energy by this elastic impact.

2. Measurement of thermal conductivity

Accurate characterization of heat insulation in insulating materials is important. Generally, there are two standardized methods available for characterizing the thermal conductivity or the thermal resistance of insulating materials. The heat flow meter technique is a fast and reliable tool for thermal conductivity

measurement method around room temperature. However, the system requires a standard material for calibrating the built-in heat flux transducers. Therefore, it is not an absolute testing technique. The guarded hot plate overcomes this problem. No calibration is required as long as the uncertainty of the components and measurement devices employed stays within a certain range.

Figure 2 shows the figure of the guarded hot plate apparatus [1]. In a guarded hot plate system, an electrically heated metallic plate (hot plate) is sandwiched between two specimens of the same material (symmetrical operation). The hot plate is surrounded by a guard ring which is controlled to the same temperature as the hot plate and therefore prevents radial heat transfer laterally from the hot plate. Placed above the upper specimen and below the lower specimen are two more heated metallic plates (called auxiliary heaters or cold plates). During a test, a well defined temperature difference is created between the hot plate and the cold plate. The entire plate stack is surrounded by a sectional furnace. The furnace is controlled in such a way that it simulates a comparable temperature profile as occurring in the plate stack. This additionally avoids radial heat loss from the plate stack. If the distance between the plates (thickness of the specimens) and the power input into the hot plate under stationary conditions are known, the thermal conductivity is described as

$$\lambda = \frac{-0.5 \cdot Q \cdot L}{A \cdot \Delta T} \qquad (2),$$

where Q is heat flow through the meter area of the specimens, A is meter area normal to direction of heat flow, ΔT is temperature difference across specimens,

L is the thickness of specimens. The plate stack and the furnace are placed in a vacuum-tight container, allowing measurements to be carried out under vacuum or well-defined oxidizing or inert atmospheres.

3. Thermal conductivity of porous material under the evacuated condition

The porous silica powder and transparent silica aerogel was purchased from Suzuki Yushi Industrial Co., Ltd. and Panasonic Electric works Co., Ltd., respectively.

Microstructure of the porous ceramics materials was investigated by Field Emission scanning electron microscopy (FE-SEM) observation (SU8000, HITACHI) without coating metal at a low accelerating voltage. The porous ceramics powder was subjected to grinding by planetary ball mill for 10 minutes. For silica aerogel, the roughly crushed specimen was performed by SEM observation. The textual properties of porous ceramics materials such as BET surface area, pore volume and average pore diameter were investigated by a surface area analyzer (Quantachrome, AUTOSORB-1). The specimens were initially degassed at 150˚C for 2 hours to remove the adsorbed species and the N_2 adsorption isotherms were obtained at -196˚C. Thermal conductivities of porous silica powders and monolithic aerogels were measured with an evacuable guarded hot plate apparatus GHP 456/3/1 Titan (NETZCH). Each measurement was performed at a temperature difference of 10 K and measurement temperature of 25 ˚C in the pressure range from 1 Pa to

atmospheric pressure (10^5 Pa).

The low magnification SEM image for porous silica powder is shown in Figure 3(a). The particle size of silica powder was around 5 μm and the particle with the extremely large and small particle size was not observed. One can see that the particles have the well-defined spherical shape with smooth surface. Figure 3(b) shows the high magnification SEM images of the crushed porous silica powder. The SEM images indicated that the pore structure was observed not only at the surface of the powder but also inside the powder and the silica powder has the open and continuous pore structure with the pore diameter of approximately 10 nm. This pore size is in good agreement with the result of nitrogen adsorption, 7 nm, as shown in Figure 3(c). BET surface area of silica powder is 460 m^2 /g and pore volume is 0.617 cm^3 /g.

Figure 4(a) shows outlook of a monolithic silica aerogel. The bulk density of the aerogel was 0.11 g/cm^3, which was calculated from their mass to volume ratios. High magnification SEM image of silica aerogel is shown in Figure 4 (b). The aerogel was composed of intricate silica network on the orders of nanometers and nano-pore of about 20 nm in diameter. Figure 4(c) shows the pore size distribution of silica aerogel. The average pore size is approximately 20 nm and sharp and narrow pore size distribution is obtained. The resultant aerogel shows high BET surface area of 665 m^2/g and high pore volume of 3.21 cm^3/g.

Figure 5 depicted the gas pressure (vacuum) dependence of the apparent thermal conductivity λ of porous silica powder and silica aerogel. For comparison, thermal conductivity of nitrogen gas is also shown. In high

vacuum region, the thermal conductivity of nitrogen gas is almost zero, however, the thermal conductivity gradually increased with increasing the gas pressure at the pressure around 1 Pa and saturated at approximately 10^2 Pa. The saturated value thermal conductivity of nitrogen gas was 0.026 W/ (m·K), which was in good agreement of the reference data [2]. The behavior of pressure dependence of the thermal conductivity at the pressure from 1 Pa to 100 Pa is attributed that the mean free path of the gas molecule is comparable with the sample thickness.

The apparent thermal conductivity, λ, of silica powder rapidly decreased at the pressures from atmospheric to 1000 Pa, while at lower pressure than 1000 Pa, significant change was not observed. As for aerogel, apparent thermal conductivity was constant at the pressure below 10^4 Pa. The thermal conductivity of the porous powder and aerogel was lowered than that of simple vacuum at lower vacuum region (higher gas pressure). It indicates the porous ceramic materials had an advantage for the application of thermal insulator.

Apparent thermal conductivity can be expressed by;

$$\lambda = \lambda_{evac} + \lambda_{G0} / (1+p_{1/2}/p_G) \quad (3),$$

where λ_{evac} is the thermal conductivity of the evacuated specimen (for example, gas pressure of 1 Pa), λ_{G0} is the thermal conductivity of still nitrogen gas, $p_{1/2}$ is the gas pressure, at which the gaseous conductivity is equal to $\lambda_{G0}/2$. $P_{1/2}$ is inversely proportional to the pore width Φ and, for air, is defined as follows;

$$p_{1/2} /(\text{mbar}) \approx 230 /(\Phi/\mu\text{m}). \quad (4)$$

From equation (4) and Figure 4, the pore width Φ of porous silica powder is estimated to be approximately 3 μm. The average grain size of this powder is

approximately 5 μm, the grain space is expected to be a few μm. This grain space shows good accordance with the pore width among silica powders presumed by the pressure dependence of thermal conductivity. When it comes to aerogel, inadequate saturated thermal conductivity of aerogel even at an atmospheric pressure allowed us not to estimate the pore width of aerogel with high accuracy. However, according to the presumed thermal conductivity of the resultant data of thermal conductivity, the pore width is expected to be a few dozen nanometers, which is the good agreement with the pore width from the nitrogen adsorption measurement and SEM observation. This good agreement of pore width between the data from vacuum dependence of thermal conductivity and the nitrogen adsorption measurement for silica powder and aerogel indicates that the equation (4) is quantitatively-correct and the onset pressure, at which thermal conductivity increased dramatically, is higher (lower vacuum) for the substance with smaller pore size. Vacuum insulation panel is seemed to be prospective to increase the thermal conductivity in the long term use because of penetration of the gas molecule through the laminate film or at the sealing faces. Therefore, it is desirable that the onset pressure at which the thermal conductivity increased is high, and then, the substance with smaller pore size is suitable for the vacuum insulation panel.

4. Conclusion

Thermal conductivity for porous silica powder and transparent silica aerogel as a function of gas pressure were evaluated. It was clarified that the thermal

conductivity of the porous ceramic material was lowered than that of simple vacuum at lower vacuum region (higher gas pressure), indicating the porous ceramic materials had an advantage for the application of thermal insulator.

Reference

[1] J. Bluum, T. Denner and Y. Shinoda, Proc. Of 28th Japan Symposium on thermophysical properties (2008) 85

[2] R. A. Perkins, H. M. Roder and C. A. Nieto de Castro, J. Res. NIST 96 (1991) 247

	λ_g: Thermal conduction by gas molecules
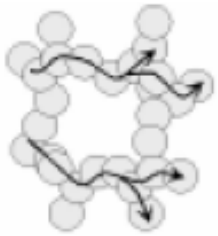	λ_{cd}: Thermal conduction through the solid
	λ_{cv}: Thermal conduction by gas flow
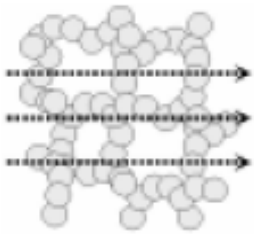	λ_{rad}: Thermal radiation

Figure 1: Mechanism of heat transfer through the porous materials.

(a)

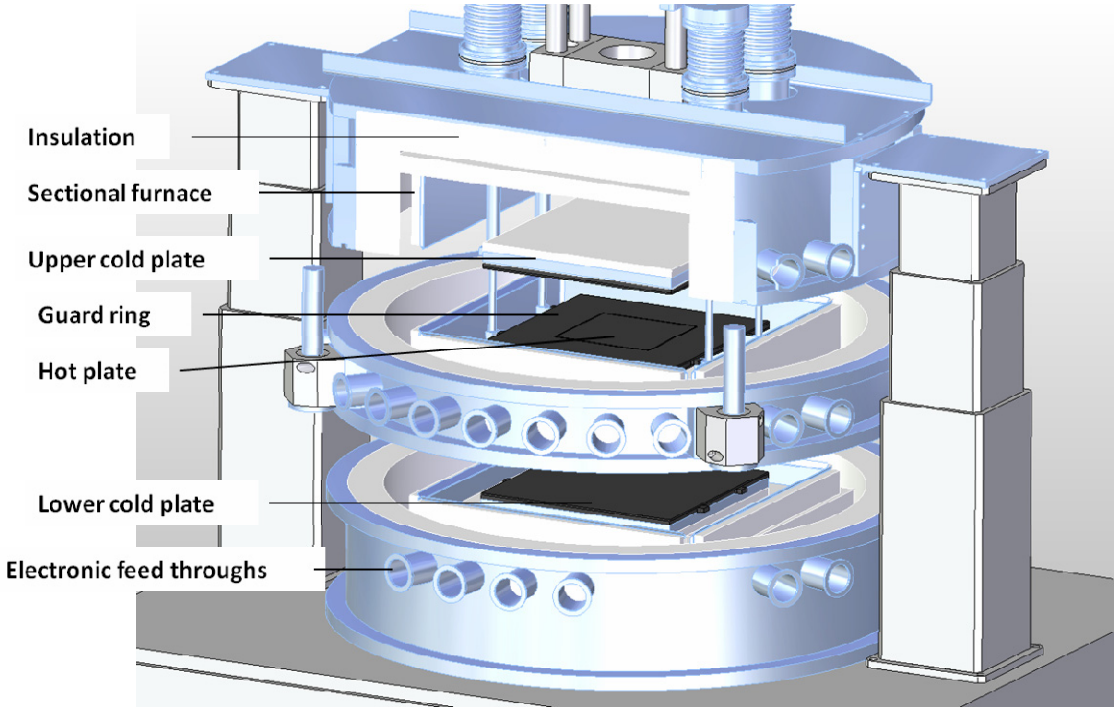

(b)

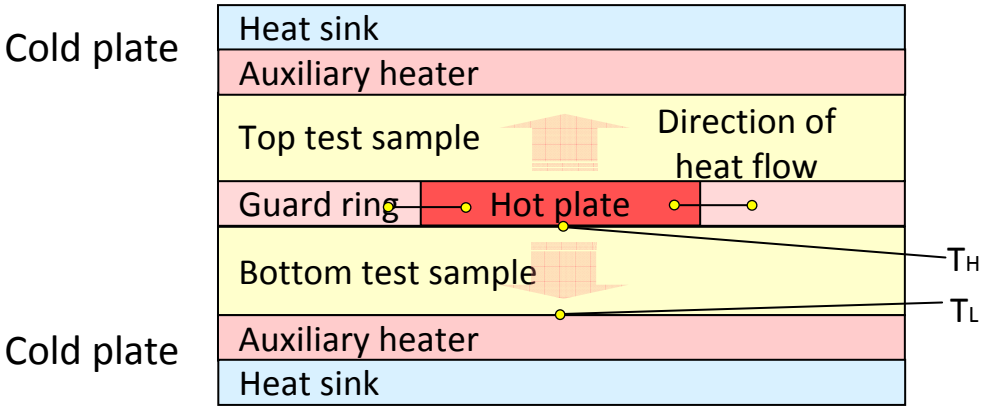

Figure 2: Picture of the equipment (a) and schematic drawing of Guarded Hot Plate method (b) to measure thermal conductivity of porous ceramic powders and materials.

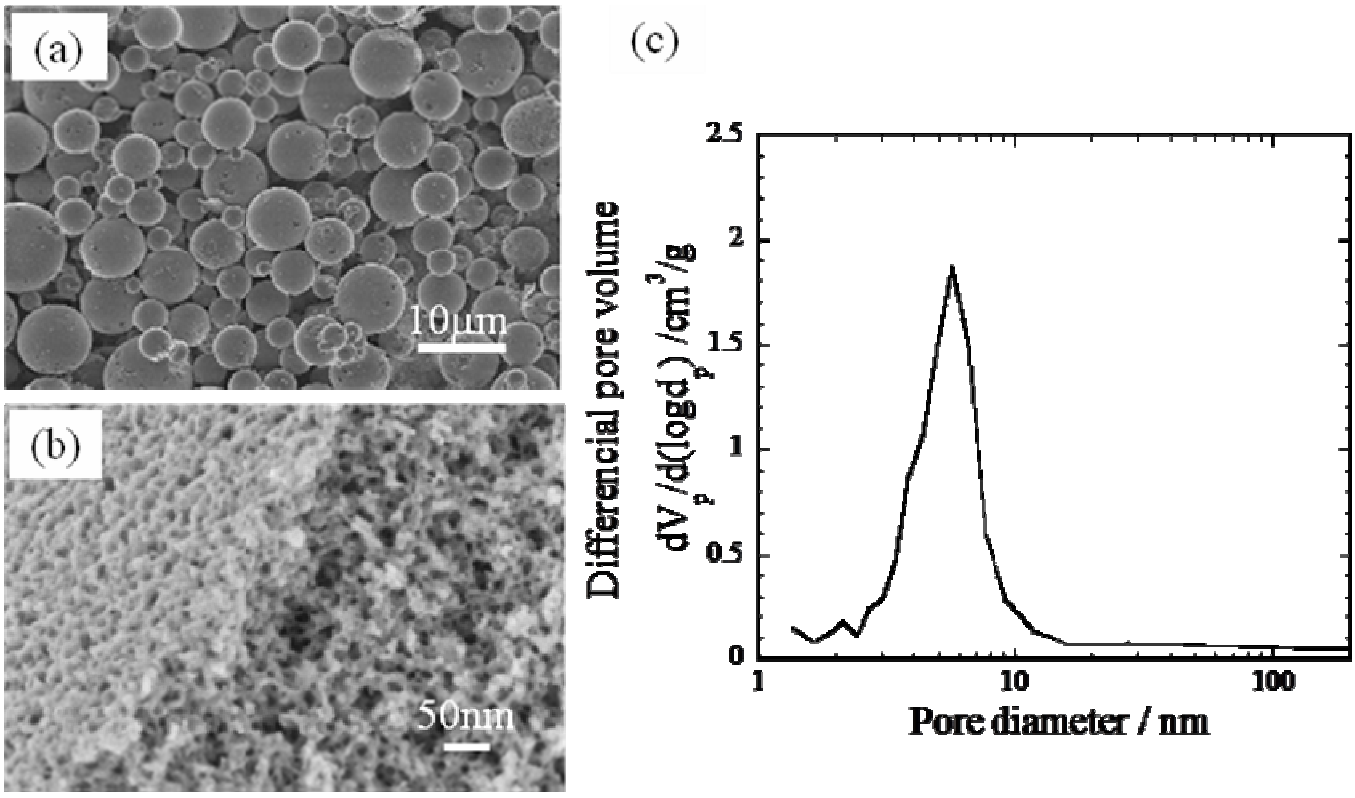

Figure 3: (a) Low magnification SEM images, (b) high magnification image and (c)pore size distribution of porous silica powder.

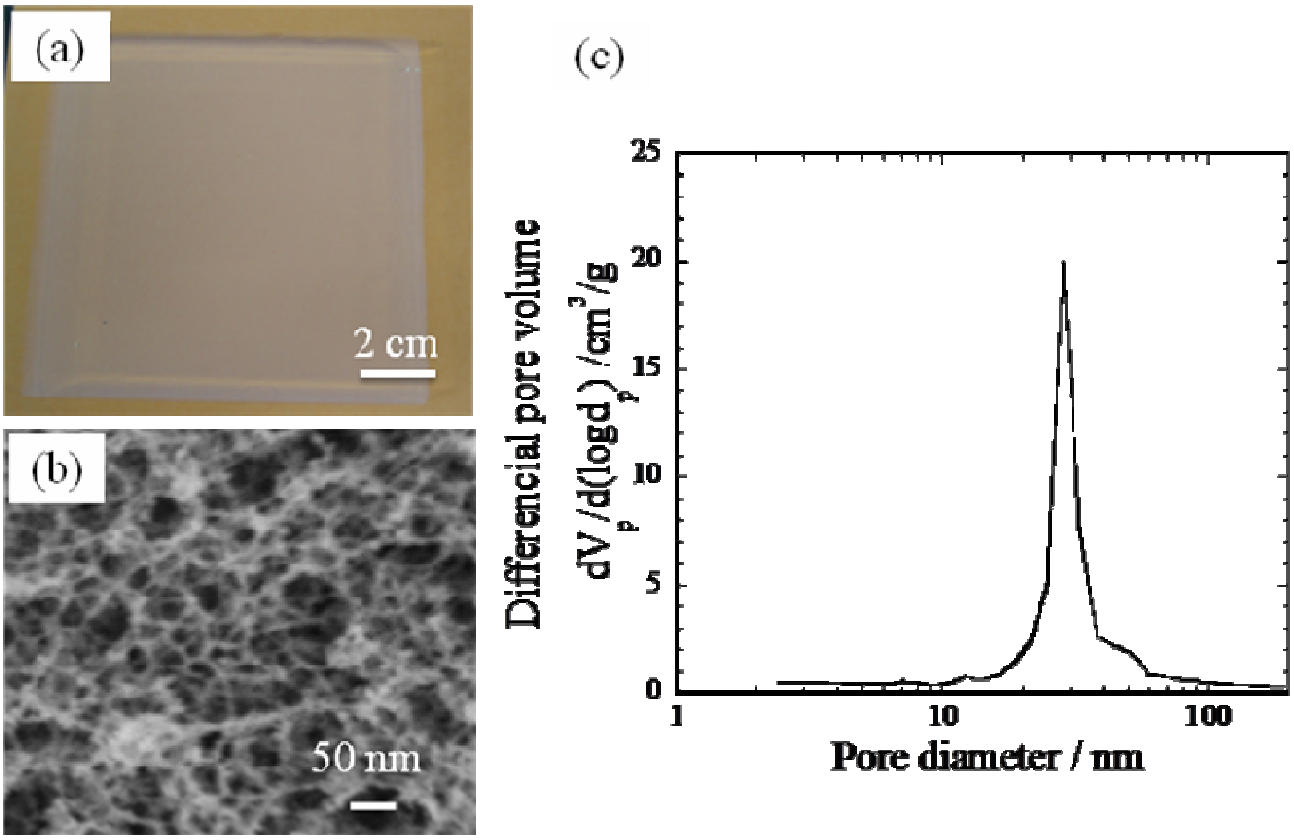

Figure 4: (a) Appearance of transparent silica aerogel. (b) High magnification SEM image of the silica aerogel. (c) pore size distribution of silica aerogel.

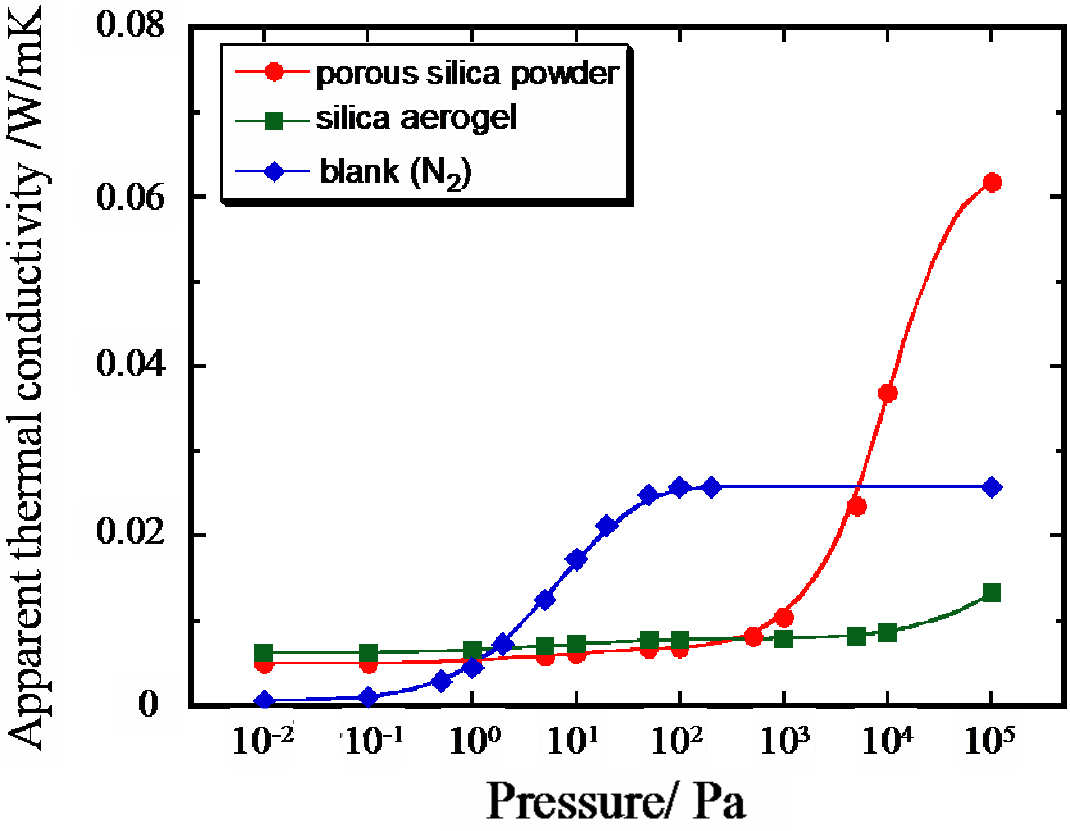

Figure 5: Pressure (vacuum) dependence of thermal conductivity for porous silica powder, silica aerogel and blank (N_2) gas.

CHAPTER 2

Synthesis and characterization of transparent silica aerogels

2.1 Transparent silica aerogels using silicon oligomer precursor

1. Introduction

Silica aerogels are unique materials which are characterized by high porosity and fine porous structure[1, 2]. Regardless of high porosity as high as >90%, silica aerogel shows optical transparency due to fine porous structure. In addition, very low solid fractions and small sizes of the pore bring the excellent thermal insulating properties. Low refractive index, low dielectric constant, and high specific surface area, correlated with high porosity of aerogel, are important properties as well. These remarkable properties of aerogels are expected to lead to many applications including thermal insulator for architectural purposes, insulator for integrated circuit and cladding materials for light guiding[3-5]. In spite of such promising applications, a fatal drawback has prevented aerogels from widespread applications except for particular field such as high energy-physics[6] and space science[7]. For example, aerogels are too brittle and fragile due to delicate and highly thin network structure consisting of weak linkage of silica nano particles. With the purpose of broadening the applications utilizing the above unique properties, numerous attempts to strengthen aerogels mechanically by aging[8, 9], crosslinking with organic polymers[10-12], preparing from or mixing organosilane precursors in a starting

solution[13-18] have been explored. However, such treatments sacrifice the transparency of aerogels.

For window application satisfying transparency and thermal insulation, multiple glazing simultaneously, which has the stacking structure of aerogel sandwiched between two plates of glasses with spacer, has been developed[19, 20]. When an external mechanical stress was applied for multiple glazing using aerogel as core materials, glass and spacer surrounded aerogel are primary strained before deformation of aerogel. Since Young's modulus of glass and spacer is higher than that of aerogel, the applied stress of aerogel inside the multiple glazing is relatively small and does not reach the compressive strength of aerogel. In short, as far as the application of multiple glazing is concerned, aerogel would rather desire the optical transparency than the mechanical strength; aerogel needs the softness enough to follow the stain of glass and spacer by compression and bending.

Tillotson *et al*. reported that aerogels from two-step sol-gel process of tetramethoxy silane (TMOS) showed excellent optical properties[21]. In two-step method, condensed precursor, which is hydrolyzed TMOS with lower stoichiometric amount of water under acidic condition, is polymerized with sufficient amount of water under basic condition. This two-step method is difficult to control the hydrolysis and condensation reaction in sol-gel step due to the cumbersome and complicated fabrication procedure. Quality-stable silicon oligomer with the similar structure of the precursor of two-step method is commercially available. In this study, aerogels using silicon oligomer as precursor have been prepared and their optical and mechanical properties are

investigated.

2. Experimental

2.1 Chemicals

Metylsilicate 51(MS) was purchased from Colcoat co., Ltd. Ethanol and 1 mol/L ammonia solution were from Nacalai tesque, inc. and Kanto chemical co. Ltd, respectively. 1, 1, 1, 3, 3, 3-Hexamethyldisilazane was obtained from Wako pure chemicals, Ltd. All reagents were used as received.

2.2 Synthetic procedure

A flow diagram of the experimental procedures is shown in Fig. 1. The molar ratios were Si: H_2O: ethanol = 1: (4-14): (4-8). The molar ratios were calculated by regarding MS as tetramer (Molecular weight is ca. 470). 0.1 M ammonia water was used as catalyst. The molar ratio of ammonia water was calculated by using the amount of water. All the gel were prepared by mixing together two solution, A&B, with ice cooling to retard the gelation. Solution A contained given amounts MS in ethanol; solution B contained an equal amount of ethanol and aqueous ammonia water (0.1M). The wet gel was aged at 50˚C for 2 days to complete the condensation. For methylation, the resultant wet gels were solvent-exchanged with 1, 1, 1, 3, 3, 3-hexametyldisilazane ethanol solution at room temperature and ethanol for 3 times each for more than 8 h. Resultant alcogels were dried from supercritical carbon dioxide at 50˚C, 12MPa in an autoclave (SCRD6, Reexam co., Ltd) to obtain aerogels. No shrinkage after supercritical drying was observed in the resultant gels derived from MS. For

the sample notation, the first number stands for the molar ratio of ethanol/MS and a number after the hyphen is related with the molar ratio of H_2O/MS. The last character “m” or “h” stands for metylated gel or hydrophilic gel, respectively.

2.3 Characterization

The porous morphology was observed under a field emission scanning electron microscope (FE-SEM) SU-8000 (Hitachi Ltd). Bulk density ρ_b was obtained by measuring the volume and weight of a gel. Nitrogen sorption measurements were performed to obtain total pore volume and pore size distribution with BELSOPR-miniII (BEL JAPAN, Inc.). Samples were outgassed under vacuum at 200°C for at least 1 h prior to measurement. Desorption branch was used for the BJH calculation. For light transmittance measurements from 380 nm to 780 nm, a UV-VIS-NIR spectrometer Lambda 950 (Perkin Elmer) equipped with an integrating sphere was employed. Direct-hemispherical transmittance was recorded, and obtained transmittance data at 550 nm were normalized into those of 10 mm-thick samples using the Lambert-Beer equation. Mechanical properties of aerogels were investigated by a material tester 5585 system (Instron co., Ltd). The measurement for carved aerogel (typically ca. 50×50×10 mm^3) were performed from the stress of 0 to 0.6 MPa by compression at a speed of 2 mm/min, and then back to 0 MPa by removing the load at the same speed. Young’s modulus is calculated as the slope between the strain ranges of 0.15 to 0.20.

3. Result and Discussion

3.1 Density and morphology of aerogels

Starting composition and obtained parameters of aerogels are listed in Table 1. All samples turn into a gel within an hour. Apparently, the decrease in density of aerogels with the concentration of water as well as ethanol is observed. This behavior is also confirmed to increase the total pore volume calculated from the nitrogen adsorption, which is attributed to relative decrease of silica component to the starting composition. Aerogels prepared by changing the amount of water and ethanol have almost same average pore diameter of approximately 30 nm.

Fig. 2 shows the resultant aerogel morphologies. Aerogels obtained from MS system possesses skeletons of aggregated globules and small pores (~ 10 to 30 nm, mesopores). From Fig.2 (a)-(c), it was also observed that the pore morphology becomes slightly homogeneous with decreasing the concentration of ethanol. Fig.2 (d)-(f) suggests that domain size (pore size plus skeleton size) is smaller with increasing the concentration of H_2O. The result of pore size distribution (Fig.3) indicates that pore size is sharper with increasing the water concentration, which coincides with the SEM observation (Fig.1 (d)-(f)).

3.2 Optical properties

Fig.4 exhibits the visible light transmittance of 1 cm thick aerogels prepared by different molar ratio of H_2O/Si. The increase in transmittance with higher water content of starting composition is observed. The transmittance at 550 nm for 08-08m, 08-05m and 08-04m is 92%, 86%, 83%, respectively. One can see that the transmittance of gels decrease gently in the short wavelength region.

Since there is no absorption band in the wavelength range of visible light for SiO_2, a decrease in transmittance of shorter wavelength is presumed to be caused by the light scattering. As the refractive index of silica aerogel is close to 1, it can be considered that surface reflection is negligible and the scattering is almost isotropic. This light scattering is well described by the Rayleigh theory[22, 23];

$$\alpha = \frac{2\pi^5 d^6}{3\lambda^4}\left(\frac{n^2-1}{n^2+1}\right)^2 \quad (1),$$

where α is absorption coefficient, *d* is the scattering center dimension (diameter of particle or fiber), *n* is the refractive index of the silica and λ is wavelength of light. Absorption coefficient, α, is calculated as follows; $T = \exp(-\alpha L)$, where L is the thickness of sample. According to these equation, absorption coefficient, α, should be related to wavelength with the power factor of -4. For aerogels prepared in this study, absorption is plotted against the wavelength (Fig.6 (b)), showing good linearity.

The scattering of light in aerogels is caused by distribution of refractive index such as fine particle composed of silica skeleton and fine pore surrounded by silica skeleton. As mentioned above, the morphology becomes finer and pore size distribution becomes sharper with higher water content of starting composition is observed. This finer structure, thinner skeleton and smaller pore size, suppresses the light scattering and brings higher transmittance.

Fig.5 shows the effect of Ethanol/Si molar ratio on transmittance. When ethanol concentration is modulated, aerogel with the density of 0.13 $g \cdot cm^{-3}$ is the most transparent and its transmittance is 90%. From SEM images (Fig.2

(a)-(c)), it is observed that structure becomes more inhomogeneous with increasing the concentration of ethanol. From the ^{29}Si NMR studies, it is revealed that an increase in solvent content reduces the rate of polymerization reactions leading to more separation between the SiO_2 clusters[24]. Therefore, the aerogels formed by using excess ethanol happened to have larger pore sizes with low densities as shown in Fig.2 (a)-(c). This pore sizes affect the transmittance of aerogels.

3.3 Compressive mechanical properties

Fig.8 shows stress-strain curve for 10-08m obtained by cyclic uniaxial compression test. For comparison, data for the aerogel without methylation, 10-08h, is also shown. Stress becomes exponentially larger with increasing strain for both samples due to the densification of the aerogels. Young's modulus, *E*, of 10-08m and 10-06h is 0.46 and 0.42 MPa, respectively. This relationship reflect the slightly higher density of 10-06h (0.12 $g \cdot cm^{-3}$) than that of 10-06m (0.11 $g \cdot cm^{-3}$). The recovery ratio of metylated sample is as high as 32 % of original shape, which is higher than that of aerogels without methylation treatment, only 15 %. Similar phenomenon is reported by aerogels from methyltrimethoxysilane (MTMS) precursor, exhibiting recovery of 30% from original shape[17] and, for aerogels optimized starting composition and post treatments, showing almost 100 %[15]. The surface of silica skeletons of metylated aerogels as well as aerogels from MTMS are covered with methyl group. In the case of aerogels from MTMS, the recovery is caused by repulsive interaction between methyl groups and low concentration silanol group. A

similar situation is expected for present metylated aerogels. In contrast, hydrophilic aerogel shrunk and barely recovered, because the silanol groups that are close together react to siloxane bonds during the compression test.

The effect of mechanical properties on the ratio of ethanol and water to silicon oligomers is examined. The Stress-strain curves for aerogels from different ethanol/Si ratio by cyclic uniaxial compression test are shown in Fig.8 (a). The aerogels becomes softer (more strain fixed stress) in the order of 12-06m < 10-06m < 08-06m. Young's modulus of 12-06m, 10-06m and 08-06m is 0.24, 0.42 and 0.66 MPa, which is related to the bulk density with the power of 4. Similar scaling law (scaling exponent of 2.5 to 4) is reported by 3-point bending and ultrasound velocity measurement[25-27]. Fig.8 (b) illustrates stress-strain curves for aerogels from different H_2O/Si ratio by cyclic uniaxial compression test. No significant change in Young's modulus and recovery ratio is observed. Young's modulus of 08-04m, 08-05m and 08-08m is 0.63, 0.66 and 0.66 MPa, respectively. As mentioned above, Young's modulus is changed with density. From the decrease in density from 0.14 to 0.12 $g \cdot cm^{-3}$ with increasing the H_2O/Si ratio from 4 to 8, decrease in Young's modulus was anticipated but the Young's modulus measured by uniaxial compression test was not changed. In short, taking into account of the decrease in density, it is found that aerogels become harder with increasing the water content. From SEM images and pore size distribution, it is confirmed that the structure becomes finer and pore distribution is smaller with increasing the water concentration. This finer structure makes it possible to disperse the mechanical stress, leading to smaller strain and hardness of aerogels from higher H_2O/MS ratio.

4. Conclusion

Transparent aerogels using silicon oligomer as precursor have been prepared and the effect of the concentration of water and ethanol on optical, mechanical thermal properties of resultant aerogel was investigated. Total pore volume and density measurement confirmed that the density of aerogel decreased with increasing the concentration of ethanol and water. FE-SEM observation indicated that aerogels from silicon oligomer possessed skeletons of aggregated globules and small pores. With decreasing the concentration of ethanol at starting condition, the microstructure of aerogels became slightly homogeneous, which affected optical transmittance and uniaxial compression behavior. With increasing H_2O/Si ratio, the domain size of aerogel became finer, leading to higher optical transparency as high as 92 % at 550 nm for 1cm thick aerogel and stiffer character against the uniaxial compression.

Reference

[1] J. Fricke and A. Emmerling, *Journal of the American Ceramic Society* **75** (1992), p. 2027.

[2] A. C. Pierre and G. M. Pajonk, Chemistry of aerogels and their applications, ACS Publications (2002).

[3] H.-S. Yang, S.-Y. Choi, S.-H. Hyun, H.-H. Park and J.-K. Hong, *Journal of Non-Crystalline Solids* **221** (1997), p. 151.

[4] J.-K. Hong, H.-S. Yang, M.-H. Jo, H.-H. Park and S.-Y. Choi, *Thin Solid Films* **308-309** (1997), p. 495.

[5] L. W. Hrubesh, *Journal of Non-Crystalline Solids* **225** (1998), p. 335.

[6] T. Sumiyoshi, I. Adachi, R. Enomoto, T. Iijima, R. Suda, M. Yokoyama and H. Yokogawa, *Journal of Non-Crystalline Solids* **225** (1998), p. 369.

[7] P. Tsou, *Journal of Non-Crystalline Solids* **186** (1995), p. 415.

[8] A. Fidalgo, M. E. Rosa and L. M. Ilharco, *Chemistry of Materials* **15** (2003), p. 2186.

[9] S. H□eid, J. Anderson, M. A. Einarsrud, D. W. Hua and D. M. Smith, *Journal of Non-Crystalline Solids* **185** (1995), p. 221.

[10] B. M. Novak, D. Auerbach and C. Verrier, *Chemistry of Materials* **6** (1994), p. 282.

[11] M. A. B. Meador, E. F. Fabrizio, F. Ilhan, A. Dass, G. Zhang, P. Vassilaras, J. C. Johnston and N. Leventis, *Chemistry of Materials* **17** (2005), p. 1085.

[12] N. Leventis, C. Sotiriou-Leventis, G. Zhang and A.-M. M. Rawashdeh,

Nano Letters **2** (2002), p. 957.

[13] N. Hüsing, U. Schubert, R. Mezei, P. Fratzl, B. Riegel, W. Kiefer, D. Kohler and W. Mader, *Chemistry of Materials* **11** (1999), p. 451.

[14] N. Hüsing and U. Schubert, *Journal of Sol-Gel Science and Technology* **8** (1997), p. 807.

[15] K. Kanamori, M. Aizawa, K. Nakanishi and T. Hanada, *Advanced Materials* **19** (2007), p. 1589.

[16] K. Kanamori, M. Aizawa, K. Nakanishi and T. Hanada, *Journal of Sol-Gel Science and Technology* **48** (2008), p. 172.

[17] K. Kanamori, K. Nakanishi and T. Hanada, *Journal of the Ceramic Society of Japan* **117** (2009), p. 1333.

[18] M. Nogami, S. Hotta, K. Kugimiya and H. Matsubara, *Journal of Sol-Gel Science and Technology* **56**, p. 107.

[19] K. I. Jensen, J. M. Schultz and F. H. Kristiansen, *Journal of Non-Crystalline Solids* **350** (2004), p. 351.

[20] J. M. Schultz and K. I. Jensen, *Vacuum* **82** (2008), p. 723.

[21] T. M. Tillotson and L. W. Hrubesh, *Journal of Non-Crystalline Solids* **145** (1992), p. 44.

[22] M. Kerker, The scattering of Light, Academic Press, New York (1969).

[23] C. G. Bohren and D. R. Hoffman, Absorption and Scattering of Light by Small Particles, Wiley, New York (1983).

[24] B. E. Yoldas, *Journal of Non-Crystalline Solids* **83** (1986), p. 375.

[25] T. Woignier, J. Pelous, J. Phalippou, R. Vacher and E. Courtens, *Journal of Non-Crystalline Solids* **95-96** (1987), p. 1197.

[26] J. Gross and J. Fricke, *Journal of Non-Crystalline Solids* **145** (1992), p. 217.

[27] A. H. Alaoui, T. Woignier, G. W. Scherer and J. Phalippou, *Journal of Non-Crystalline Solids* **354** (2008), p. 4556..

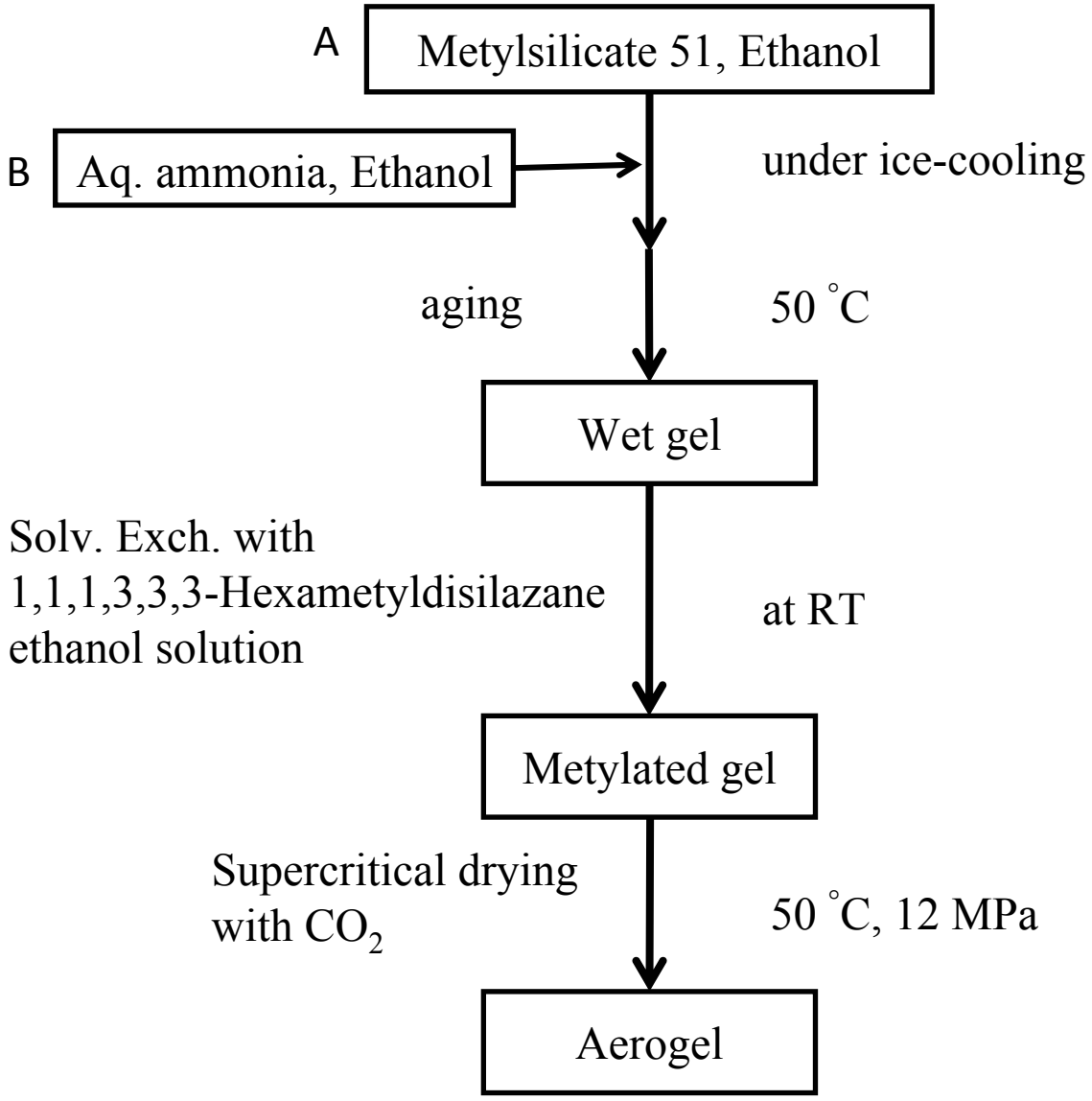

Figure1: Flow diagram of experimental procedure

Table1: Starting composition and obtained properties of aerogels

	Ethanol/Si	H_2O/Si	ρ_b/g·cm^{-3}	V_p /cm^3 g^{-1}	d/ nm
04-06m	4	6	0.20	-	-
05-06m	5	6	0.17	-	-
06-06m	6	6	0.16	-	-
07-06m	7	6	0.14	-	-
08-06m	8	6	0.13	3.24	25
10-06m	10	6	0.11	3.26	28
12-06m	12	6	0.10	3.46	28
14-06m	14	6	0.09	-	-
08-04m	8	4	0.14	3.02	28
08-05m	8	5	0.13	3.39	28
08-07m	8	7	0.12	3.51	33
08-08m	8	8	0.12	3.46	33

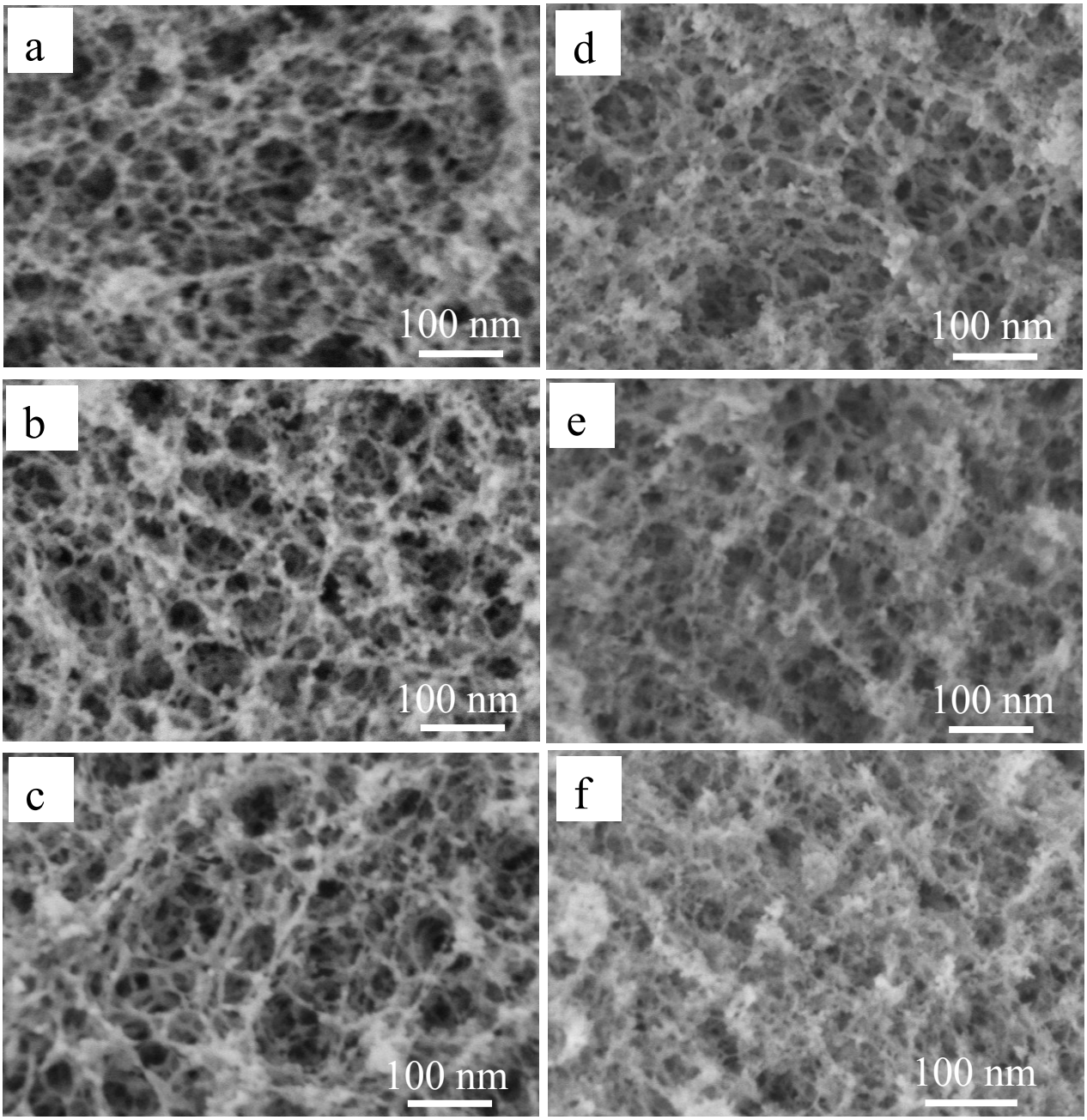

Figure 2: FE-SEM images of obtained aerogels; (a)08-06m, (b)10-06m, (c)12-06m, (d)08-04m, (e)08-05m , (f)08-08m.

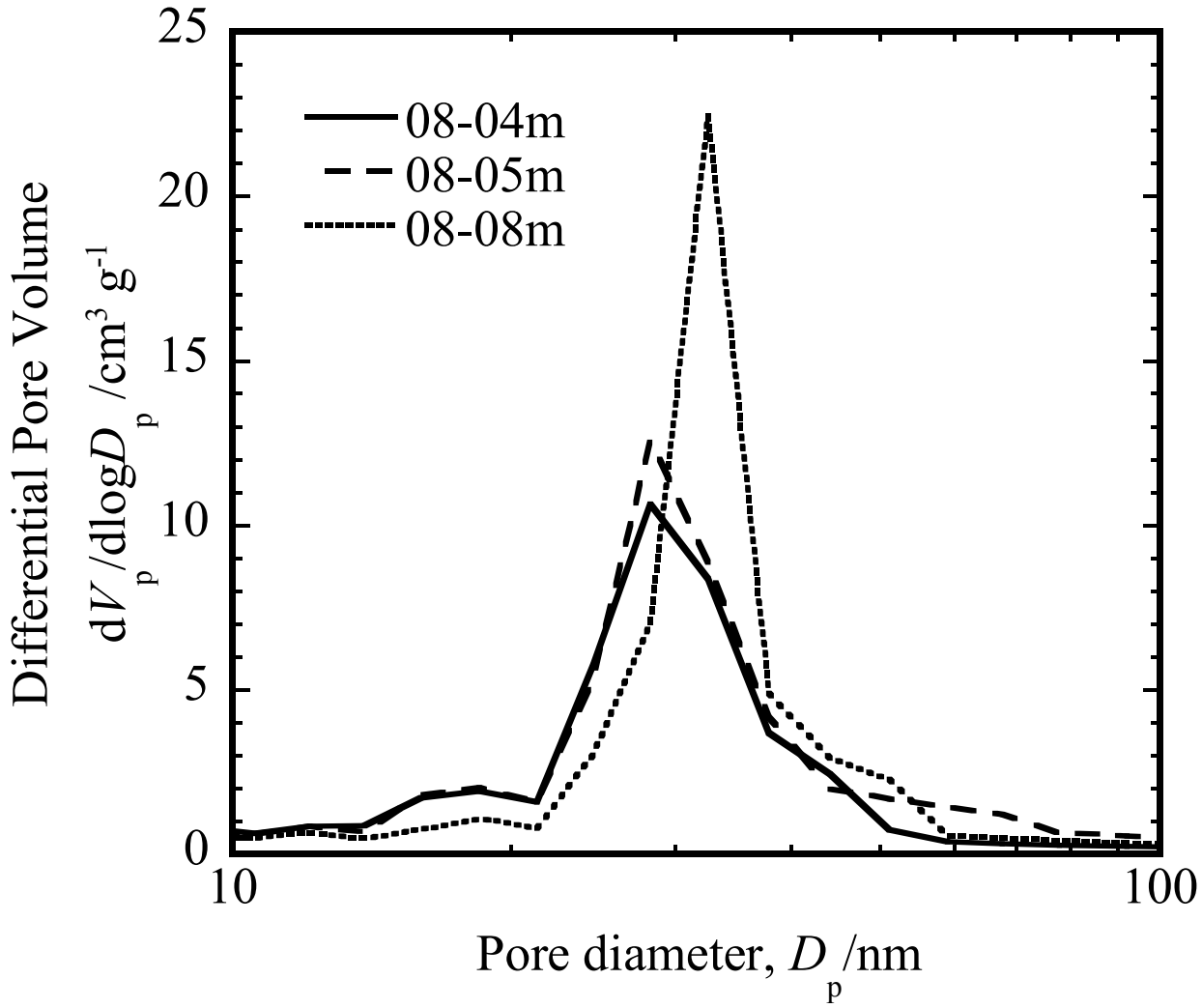

Figure 3: Pore size distribution obtained from the BJH method using desorption branch: Solid, broken and dotted line correspond to 08-04m, 08-05m and 08-08m, respectively.

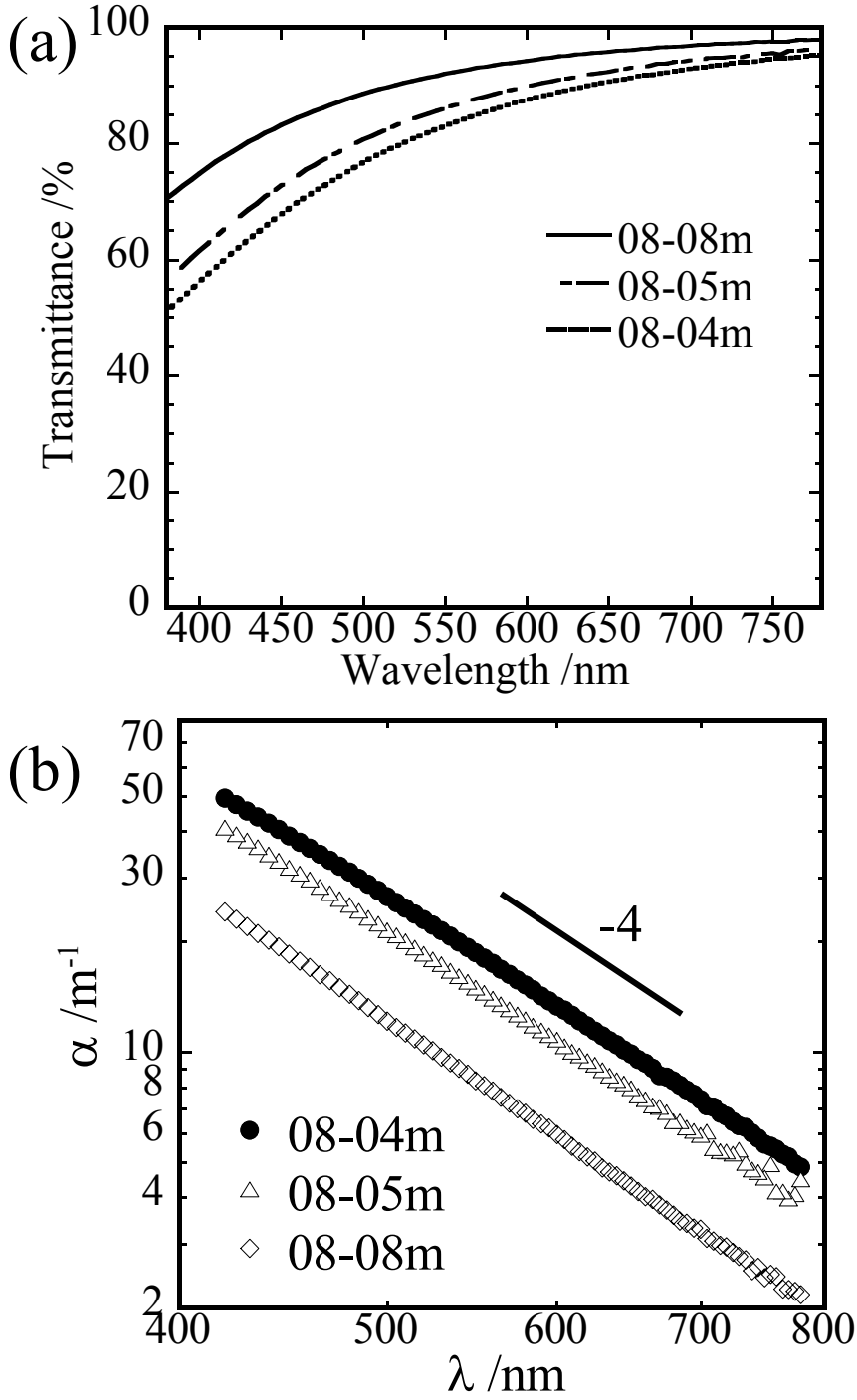

Figure 4: (a) Optical transmittance spectra for the aerogel prepared from different molar ratio of water to MS. Thickness of samples is 10 mm. Solid, broken and dotted line correspond to 08-04m, 08-05m and 08-08m, respectively. (b) Relation between absorption coefficient, a, and wavelength plotted as log-log plot. Absorption scaled as the -4 power of the wavelength.

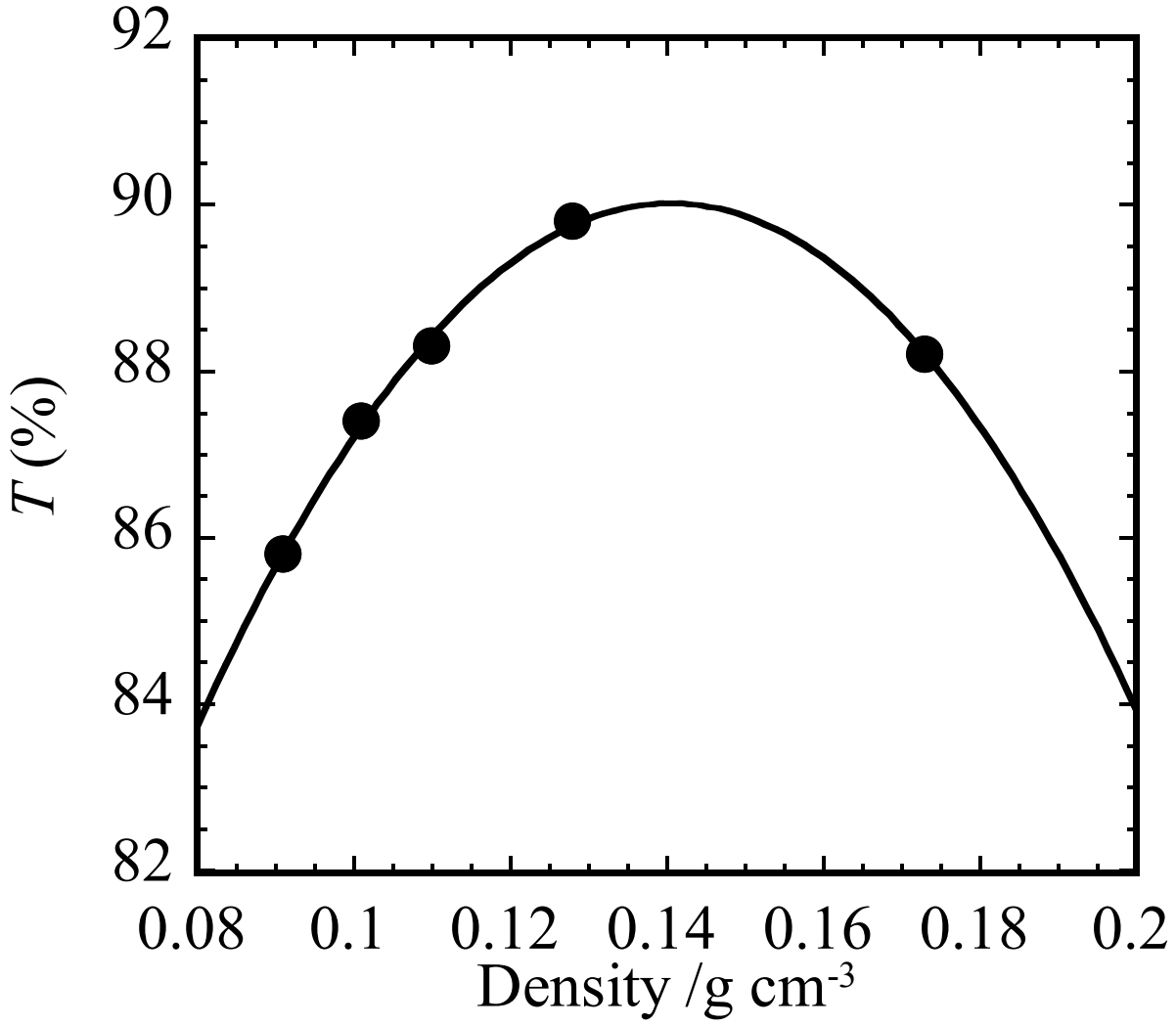

Figure 5: Relation between the transmittance (%) at 550 nm wavelength and density for aerogels prepared from the different ethanol/Si ratio.

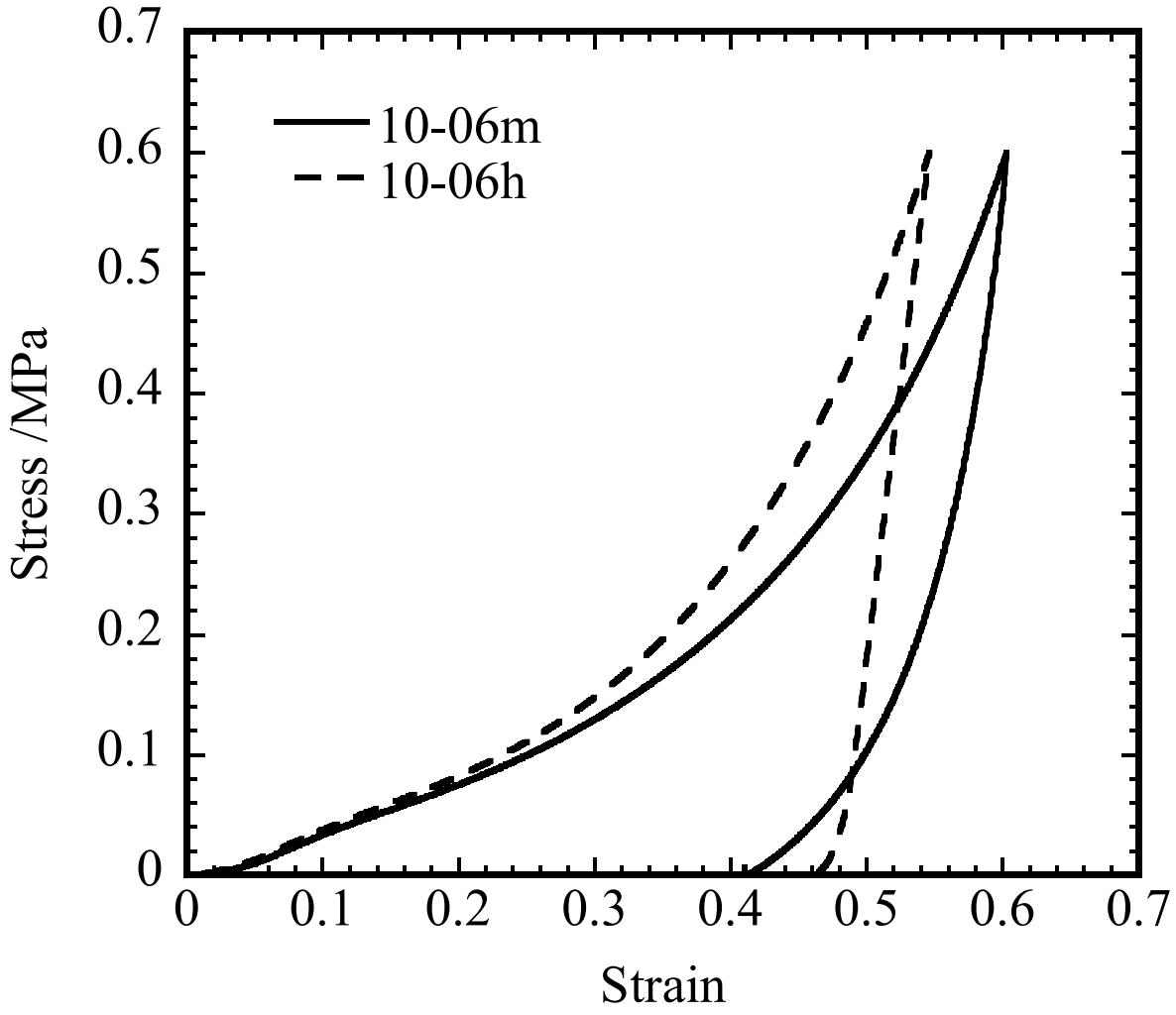

Figure 6: Stress-Strain curves of obtained aerogel: solid and dashed line corresponds to 10-06m and 10-06h, respectively.

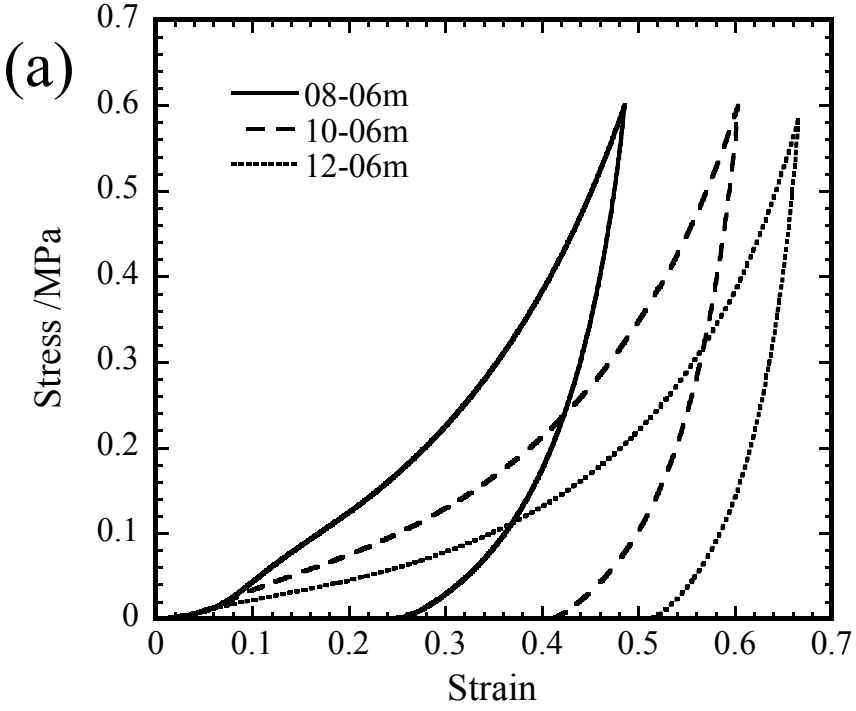

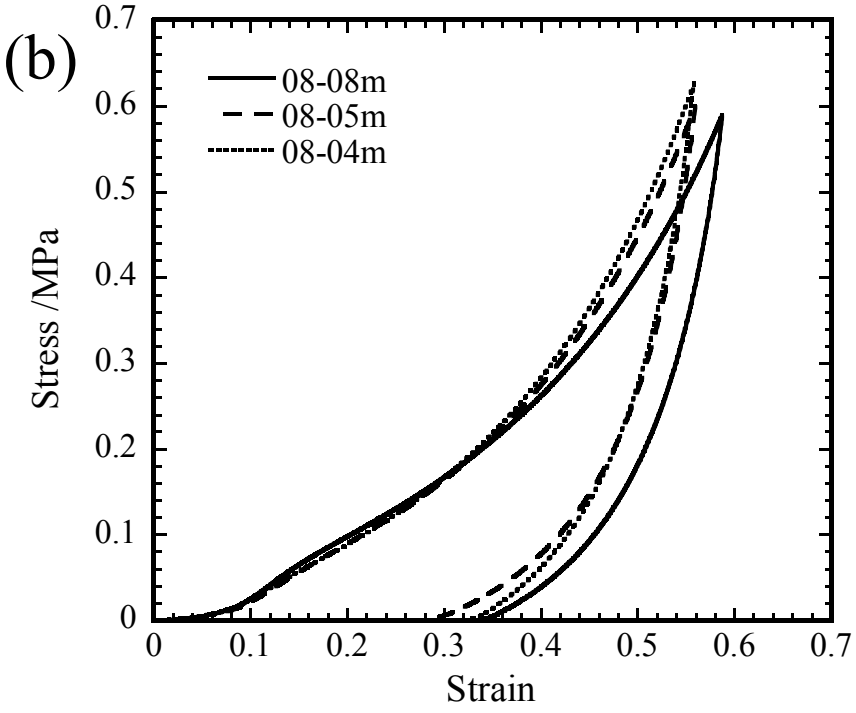

Figure 7: (a) Stress-stain curves for aerogels with different ethanol ratio to MS. (b) Stress- strain curves for aerogels with different H_2O/Si ratio.

2.2 Transparent silica-based aerogels using Methyltrimethoxysilane precursor

1. Introduction

Commercial silica aerogels which are produced by drying sol-gel-derived hydrogels under super critical condition of liquids such as water, alcohol, and carbon dioxide are characterized to contain small pores (ca. 50 nm), large surface area (> ~500 m^2/g), and high porosity (> 80 %)[1]. These key properties of aerogels lead to many applications including thermal insulation for architectural purposes, heat storage appliances, transport vehicles and space industry[2-5]. In addition to their low thermal conductivities, they possess outstanding characteristics in their optical transparency in the visible wavelength region and have high potential applications to use in an architectural windows exhibiting extremely low thermal conductivity[6, 7]. Despite of these potential applications, there are some drawbacks. For example, aerogels are brittle and fragile due to their thin skeletons composing of the porous morphology, resulting into more difficult to practical usage of aerogels in large scale. Another problem is the hydrophilic property of the aerogels during long time usage[8]. To overcome these disadvantages of aerogels, many studies of organically modified silica aerogels. Terminating the skeleton surface with organics such as methylsilane groups brings the gel hydrophobic property. On the wrong way, however, the transparency of the obtained aerogels falls to lower.

Our interest focuses on the preparation of high transparent silica-based

aerogels with high mechanical strength and Young's modulus. In this work, non-ionic surfactant molecules are used to control the skeleton structure and pore size. Methyltrimethoxysilane was hydrolyzed using acid and base catalysts, followed by reacting with the surfactant for adjusting the skeleton structure of hydrogels. It was found that non-ionic surfactant molecules are appropriate to form fibrous skeleton structure with small-sized pores, which are easily removed by soaking in hot water, resulting in the formation of porous aerogels with high transparency. Rayleigh scattering was also discussed in relation with the pore and skeleton size of aerogels.

2. Experimental

2.1 Sample preparation

The silica-based aerogels were prepared by hydrolyzing methyltrimethoxysilane ($CH_3Si(OCH_3)_3$, MTMS, Aldrich) with formic acid (HCOOH) and NH_4OH as hydrolysis catalysts. Non-ionic surfactant used in this study was ethylene oxide/propylene oxide block copolymer ($(C_2H_4O)_{118}(C_3H_6O)_{45}(C_2H_4O)_{118}$, F98, BASF). All materials were used as received. Water purified with a Milli-Q system from Millipore (AQUARIUS/GS-20R) was used for the experiments. The synthetic process is showed in Fig. 1. Initially, the calculated amount of MTMS was added into the mixture of water (as 0.01 mol/l HCOOH aq. as catalyst) and F98, followed by stirring for 10 h to hydrolyze MTMS. After adding 1 mol/l NH_4OH solution, the mixture was stirred for 20 min, followed by aging at room temperature for 24 h in

a closed vessel, resulting into the formation of wet gel. For optimizing the F98 content, samples were prepared to contain F98 up to 15 wt% in the 1MTMS·14H_2O (molar ratio) sample. The obtained wet gels were soaked in ethanol at ambient temperature for 12 h. The other wet gels were soaked in hot water at 50 ˚C for 3 days, followed by soaking in ethanol to exchange the water. The obtained gels were placed in the autoclave (Ryusho Co.Ltd. SCRD6, Japan) chamber together with ethanol, then dried by supercritical carbon dioxide at 50 ˚C under 12 MPa. Thus, the aerogels obtained with and without using hot water were abbreviated such as H14F5-T and H14F5-N, respectively.

The aerogel prepared using tetramethoxysilane ($Si(OCH_3)_4$, TMOS) was compared with the MTMS-derived aerogels. The hydrolysis and supercritical drying conditions were same as that for MTMS.

2.2 Characterization

The surface morphology of the prepared aerogels was characterized by scanning electron microscopy (JEOL-JSM-6301, NORAN instrument). The surface area, pore volume and pore-size distribution of the samples were measured using a nitrogen-gas sorption analyzer (NOVA-1000, Quantachrome Corporation). Prior to the measurements, the samples were preheated at 250 ˚C in vacuum in order to remove the remaining absorbed water. The pore size distribution was determined by the Barret-Joyner-Halenda (BJH) method. The average pore size (d) was calculated from the pore volume (V) and surface area (S) assuming the existence of cylindrical pores: $d = 4\ V/S$.

Flexural elastic modulus of the sample was determined from the stress-strain

curves using three-point bending method.

Small angle X-ray scattering (SAXS) data were collected using a Rigaku-SAXS system, Nanoviewer, using Cu-Kα radiation at wavelength of 0.154 nm.

3. Results and discussion

3.1 Effect of F98 surfactant on the transparency of aerogels

Silica-based aerogels, prepared from $Si(OCH_3)_4$ (TMOS) and $Si(OC_2H_5)_4$ (TEOS) as starting materials, are not generally suitable for practical uses because of their low mechanical strength and fragility, even though their high transparency. Another problem of these aerogels is the hydrophilicity. The pore surfaces are terminated with hydroxyl bonds bound with silicon atoms to absorb the water in ambient atmosphere, resulting into become more fragile and turbid. The modification of these silica gel skeletons with organic compounds would be expected to improve the hydrophobity of the pore surfaces. Methyltrimethoxysilane and dimethylmethoxysilane, having one and two methyl groups, respectively, attached to one silicon atom, are candidates to improve their mechanical and hydrophobic properties. When these compounds are hydrolyzed, alkoxy groups, SiOR, are hydrolyzed to form hydroxyl groups, SiOH, followed by polymerizing to form three dimensional siloxane network structures. The surfaces of the network structure are stopped with the methyl groups not to be further hydrolyzed, which brings the gel hydrophobic property. This molecular conformation causes serious phase separation during its hydrolysis-polymerization process, resulting into the formation of gels having

large pores with wide distribution. This pore structure often causes the transparency of aerogels down. The gel prepared without using F98 exhibited no transparency, but white color and fragile to powders.

F98 surfactant is used in this study to control the pore morphology of the wet gels. Different amounts of F98 were added to the hydrolyzed MTMS solution to form the wet gels, the pictures of which are shown in Fig. 2a. It is apparent that the transparency of the obtained wet gels increases as the content of F98 increases. F98 surfactant is non-ionic, in which both the hydrophobic and hydrophilic units are connected. During polymerization reaction of the hydrolyzed MTMS into three dimensional network structures, the CH_3 bonds terminating the network structure are bound with the hydrophobic units of F98 molecules. The other hydrophilic units have an affinity with water molecules in the solvent. Therefore, with increasing F98 content, the growth of siloxane network is limited, resulting into the formation of small pores and then the increased transparency. These monolithic wet gels were soaked in ethanol to replace the solvent, followed by drying under supercritical conditions. Figure 2b exhibits the picture of the obtained aerogels. It is apparent that the transparency of aerogels decreases after supercritical drying. Moreover, the transparency of the aerogels decreases by increasing the F98 content more than 10 wt%. On the other hand, when the wet gels were soaked in hot water at 50 ˚C before solvent replacement by ethanol, the obtained aerogels exhibit high transparency, which increases with increasing the F98 content as shown in Fig. 2c. Thus, the treatment of the wet gels in hot water is appropriate for the preparation of transparent aerogels.

It was noticed that when the wet gels containing F98 were soaked in ethanol, they were swollen in solvent. Thereafter, the swollen gels were observed to shrink during supercritical drying. These swelling and shrinkage behaviors cause stress to form cracks in the gel, resulting into the transparency decrement. The rate of shrinkage and swelling of gels during soaking in ethanol and thereafter supercritical drying, respectively, are shown in Fig. 3. Apparently, the transparency of the aerogels is well related with their swelling rate in the ethanol solvent. Some different alcohols and water were tested to avoid the swelling of gels in their solvents. Among the tested solvents, hot water at 50 °C was found to be the best for suppressing the swelling of the wet gel. In Fig. 3, the swelling of gels soaked in hot water at 50 °C and the shrinkage by thereafter supercritical drying are also presented. It is evident that the swelling and shrinkage rates are significantly decreased. As the solubility of F98 in water decreases with increasing temperature, the F98 molecules are effectively extruded from the gel.

3.2 Porous properties of aerogels

Fig. 4 shows the optical transmittance spectra and pore size distribution curves of the aerogels (H14Fx-T series) prepared by replacement with hot water, followed by supercritical drying. It is evident that smaller pores are formed together with narrow distribution of size with the F98 content increment. Corresponding to the decreased pore size, the transparency clearly increases. With this relation between the pore size and transparency, one can conclude that in the series of molar ratio of 14:1 for H_2O and MTMS, the minimum size of pore is about 20 nm, where the transparency is limited to be about 50 % at 400 nm

wavelength for the thickness of 3 mm.

For preparation of aerogels with higher transparency, MTMS was hydrolyzed by changing the ratio of H_2O and F98 to MTMS. Typical examples of the transmittance spectra and pore size distribution curves are shown in Fig. 5. It was found that in our experiments the pore becomes smaller together with narrowing the pore size distribution as the ratio of F98 to water content increases. By optimizing the hydrolysis condition of MTMS, we could prepare the aerogel with an average pore size of 10 nm and its narrow size distribution. The transparency increased with decreasing pore size and reached to 65% at 400 nm wavelength for the thickness of 10 mm.

The prepared aerogels also exhibit excellent mechanical properties. In Fig. 6, the bending strength and Young's modulus are compared with the aerogel prepared using TMOS. It is evident that aerogels prepared in this study exhibit good mechanical strength and Young's modulus three times higher than those of TMOS-derived aerogel.

The structural and physical properties of aerogels prepared in this study are summarized Table 1. It is generally known that the porosity was controlled almost constant about 85%. Therefore, the transparency and mechanical properties can be discussed in relation with the skeleton structure, pore size and size distribution.

3.3 Pore structure formed in aerogels

In this section, the effect of the gel structure on the transparency is further studied. Fig. 7 exhibits the SEM images of the prepared aerogels. Apparently,

the gel morphology is strongly affected by the preparation conditions. The H15F5-T aerogel is composed of the chain structure connecting the sphere-like particles of the few tens nano-meter size. On the other hand, with increasing F98 content, the structure changed from spheres-connected structure to fibrous ones together with decreasing their size. The H9F28-T aerogel consists of three dimensionally connected fibers of ~ 10 nm diameter. These differences in the gel structure can be more clearly studied by small angle X-ray scattering (SAXS) experiments. Fig. 8 demonstrates SAXS profiles of the prepared aerogels. It is evident that the scattering intensities drastically decrease with increasing F98 content. The decreased X-ray scattering intensity would result into the increased optical transmittance. The significant differences were noticed in the SAXS patterns. The H15F5-T aerogel exhibits the pattern characterized by the aggregated particles with a wide size distribution. On the other hand, aerogels prepared using large amount of F98 exhibit the peak in SAXS patterns, and the peak position shifts to larger *q*-value as the F98 content increase. The appearance of peak in the SAXS patterns indicates the existence of the strongly correlated scattering species. From the peak position, the size of correlated scattering species, *L*, can be calculated by simulating Brag's law: $L = 2\pi/q$, where $q = 4\pi\lambda^{-1}\sin\theta$, and θ and λ are scattering angle and wavelength of used X-ray, respectively. The *L* values are calculated as 47, 47, 19, and 17 nm for H14F8-T, H14F14-T, H10F23-T, and H9F28-T aerogels respectively. Compared with SEM images shown in Fig. 7, these *L* values can be recognized as the size of particles and fibers composed of aerogels.

The formation of these different gel morphologies was further investigated by

measuring the time-developed SAXS intensities. For the SAXS experiments, the MTMS was hydrolyzed with water and HCOOH, followed by adding NH_4OH in the glass capillary. After F98 surfactant was added under vigorously stirring, the capillary was set in the SAXS equipment, and the SAXS profiles were measured as a function of time, which are shown in Fig. 9 as log-log plot. It was proved that the H14F5-T sample exhibits the typical profile showing the aggregated particles and their particle growth with time. The slope in large *q*-value range is calculated to be -4 using the Porod's law, indicating the sharp surface of the particles. As the time increases, the intensities also increase and the position deviating from the Porod's law shifts to low *q*-value, indicating the growth of the particles. As for the H9F28 sample shown in Fig. 9b, on the other hand, the slope at the initial stage and approaches to -4 as the time increases. Simultaneously, the intensities in the middle range of q-value increase exhibiting the peak, though the scattering intensity in the low *q*-value is not changed. It is also apparent that the intensities at the peak position increase together with shifting to low *q*-value, indicating the increase in the fiber diameter.

3.4 Light scattering for aerogels

It was found that the prepared aerogels consist of three dimensionally-connected structure of fibers and colloidal particles with few tens nm size, where the pore size is also in the same orders. As the silica does not absorb visible light, the decrease in the transparency is attributed to the light scattered by particles in a transparent medium like air or the pores in the transparent silica. This light scattering is well described by the Rayleigh

theory[9, 10];

$$\alpha = \frac{2\pi^5 d^6}{3\lambda^4}\left(\frac{n^2-1}{n^2+1}\right)^2 \quad (1),$$

where α is absorption coefficient, *d* is the scattering center dimension (diameter of particle or fiber), *n* is the refractive index of the silica and λ is wavelength of light. The transmittance, T, is then represented as $T = \exp(-\alpha L)$, where *L* is the thickness of sample. According to these relations, the transmittance should be related to the size of scattering centers with the power factor of 6. For samples prepared in this study, transmittance at wavelength of 400 nm is plotted against the silica gel fiber or particles and pore size (Fig. 10), showing good linearity.

4. Conclusion

Transparent silica-based aerogels using methyltrimethoxysilane and non-ionic surfactant by supercritical drying process have been prepared. Non-ionic surfactant was successfully used for forming wet-gels composing of the three dimensional-connected thinner fibers of silica skeletons with ~ 10 nm in diameter. It was found that the surfactants were effectively removed from the wet-gels by soaking in hot water without changing the gel size, resulting in the preparation of high transparent aerogels after supercritical drying. The transparency of aerogels increased up to 65% at 400 nm wavelength for 10 mm thickness of sample composing of the fiber skeletons or pores with ~ 15 nm of diameter. The formation process of wet- and aero-gels using the small angle X-ray scattering experiments was also elucidated.

Reference

[1] J. Fricke and A. Emmerling, *Journal of the American Ceramic Society* **75** (1992), p. 2027.

[2] V. Wittwer, *Journal of Non-Crystalline Solids* **145** (1992), p. 233.

[3] L. W. Hrubesh, *Journal of Non-Crystalline Solids* **225** (1998), p. 335.

[4] M. Schmidt and F. Schwertfeger, *Journal of Non-Crystalline Solids* **225** (1998), p. 364.

[5] G. M. Pajonk, *Journal of Non-Crystalline Solids* **225** (1998), p. 307.

[6] N. Hüsing and U. Schubert, *Journal of Sol-Gel Science and Technology* **8** (1997), p. 807.

[7] D. Haranath, G. M. Pajonk, P. B. Wagh and A. V. Rao, *Materials Chemistry and Physics* **49** (1997), p. 129.

[8] A. Venkateswara Rao, M. M. Kulkarni, D. P. Amalnerkar and T. Seth, *Journal of Non-Crystalline Solids* **330** (2003), p. 187.

[9] M. Kerker, The scattering of Light, Academic Press, New York (1969).

[10] C. G. Bohren and D. R. Hoffman, Absorption and Scattering of Light by Small Particles, Wiley, New York (1983).

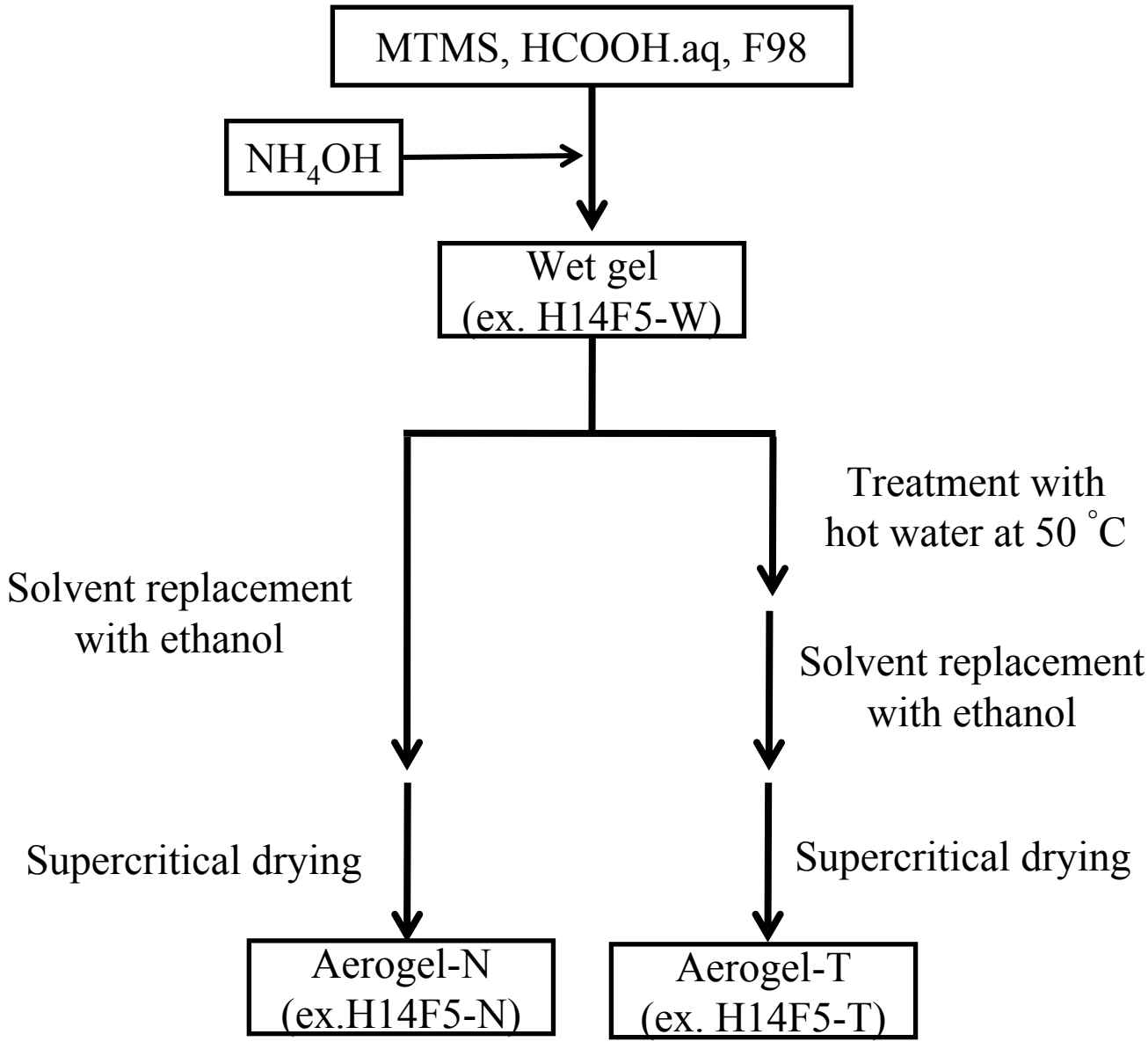

Figure1: Synthetic process for silica-based aerogels

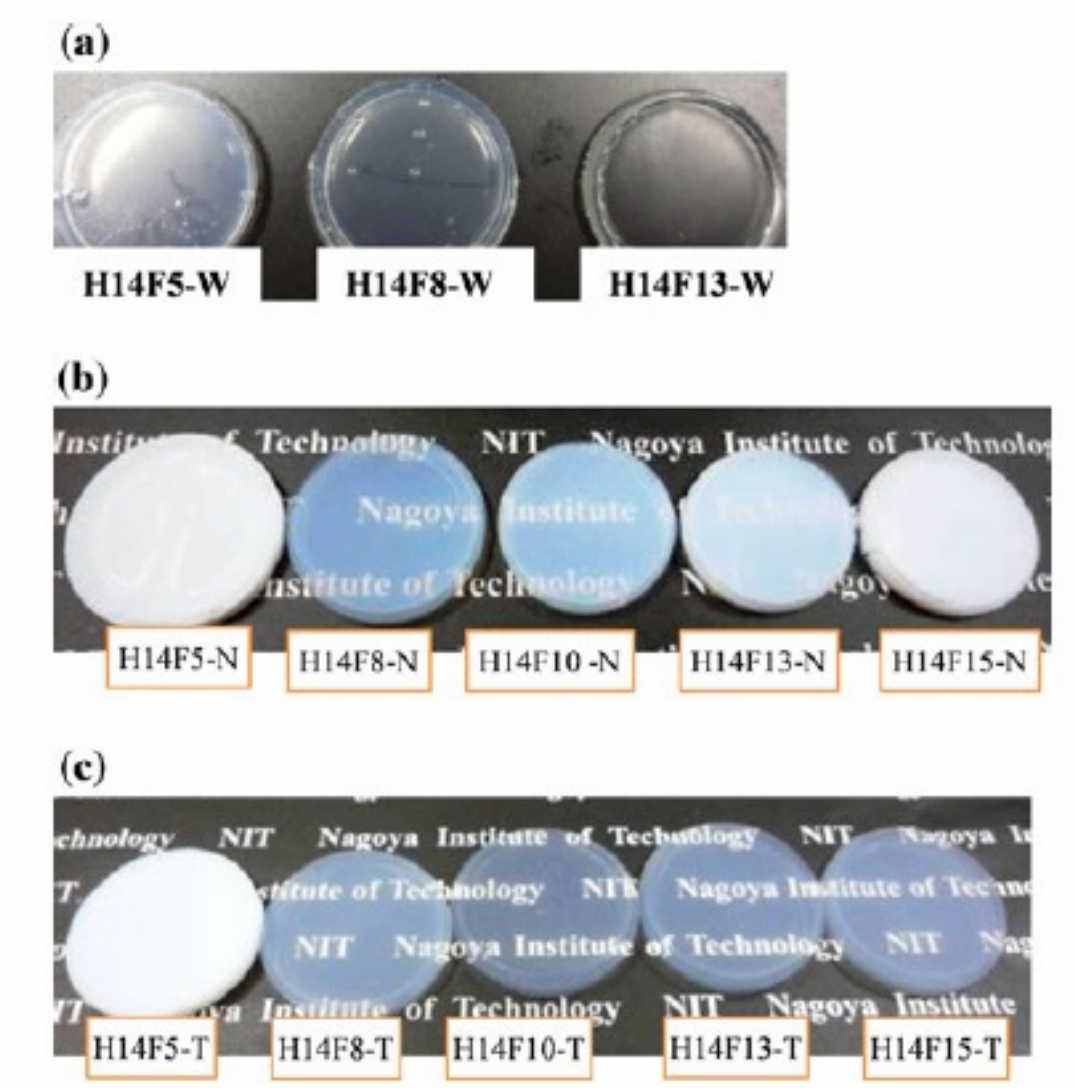

Figure 2: Wet-(H14F*x*-W) and aero-(H14F*x*-N and H14F*x*-T) gels prepared in this study. *x* is the amount of F98 surfactant, respectively, for MTMS.

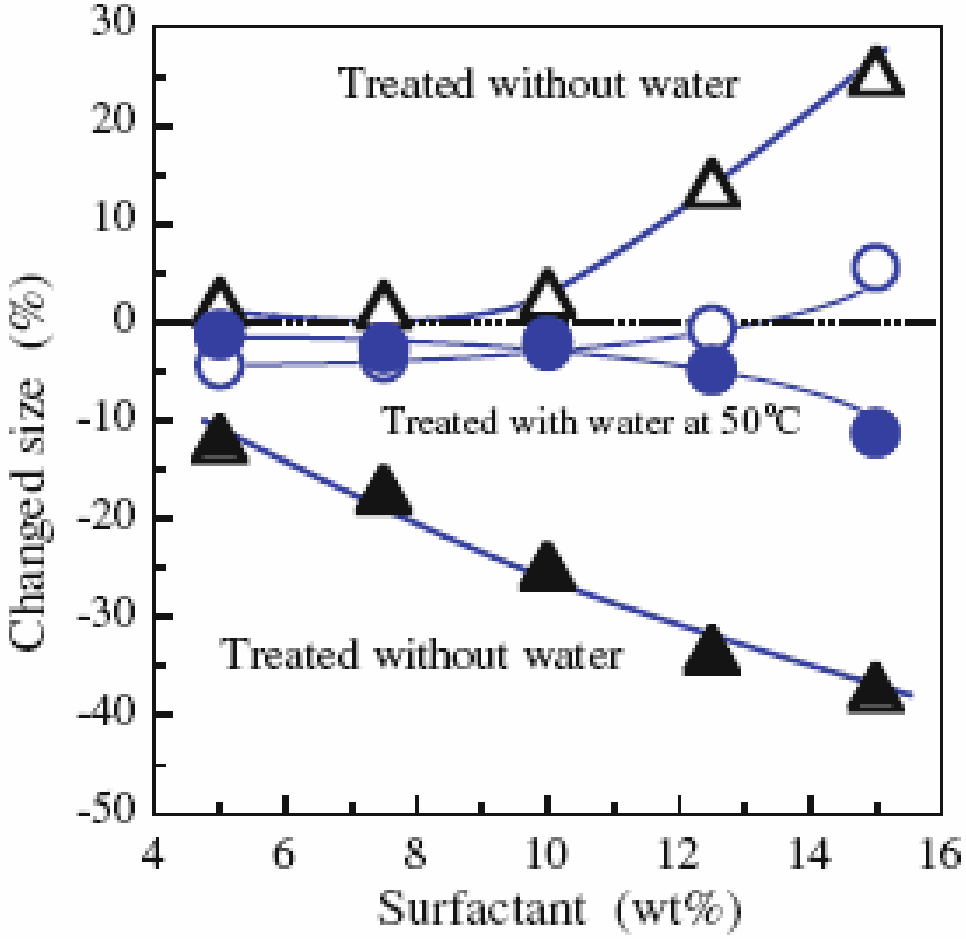

Figure 3: Rates of expansion (open marks) and shrinkage (closed marks) of gels during soaking in ethanol and supercritical drying, respectively. Aerogels were prepared with (circle, H14F*x*-T series) and without (triangle, H14F*x*-N series) soaking in hot water at 50 ˚C.

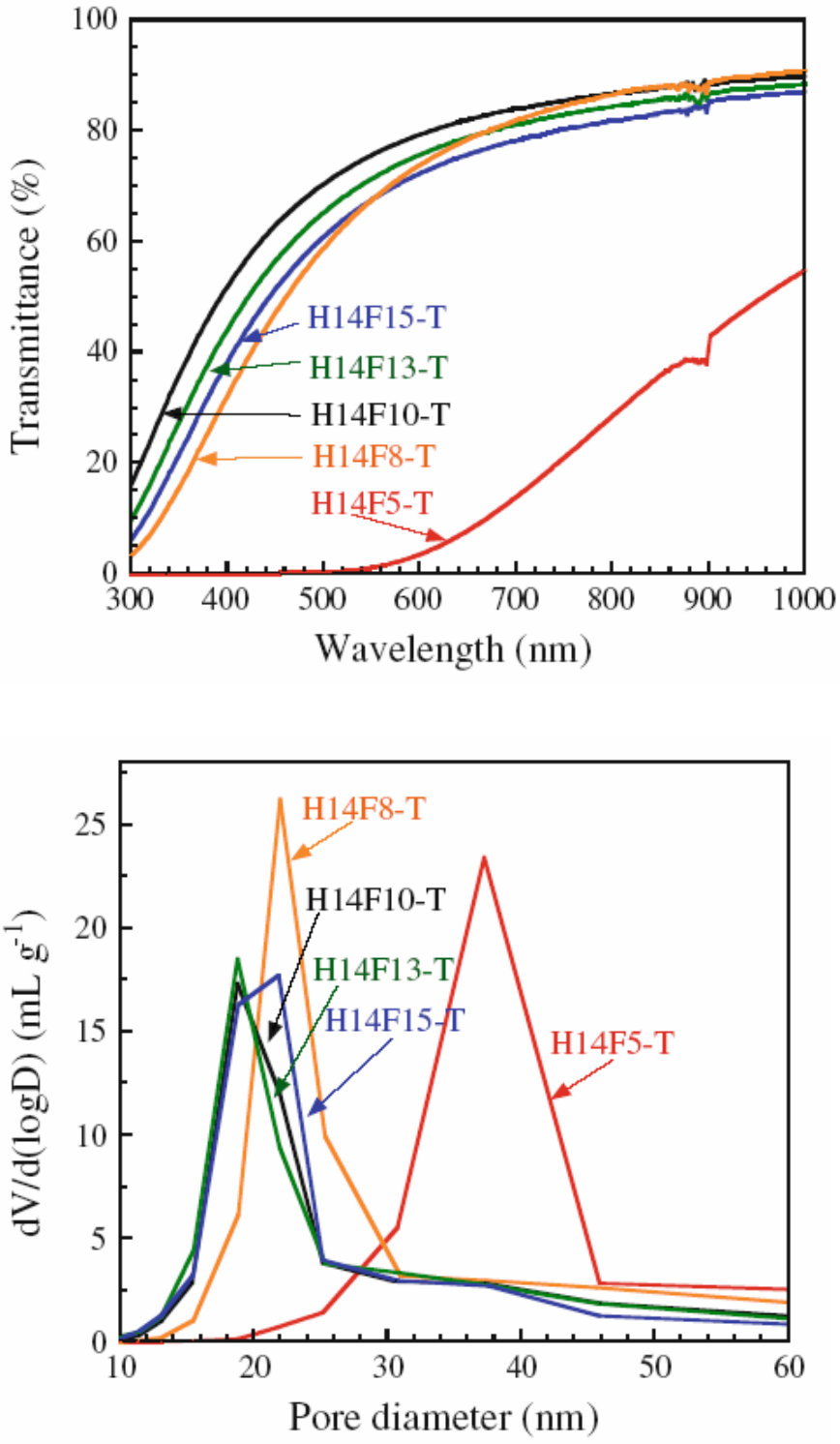

Figure 4: Optical transmittance spectra and pore size distribution curves for the aerogels prepared from the hot water-treated gels (H14F*x*-T series). Thickness of samples was 3 mm.

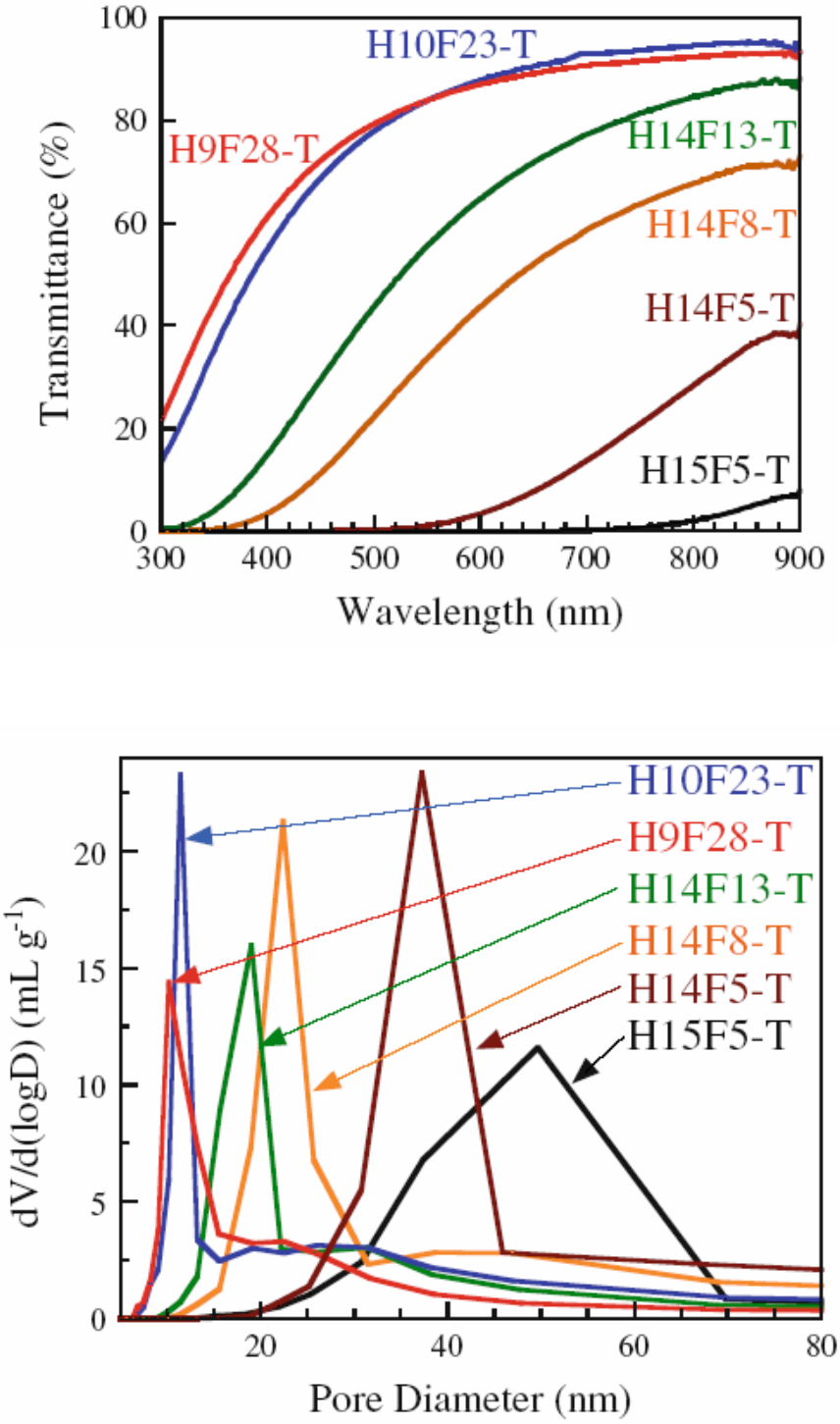

Figure 5: Optical transmittance spectra and pore size distribution curves for the aerogels prepared from the hot water-treated gels (HzF*x*-T series). Thickness of samples was 10 mm.

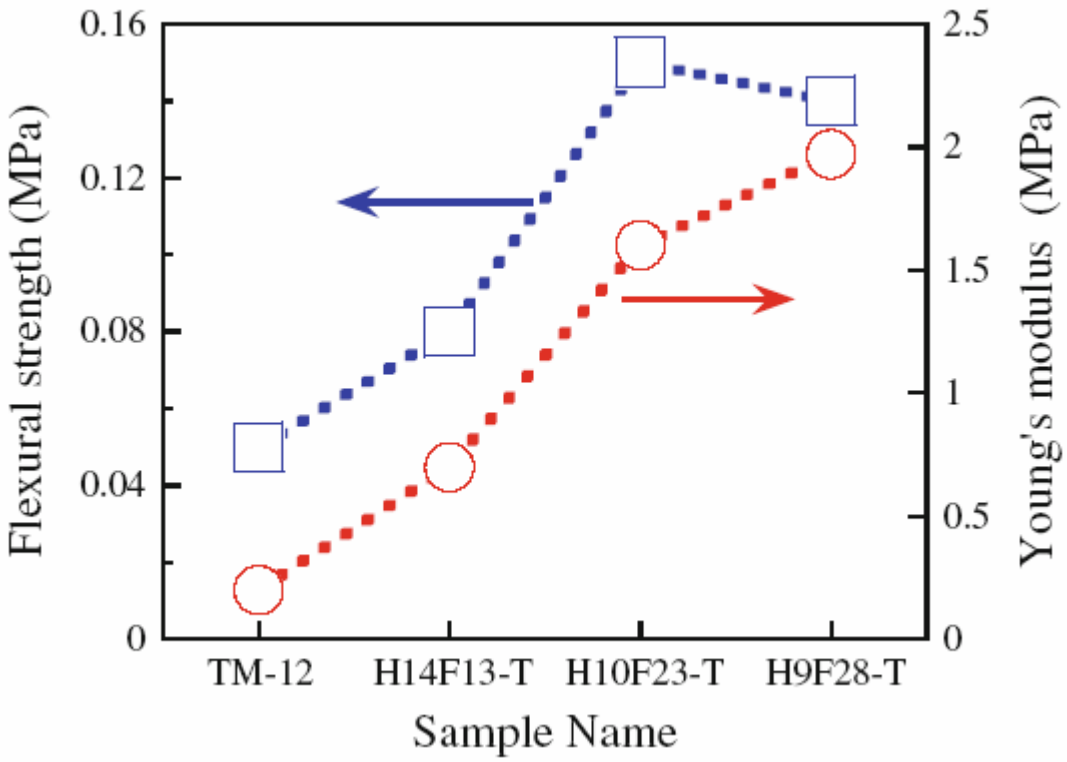

Figure 6: Bending strength and Young's modulus of the prepared aerogels. The aerogel (TM-12) prepared using TMOS instead of MTMS was compared.

Table 1: Preparation condition of aerogels and their physical properties

Sample	MTMS:H_2O (mol ratio)	Surfactant (wt%)	Specific surface area (m^2/g)	Pore volume (cm^3/g)	Mean pore diameter (nm)	Skeleton size (nm)	Transmittance (%)		Bending strength (N/mm^2)	Young's modulus (MPa)
							400 nm	600 nm		
H14F5-T	1:14	5	443	3.8	34		0.1	3.5		
H14F8-T	1:14	8	543	3.9	29	26	3.5	44		
H14F10-T	1:14	10	599	3.7	25					
H14F13-T	1:14	13	619	3.8	25	20	15	65	0.08	0.7
H14F15-T	1:14	15	647	3.7	23					
H15F5-T	1:15	5	370	3.0	33	40				
H10F23-T	1:10	23	726	3.7	20	19	55	88	0.15	1.6
H9F28-T	1:9	28	733	3.4	19	18	65	88	0.14	2.0

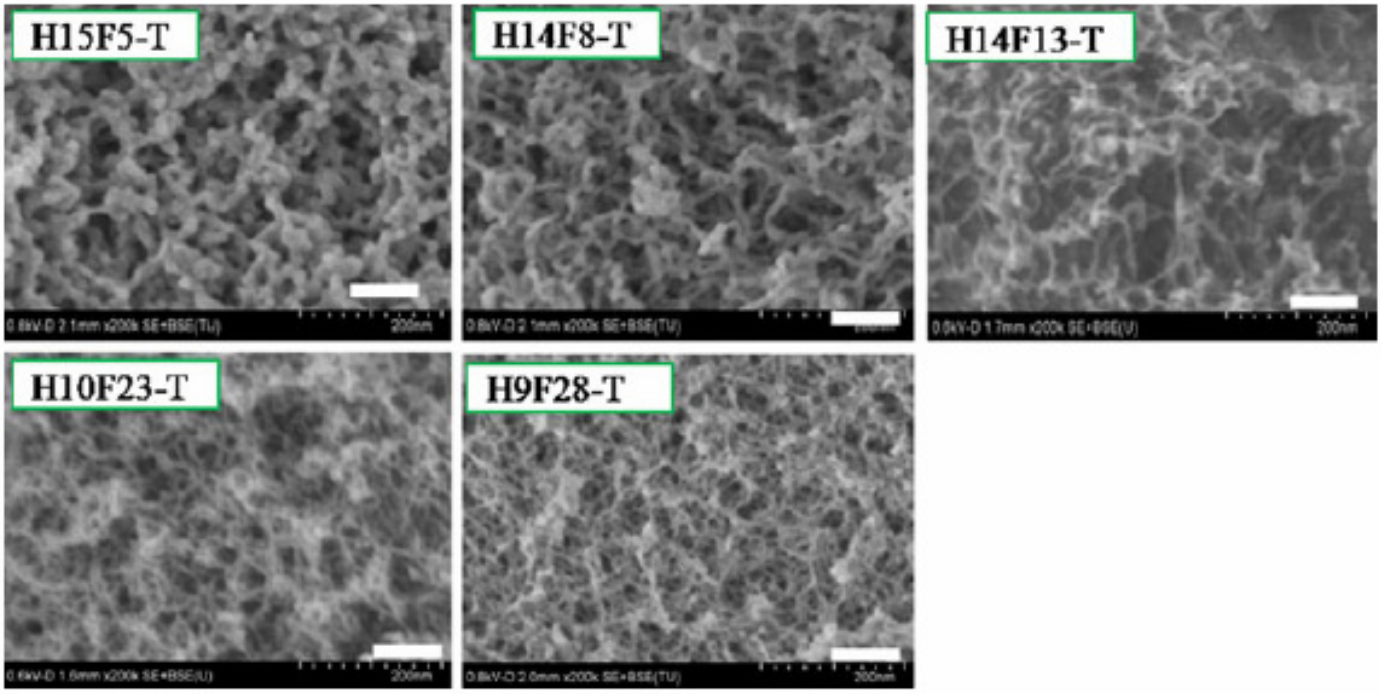

Figure 7: SEM images of the prepared aerogels

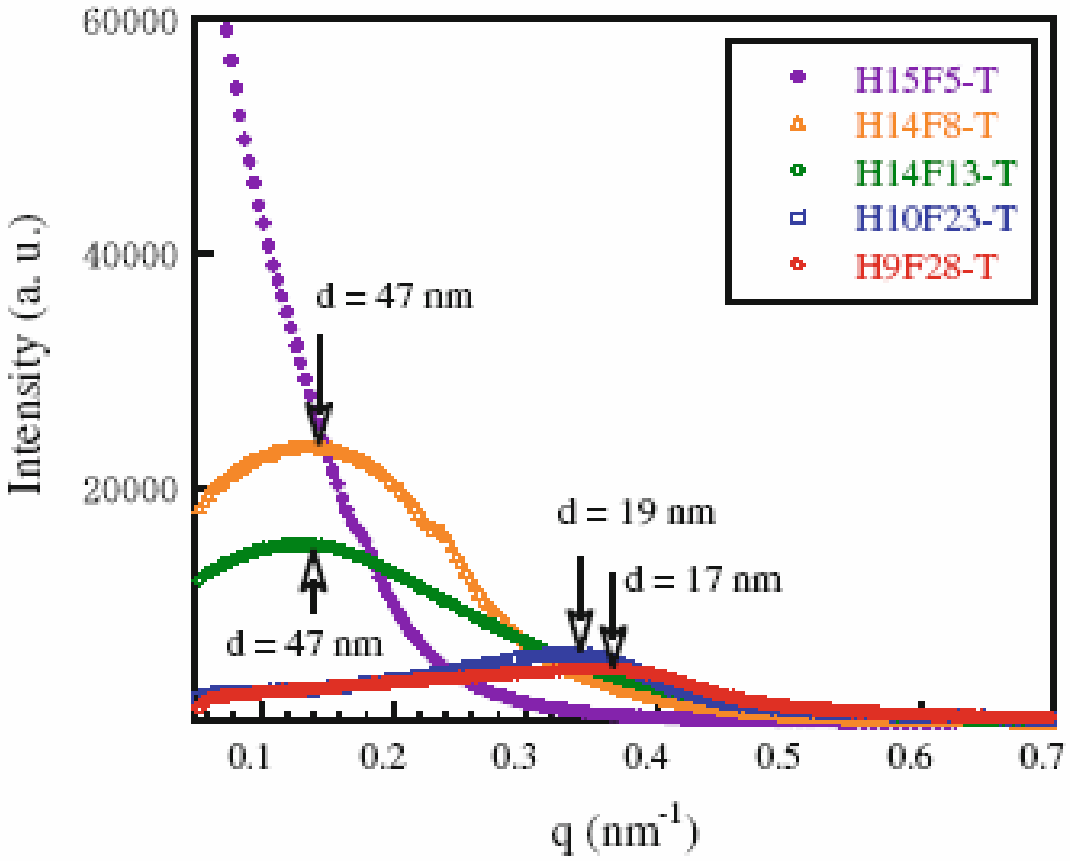

Figure 8: SAXS profiles of the prepared aerogels

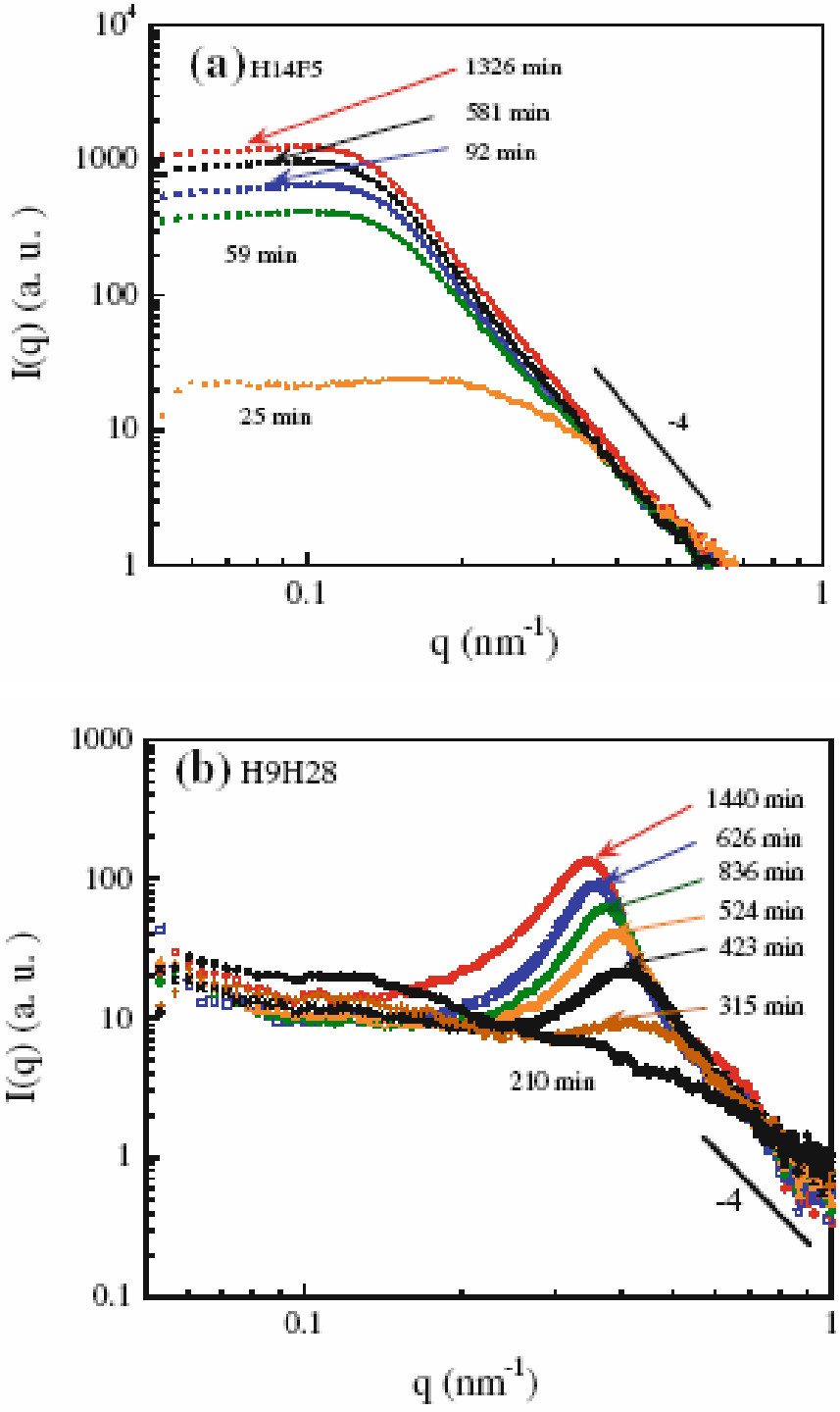

Figure 9: SAXS profiles of the hydrolyzed solution of (a) H14F5 and (b) H9F28.

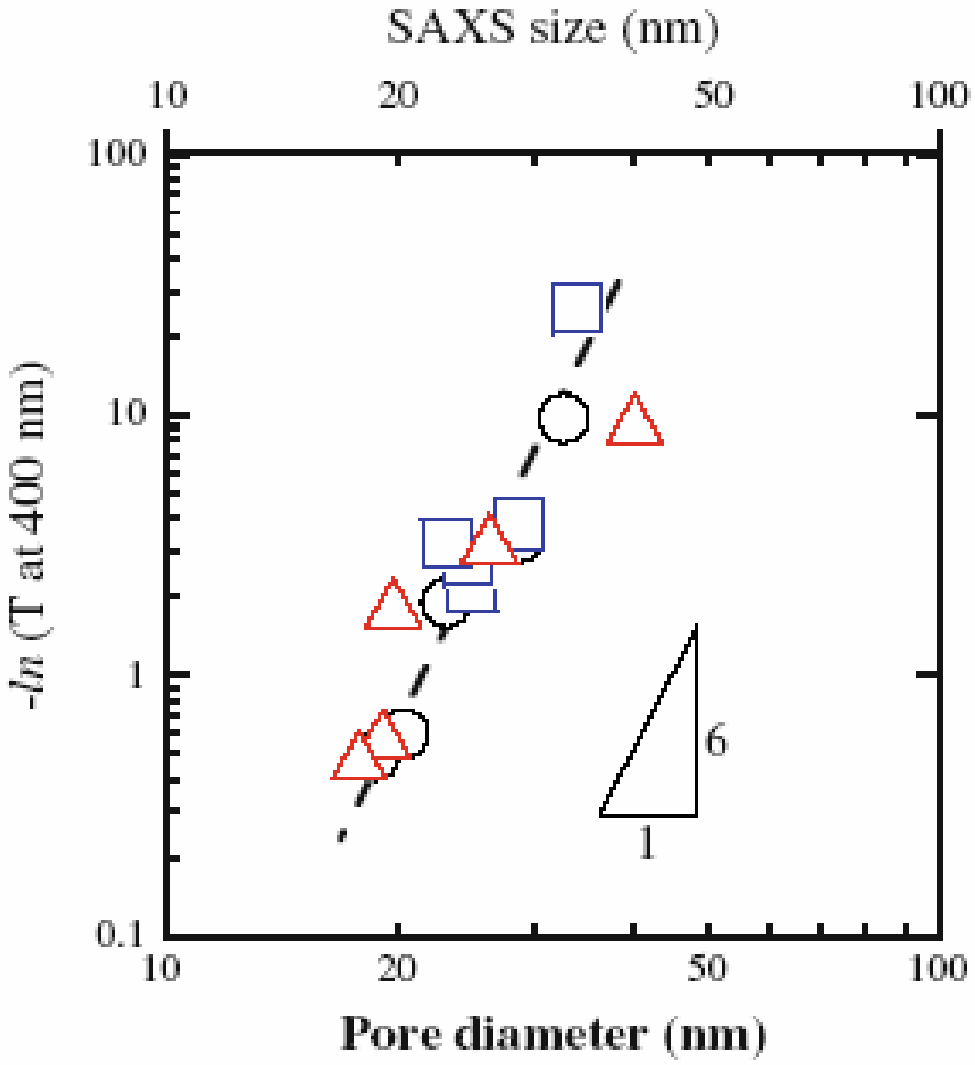

Figure 10: Relation between the transmittance (%) at 400 nm wavelength and pore size and skeleton size. Transmittance is scaled as the 6-power of the size.

CHAPTER 3

Thermal conductivity of silica aerogel under evacuated condition

1. Introduction

Silica aerogels are unique materials which are characterized by high porosity (> 90%) and fine porous structure with pore diameter smaller than 50 nm[1, 2]. Very low solid fraction and small sizes of fine pores suppress solid and gaseous conductivity, bringing the excellent thermal insulating properties. In addition, regardless of higher porosity than 90%, silica aerogel exhibits optical transparency due to fine porous structure. These key properties of aerogels lead to many applications including the super-insulating window for simultaneously satisfying transparency and thermal insulation. Super-insulating windows have the stacking structure of silica aerogel and glass and their thermal insulating property is determined by thermal conductivity and thickness of silica aerogels. When prepared with thicker silica aerogels, insulating property of super-insulating window is improved whereas the optical transparency is reduced due to the increase of light scattering of silica aerogel.

For designing of super-insulating window, accurate value of thermal conductivity and optical transmission of silica aerogel is essential. Especially, it is difficult to measure the thermal conductivity of silica aerogel accurately because the reference material, exhibiting as low thermal conductivity as silica aerogel, does not exist. Guarded hot plate (GHP) technique is a measurement method to offer the absolute value of thermal conductivity without reference

material. In this paper, aerogels with different density are prepared by controlling the starting composition and the effect of density and thickness on thermal conductivity of silica aerogel is examined by GHP method.

2. Experimental

2.1 Synthetic procedure of silica aerogels

Methyl silicate 51 (MS), silicon oligomer with molecular weight of 470 (tetramer), was used as silica source. All the gels were prepared by mixing together two solution, A and B, with ice cooling to retard the gelation. Solution A contained given amounts MS in ethanol; Solution B contained an equal amount of ethanol and aqueous ammonia water (0.1 mol/L). The density of silica aerogel is controlled by changing the amounts of ethanol in starting composition. The wet gel was aged at 50˚C for 2 days to complete condensation. For methylation, the resultant wet gels were solvent-exchange with 0.2 mol/L of 1, 1, 1, 3, 3, 3–hexamethyldisilazane ethanol solution at room temperature and with ethanol for 3 times each for more than 8 h. Resultant alcogels were dried from supercritical carbon dioxide at 50˚C, 12 MPa in an autoclave (SCRD6, Reexam co., Ltd).

2.2 Characterization of silica aerogels

The porous morphology was observed under a field emission scanning electron microscope (FE-SEM), SU8000 (Hitachi Ltd). Bulk density was obtained by measuring the volume and weight of gel. Nitrogen sorption measurements

were performed to obtain pore size distribution with BELSORP-mini (BEL JAPAN, Inc.). Samples were outgassed under vacuum at 200 ˚C for at least 1 h prior to measurement. For light transmittance, a UV-VIS-NIR spectrometer Lambda 950 (Perkin Elmer) equipped with an integrating sphere was employed.

Thermal conductivities of monolithic aerogels were measured with an evacuable guarded hot plate apparatus GHP 456/3/1 Titan (NETZCH). Each measurement was performed at a temperature difference of 10 K and measurement temperature of 25 ˚C in the pressure range from 1 Pa to atmospheric pressure (10^5 Pa).

3. Result and Discussion

3.1 Morphology of silica aerogels

Figure 1 shows the FE-SEM images of silica aerogels with density of 0.10 $g \cdot cm^{-3}$. Silica aerogels possesses skeletons of aggregated globules and small pores (10 to 30 nm, mesopores). All silica aerogels in this study have similar structure to aerogel with density of 0.10 $g \cdot cm^{-3}$. From nitrogen sorption measurement, it is also confirmed that the silica aerogel have the similar pore structure; the average pore size of aerogels with density of 0.13, 0.11, 0.10 $g \cdot cm^{-3}$ is 28, 28, 25 nm, respectively.

Figure 2 display the visible light transmittance, *T*, as a function of wavelength for aerogels with different thickness. An increase in transmittance with decreasing thickness of aerogels is observed. One can see that the transmittance of gels decrease with decreasing wavelength, which is attributed

to the Rayleigh scattering. According to the Rayleigh theory[3], absorption coefficient is proportional to the scattering centre dimension (diameter of fine particle) with the power of 6, which influenced susceptibly by the morphology of silica aerogels. Absorption of coefficient, α, is calculated as follows; $T = \exp(-\alpha L)$, where L is the sample thickness. Calculated α at 550 nm, listed in inset of Figure 2, shows almost same value, suggesting that aerogels with different thickness have the similar morphology.

3.2 Effect of density on thermal conductivity of silica aerogels

Figure 3 illustrates the pressure dependence of thermal conductivity for silica aerogels with different density. A decrease in thermal conductivity of silica aerogels with reducing gas pressure up to 10^4 Pa is observed. Below the pressure of 10^4 Pa, thermal conductivity of aerogel exhibits constant value. Apparently, both evacuated aerogel and non-evacuated aerogel shows the density dependence of thermal conductivity.

Relation thermal conductivity of aerogels measured under atmospheric and evacuated condition with density was shown in Figure 4. Thermal conductivities of aerogels measured under atmospheric and evacuated condition shows minimum value at the density of 0.14 and 0.10 $g \cdot cm^{-3}$, respectively, which coincides with optimal density predicted theoretically for minimum thermal conductivity of silica aerogels; non-evacuated and evacuated aerogel is 0.15 and 0.11 $g \cdot cm^{-3}$,respectively[4].

In porous material, heat transfer occurs via solid, gas and radiation. Since the gas pressure affect only gaseous conduction among these heat transfer

mechanisms, the difference in thermal conductivity between evacuated and non-evacuated aerogel indicate the contribution of gaseous conduction. As mentioned above, optimal density for minimum thermal conductivity measured at atmospheric pressure is higher than that measured under evacuated condition, indicating the gaseous conduction increases with decreasing density mainly due to increase the porosity.

3.3 Effect of thickness on thermal conductivity of silica aerogels

Figure 5 shows the thickness dependence of thermal conductivity for evacuated and non-evacuated aerogels with density of 0.13 g·cm^{-3}. Apparently, both of thermal conductivity measured under evacuated and atmospheric condition is affected by thickness. Thermal conductivity increase with increasing thickness and tends to saturate above 10 mm for 0.13 g·cm^{-3} aerogel. Since not only evacuated aerogel but also non-evacuated aerogel shows thickness dependence of thermal conductivity, gas conduction has little effect on this phenomenon.

Under evacuated condition, the mechanism of heat transfer was treated as the combination of solid and radiative conduction. Taking into account heat transfer at the boundary by radiation due to low extinction coefficient of aerogel, E, the effective thermal conductivity, λ_{eff}, is given by;

$$\lambda_{\mathrm{eff}} = \lambda_{\mathrm{s}} + \frac{4 \cdot n^2 \cdot \sigma \cdot T_{\mathrm{m}}{}^3}{\frac{2/\varepsilon - 1}{d} + 3/4 \cdot E} \quad (1),$$

where λ_{s} is solid conduction, n is refractive index (~1 for aerogel), σ is Stephan-Boltzmann constant (5.67×10^{-8} W/m^{2}K^4), T_{m} is the mean temperature

within the materials (298 K), ε is the emissivity of aerogel, and *d* is the thickness of aerogel. The curve of thickness dependence of thermal conductivity for evacuated aerogel (Figure 6) is reasonably reproducible by eq. (1), which gives E = 1870 m^{-1}, ε = 0.18 and λ_s = 0.0042 $W \cdot m^{-1} \cdot K^{-1}$. The value of E is comparable to reference data determined by the Infrared optical transmission measurement[5]. The value of ε is lower than that of typical silica (~ 0.7 to 0.9), presumably due to the poor absorption at the boundary of silica aerogel. λ_s is higher than radiative conduction (λ_{eff} minus λ_s, 0.026 $W \cdot m^{-1} \cdot K^{-1}$) for aerogel with 0.13 $g \cdot cm^{-3}$. For further improvement of effective thermal conductivity under evacuated condition, reducing the solid conduction is effective.

4. Conclusion

Silica aerogel has been prepared with different density and thickness by controlling the starting composition and influence of density and thickness on thermal conductivity under evacuated and atmospheric condition is examined. FE-SEM observation and nitrogen adsorption confirm that aerogel with different density have similar pore diameter. Absorption coefficient calculated by optical transmittance reveals that aerogels with different thickness have similar morphology. Measurement of thermal conductivity of aerogels indicate non-evacuated and evacuated aerogel shows minimum value at the density of 0.14 and 0.10 $g \cdot cm^{-3}$, respectively. For evacuated aerogel as well as non-evacuated aerogel, thickness dependence of thermal conductivity is observed, which is attributed to low extinction coefficient of silica aerogel.

Reference

[1] S. S. Kistler, *Nature* **127** (1931), p. 741.

[2] J. Fricke and A. Emmerling, *Journal of the American Ceramic Society* **75** (1992), p. 2027.

[3] M. Kerker, The scattering of Light, Academic Press, New York (1969).

[4] L. W. Hrubesh and R. W. Pekala, *Journal of Materials Research* **9** (1994), p. 731.

[5] X. Lu, M. C. Arduini-Schuster, J. Kuhn, O. Nilsson, J. Fricke and R. W. Pekala, *Science* **255** (1992), p. 971.

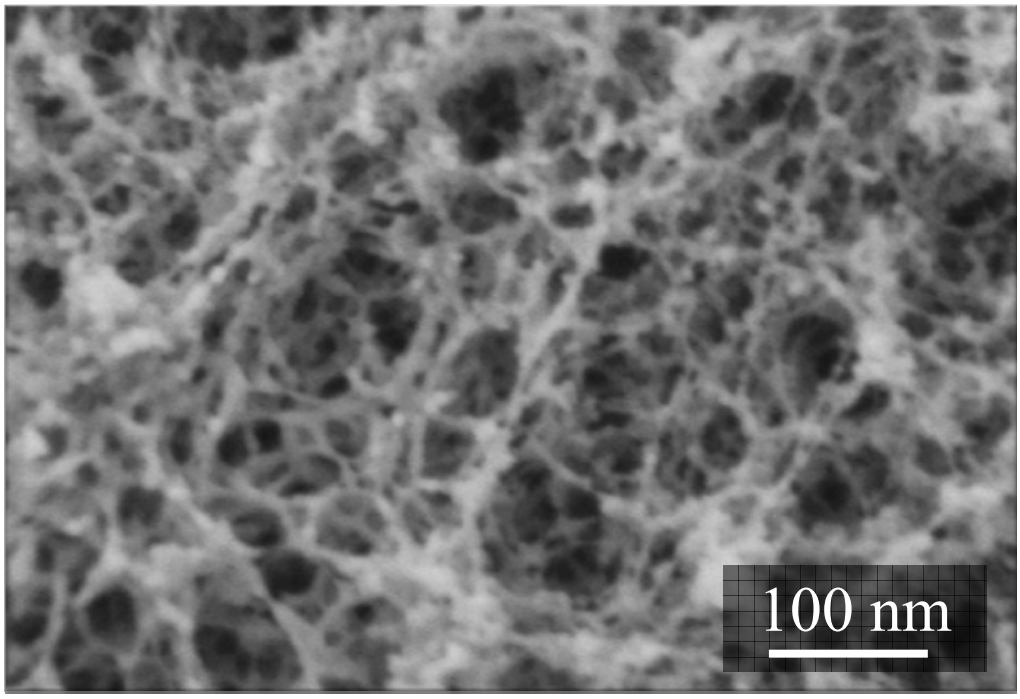

Figure 1: FE-SEM image of silica aerogel with density of 0.10 g·cm^{-3}

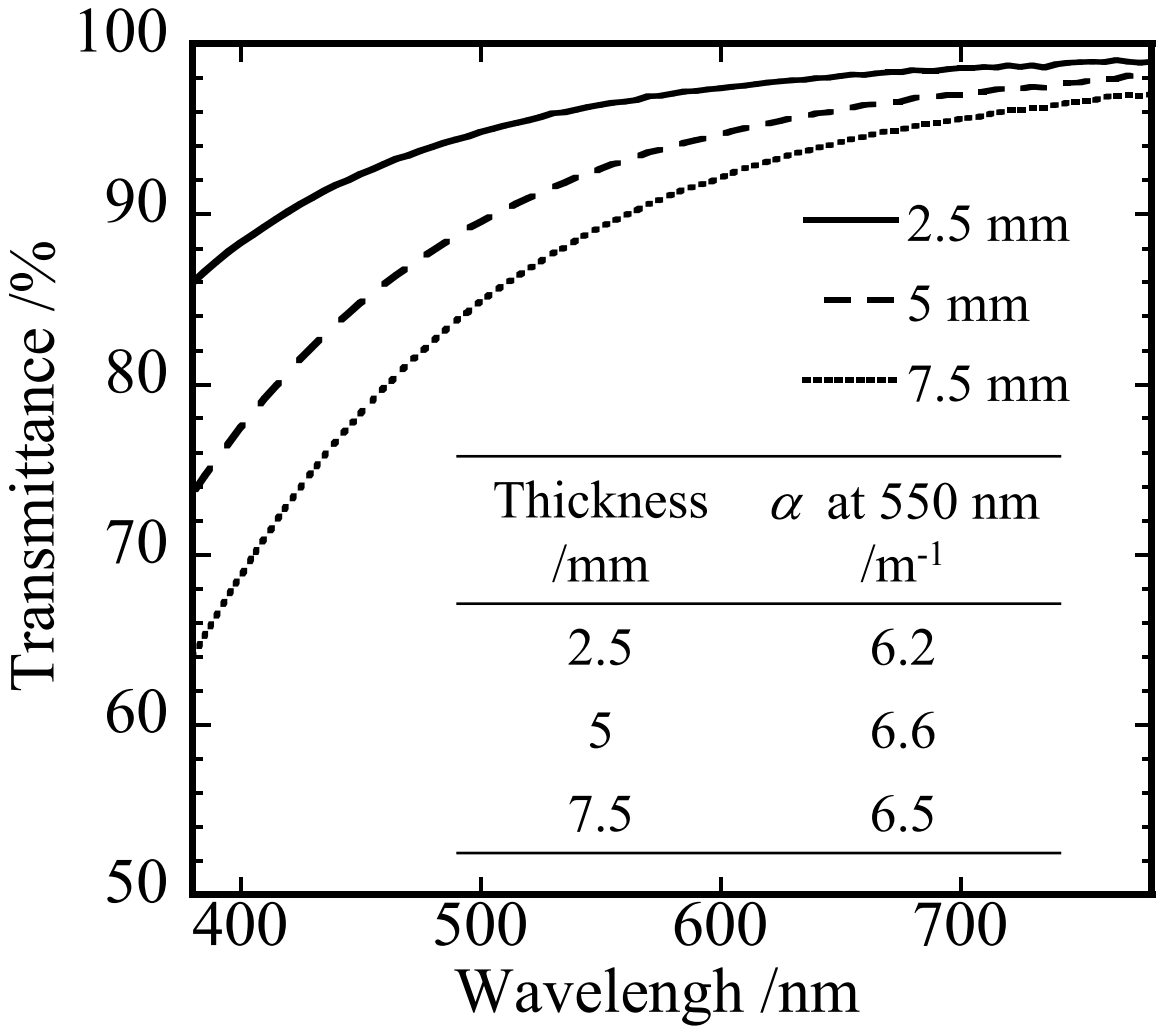

Figure 2: Visible light transmittance as a function of wavelength for aerogels with different thickness.

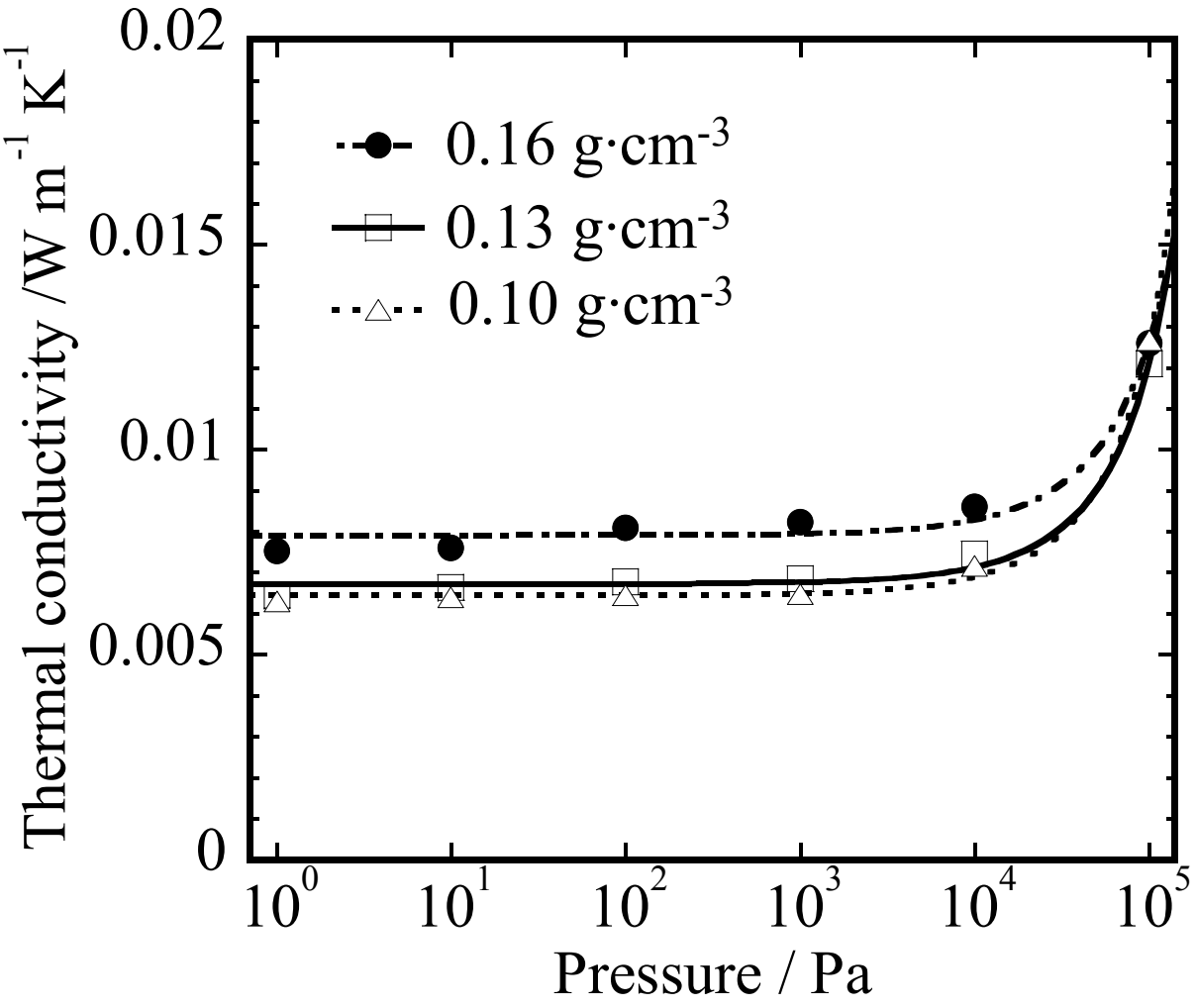

Figure 3: Pressure dependence of thermal conductivity of silica aerogels with different density.

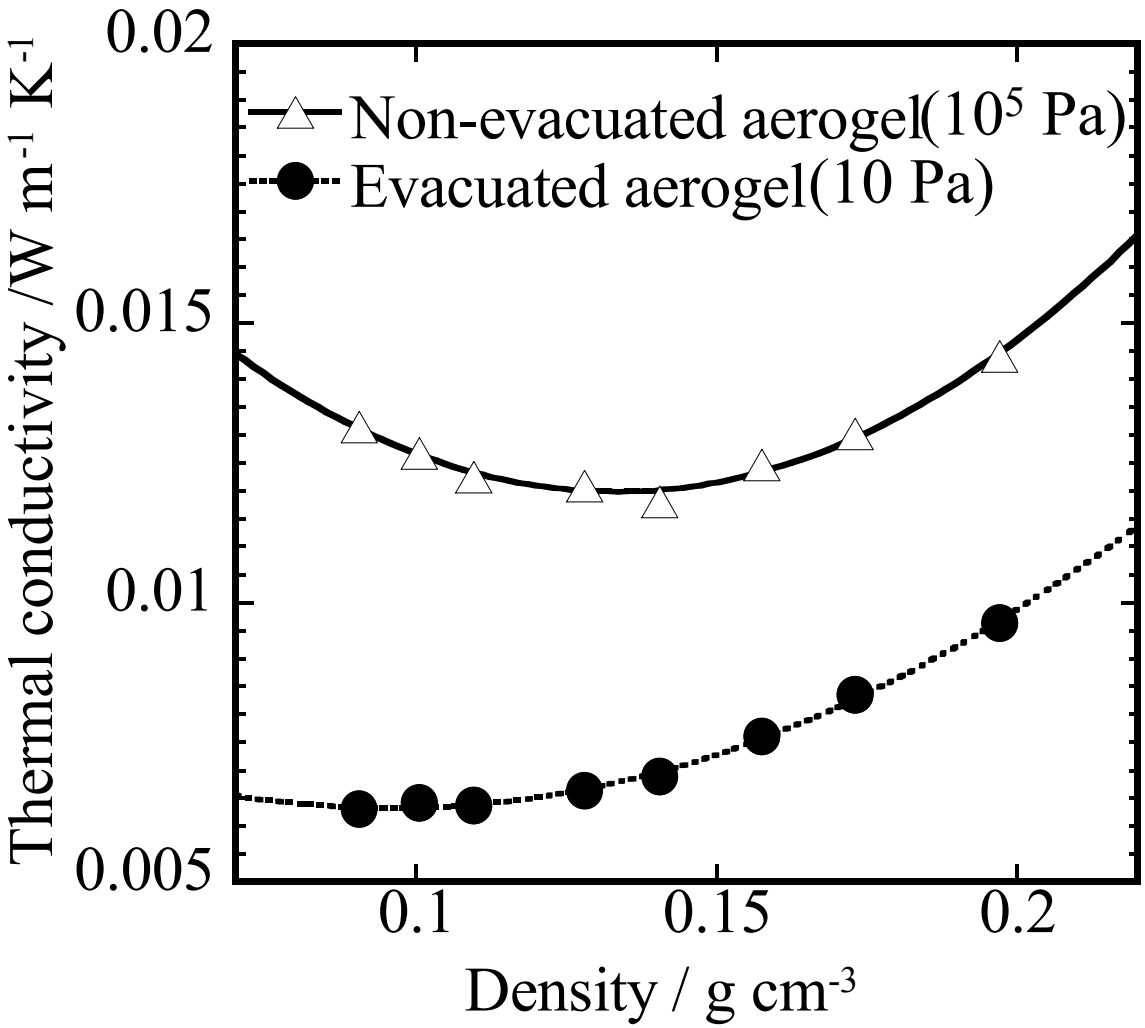

Figure 4: Relation thermal conductivity with density for evacuated and non-evacuated aerogel.

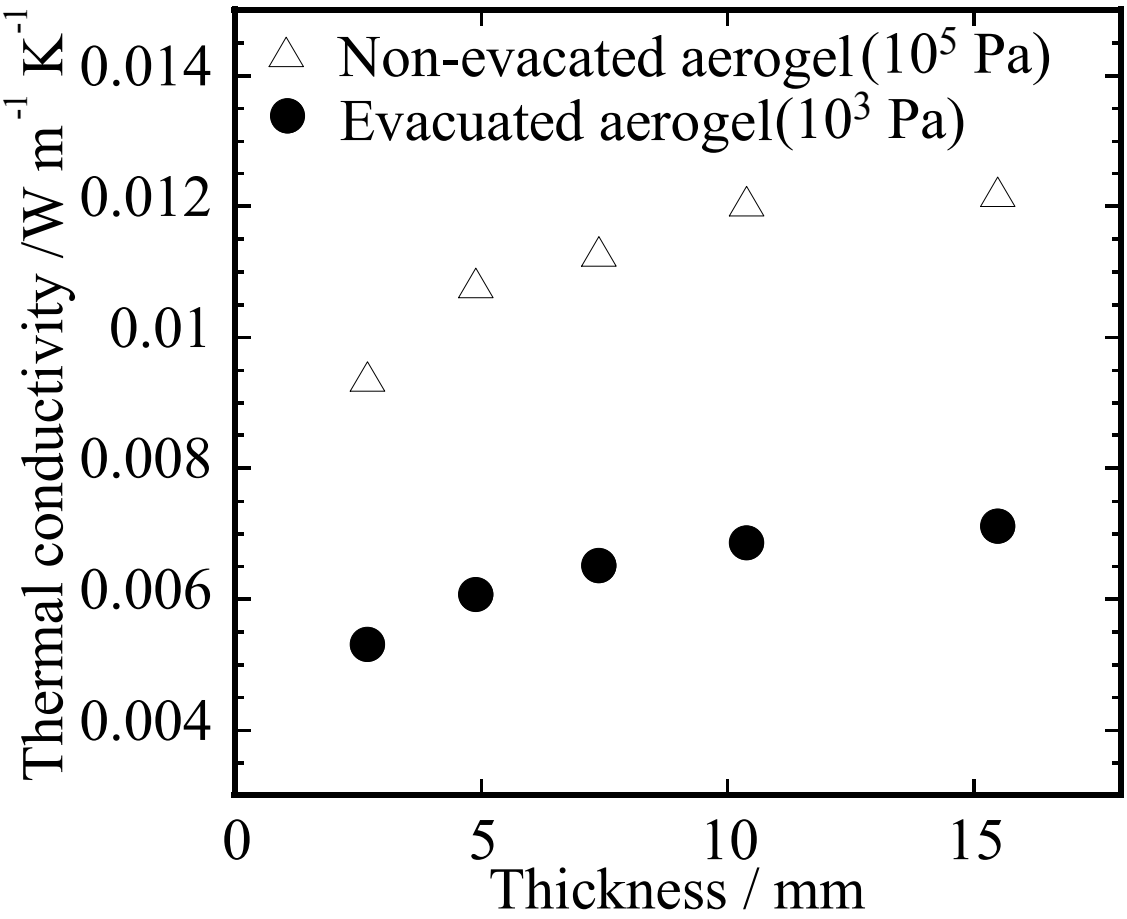

Figure 5: Thickness dependence of thermal conductivity for non-evacuated aerogel and evacuated aerogel.

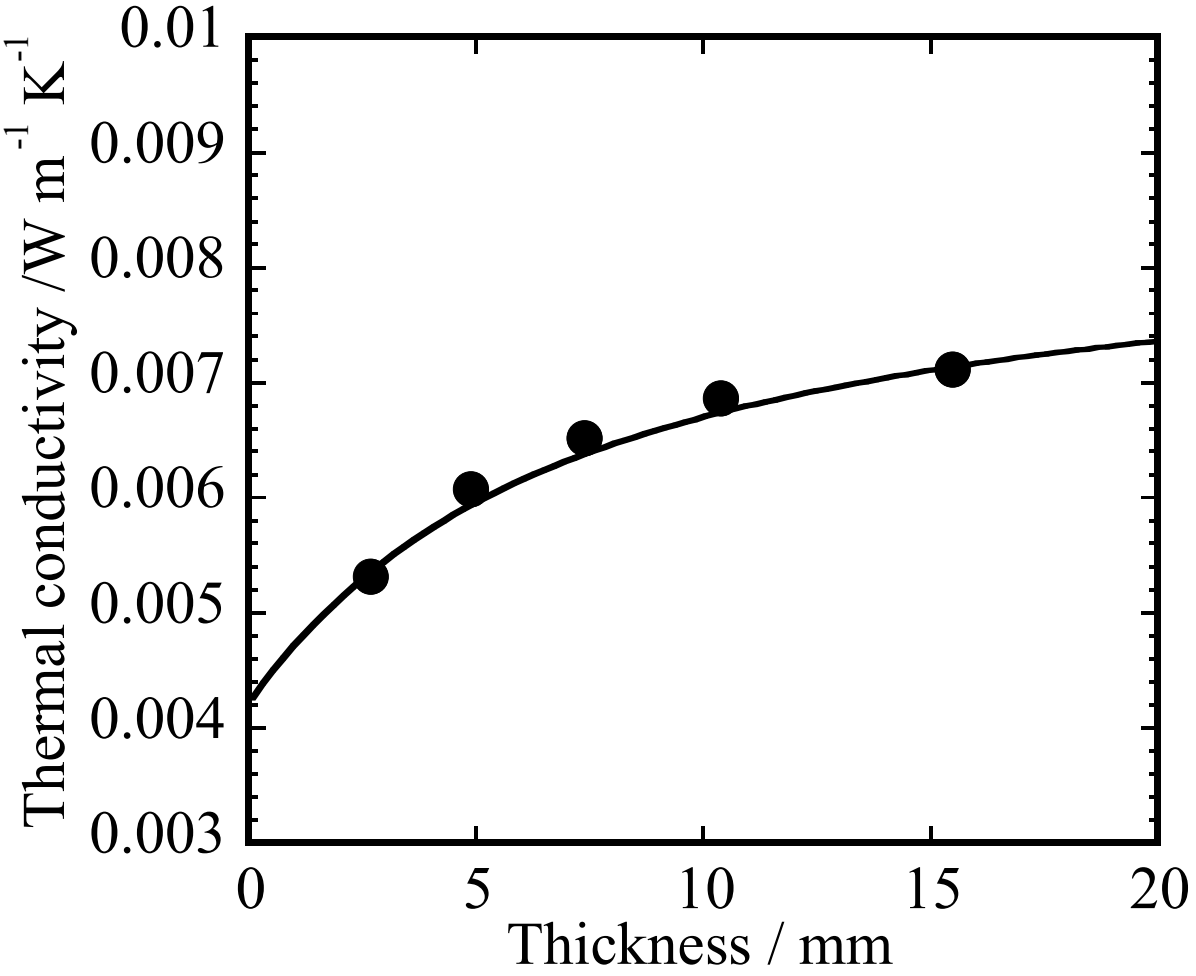

Figure 6: Variation of thermal conductivity of evacuated aerogel with density (closed circle). Solid line is drawn by fitting experimental data with theoretical curve.

CHAPTER 4

Fabrication and characterization of evacuated aerogel glazing

1. Introduction

Window in a building have a major influence on space heating demand and indoor environment both with respect to climate and daylight. Windows are still thermally weakest part of the thermal envelope but on the other hand allow the use of solar heat and daylight. In the continuing effort to lower the heat loss from buildings window glazing have been significantly improved. The *U*-value has been reduced by the introduction of insulating gas fillings and almost invisible low-E coatings to reduce heat transfer by long-wave radiation. As a example, the U-value for a sealed double-layer glazing has been reduced from 3.0 W / (m^2·K) (12 mm air-filled enclosure) to 1.1 W / (m^2·K) (15 mm argon filling enclosure and low-E coating). Further limited improvement can be achieved by the use of krypton filling. If the *U*-value should be further reduced an additional layer of glass and an additional low- E coating has to be applied. In this case the *U*-value can be lowered to approximately 0.5 W / (m^2·K). However, both the additional layer of glass and additional low-E coating also reduced the solar gain and daylight transmittance. Furthermore, the additional layer of glass increases the weight of the glazing by 33% and requires stronger window frames than those used for double-glazed solutions. In the search for further energetic improvement of window glazing, especially two different advanced glazing solutions have been investigated, vacuum glazing and the evacuated aerogel

glazing. Vacuum glazing consists of two sheets of glass with a distance of approximately 0.5 mm[1, 2]. The glazing is sealed at the edges and the space between the glasses panes are evacuated to a fine vacuum in the range of 0.01 Pa. The glass panes are kept apart by means of regular distributed small pillars. Both the glass surfaces facing the enclosure are low-E coated to reduce thermal radiation between the glass panes to a minimum. The *U*-value of vacuum glazing is in the same range as that of triple glazed sealed glazing units with argon filling, but has the advantage of lower weight and the slimness that makes vacuum glazing feasible as a replacement for single glazing. The drawback is the large thermal bridge in the edge sealing as it has to be completely airtight and has a thickness of only approximately 0.5 mm. The evacuated aerogel glazing is a double-pane sealed glazing unit, where traditional gas filling is replaced by monolithic silica aerogel, which is a highly porous and transparent material with pore sizes in the range 10 to 50 nm. The small pore makes it possible to achieve an apparent thermal conductivity below 0.010 W / (m·K) combined with a highly solar energy and daylight transmittance. These two characteristics make the monolithic silica aerogel very interesting for super-insulating window glazing units.

2. Experimental

2.1 Material

Metylsilicate 51(MS) was purchased from Colcoat co., Ltd. Ethanol and 1 mol/L ammonia solution were from Nacalai tesque, inc. and Kanto chemical co.

Ltd, respectively. 1, 1, 1, 3, 3, 3-Hexamethyldisilazane was obtained from Wako pure chemicals, Ltd. The float glass and low emissivity (Low-E) glass were from Asahi Glass co., Ltd.

2.2 Preparation of aerogel

The aerogel was prepared by sol-gel method and subsequent CO_2 supercritical drying method. Methyl silicate 51 (MS), silicon oligomer with molecular weight of 470 (tetramer), was used as silica source. All the gels were prepared by mixing together two solution, A and B, with ice cooling to retard the gelation. Solution A contained given amounts MS in ethanol; Solution B contained an equal amount of ethanol and aqueous ammonia water (0.1 mol/L). The density of silica aerogel is controlled by changing the amounts of ethanol in starting composition. The wet gel was aged at 50˚C for 2 days to complete condensation. For methylation, the resultant wet gels were solvent-exchange with 0.2 mol/L of 1, 1, 1, 3, 3, 3–hexamethyldisilazane ethanol solution at room temperature and with ethanol for 3 times each for more than 8 h. Resultant alcogels were dried from supercritical carbon dioxide at 50˚C, 12 MPa in an autoclave (SCRD6, Reexam co., Ltd).

2.3 Fabrication of aerogel glazing

Three PVC spacer with the length of 20 cm is assembled to become U-shape. Four tiles of aerogel ($95\times95\times10$ mm^3) is set inside the space surrounded by spacers. Opened one side is also covered with PVC spacer and each end is fixed by butyl tape. The sheet of float glass ($220\times220\times2.75$ mm^3) is fixed on

the spacer with the butyl tape. After turning upside down the sample, the butyl tape is placed on the spacer similarly. Subsequently, the sample is placed into custom-built vacuum inclusion device. Followed by sliding a Low-E glass attached to the chamber cover by using electrostatic chuck above the sample, the chamber is closed. The glass is arranged with the plane coated with Low-E thin film facing inward. The closed chamber is evacuated into until given pressure and is maintained same pressure condition for 10 minutes. Then, the mechanical pressure is applied at the surface of glass plate by raising the height of the board mounted sample on, leading to adhesion between glass and spacer. Applied mechanical pressure in this study is 100 kPa. After leakage until atmospheric pressure, the load is gradually removed by lowering the height of the board placed sample on. In order to seal the vacuum condition tightly, the silicon resin is filled in the outer space surrounded by the glass and spacer (Figure 1).

2.4 Characterization

Heat insulating performance of aerogel is evaluated by heat transmission coefficient, *U*, which is defined as follows:

$$U = 1/(1/h_e + 1/h_t + 1/h_i) \quad (1),$$

where h_e is the external heat transfer coefficient, h_t is the conductance of aerogel glazing, and h_i is the internal surface heat transfer coefficient.

For optical properties of aerogel glazing, a UV-VIS-NIR spectrometer Lambda 950 (Perkin Elmer) equipped with an integrating sphere is employed. The haze ratio is calculated as follow; Haze = *T*4/*T*2 × 100, where *T*2 is

Direct-hemispherical transmittance and *T*4 is Normal-diffuse transmittance.

3 Result and Discussion

Fig.2 displays contour lines of thickness for aerogel glazing using spacer thickness of (a) 10 mm, (b) 9.5 mm and (c) 9 mm, respectively. The samples with spacer of 10 mm and 9.5 mm have concave shape toward the center. On the other hand, aerogel glazing with thickness of 9 mm bowed outward.

U-value and thermal conductivity of aerogel glazing is summarized in Table 1. Thermal conductivity of aerogel inside the panel can be calculated by using the thickness of aerogel and glass and thermal conductivity of glass (1 $W \cdot m^{-1} \cdot K^{-1}$). Thermal conductivity of aerogels is close to that measured under evacuated condition (10 Pa), 0.0066 $W \cdot m^{-1} \cdot K^{-1}$. This result implies that panel using MS8M keeps the vacuum condition. Aerogel glazing of 08-10 shows the lowest thermal transmission coefficient at the center, U_{center}, of 0.623 $W \cdot m^{-2} \cdot K^{-1}$, which is comparable to evacuated aerogel glazing fabricated by J. M. Schultz *et al*[3].

Fig.3 (a) shows the direct-hemispherical transmittance of Aerogel glazing (08-10). For comparison, the curve of aerogel (MS8M) and Low-E glass was shown. Aerogel glazing is transparent in visible range (380 nm – 780 nm) and its transmission at 550 nm shows 63.2%. In the wavelength lower than 400 nm, aerogel glazing does not transmit the light. In addition, it is found that the transmission of infrared light, in the wavelength longer than 800 nm, for aerogel glazing does not occur due to reflection of Low-E glass.

Fig.3 (b) illustrates the diffusive transmission of aerogel, aerogel glazing and

Low-E glass. Apparently, an increase of the diffusive transmission especially in shorter wavelength range of aerogel glazing is observed. This increase is attributed to the Rayleigh scattering of pore and skeleton in aerogels[4, 5].

The transmission at 550 nm and haze ratio measured at regular interval on diagonal line was shown in Fig.4. Fig.4 (a), (b), and (c) correspond to the spacer thickness of 10 mm, 9.5 mm and 9 mm, respectively. The transmission of 08-10 and 08-9.5 decreases toward center of sample while that of 08-9 shows similar value all over the sample. Haze ratio of 8-10 decreases toward center and that of 8-9.5 shows similar behavior. Meanwhile, as for 8-9, the increase in haze ratio toward center of aerogel glazing is observed.

Thermal conductivity of aerogel glazing using MS8M (8-10, 8-9.5, 8-9) shows almost constant value of 0.012 $W \cdot m^{-1} \cdot K^{-1}$. This value is related to the thermal conductivity of aerogel inside the aerogel glazing. Assuming that the heat transfer of panel sample was carried out in series, thermal conductivity of aerogel inside the panel was calculated. The thermal conductivity of aerogels for 8-10, 8-9.5, 8-9 is 0.0075, 0.0078, 0.0077 $W \cdot m^{-1} \cdot K^{-1}$, which is higher than that of MS8M at 10 Pa, 0.0066 $W \cdot m^{-1} \cdot K^{-1}$. One possible origin of higher thermal conductivity is the pressure increase inside the panel. Presumably, outgas from aerogel (water and ethanol) and inflow of gas molecule through the joint and spacer raise the pressure inside the panel. From the pressure dependence of thermal conductivity for MS8M as shown in Fig.5 (a), thermal conductivity of aerogels increased with the residual gas pressure above threshold pressure. Judging from the thermal conductivity, the pressure inside the panel of 08-10 corresponds to 2×10^4 Pa.

Another possible reason is the increase in density due to densification of aerogels by external mechanical pressure. Fig.5 (b) shows the variation of thermal conductivity of aerogel with density at 10Pa. Thermal conductivity of aerogels has the tendency to increase with increasing density. The density with thermal conductivity of 0.0075 W/ (m·K) is 0.16 g/cm^3. When preparing the evacuated aerogel glazing, aerogel is compressed by atmospheric pressure, leading to densification of silica aerogel. Assuming that aerogels is compressed by applying of atmospheric pressure, the density of aerogel is calculated to be 0.156 g/cm^3, which is in good agreement with the data of thermal conductivity measurement.

4 Conclusion

Prototypes of evacuated aerogel glazing have been assembled in a vacuum chamber and its optical and thermal property was examined. The glazing prototypes with aerogel's thickness of 10 mm have a measured *U*-value of 0.62 W/ (m^2·K) and optical transmittance of 64%.

Reference

[1] P. W. Griffiths, P. C. Eames, T. J. Hyde, Y. Fang and B. Norton, *Journal of Solar Energy Engineering* **128** (2006), p. 199.

[2] R. E. Collins and T. M. Simko, *Solar Energy* **62** (1998), p. 189.

[3] J. M. Schultz and K. I. Jensen, *Vacuum* **82** (2008), p. 723.

[4] M. Kerker, The scattering of Light, Academic Press, New York (1969).

[5] C. G. Bohren and D. R. Hoffman, Absorption and Scattering of Light by Small Particles, Wiley, New York (1983).

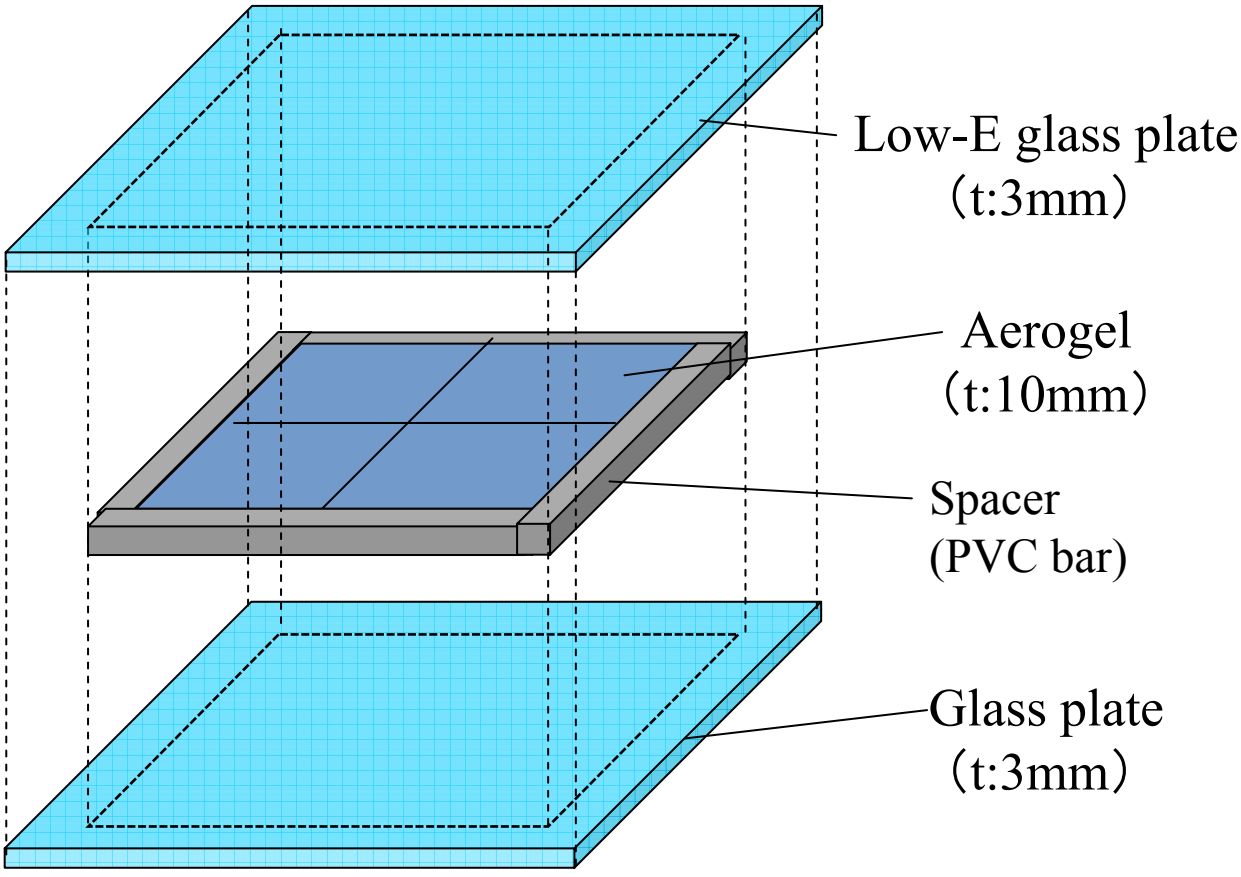

Figure 1: Schematic drawing of evacuated aerogel glazing

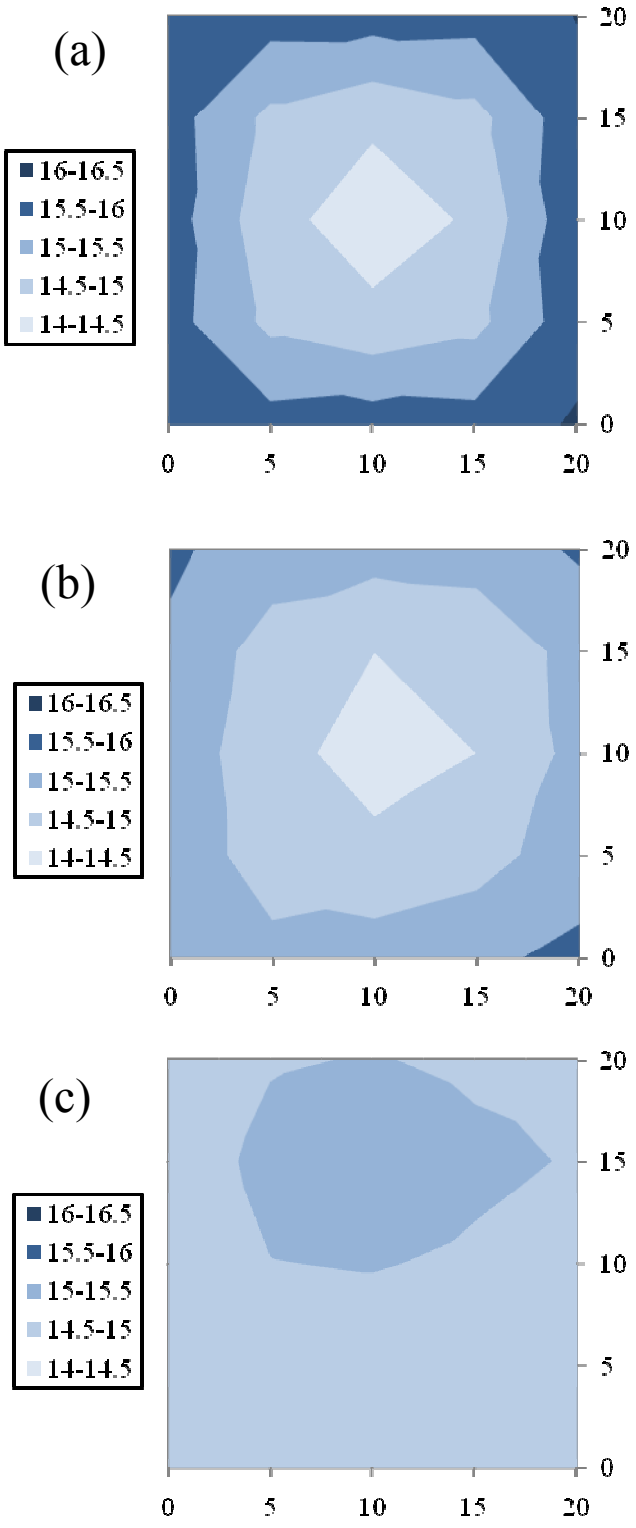

Figure 2: Contour lines of thickness for aerogel glazing using spacer thickness of (a) 10 mm, (b) 9.5 mm and (c) 9 mm

Table 1: *U*-value and thermal conductivity of aerogel glazing

Sample name	Thermal conductivity / $W \cdot m^{-1} \cdot K^{-1}$	U_{center} /$W \cdot m^{-2} \cdot K^{-1}$	Calculated aerogel Thermal conductivity / $W \cdot m^{-1} \cdot K^{-1}$
8-10	0.0115	0.623	0.0075
8-9.5	0.0122	0.677	0.0078
8-9	0.0122	0.684	0.0077

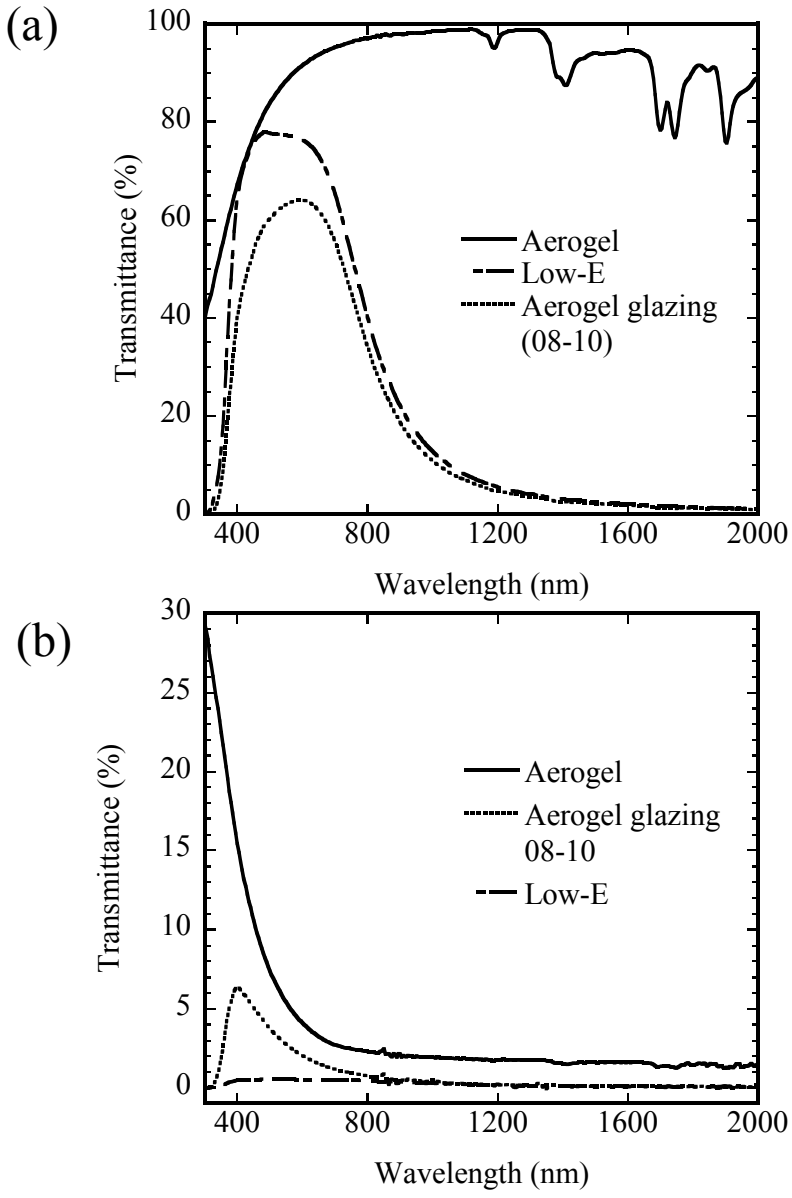

Figure 3: (a)direct-hemispherical transmittance of Aerogel glazing. For comparison, the curve of aerogel (MS8M) and Low-E glass was shown. (b) the diffusive transmission of aerogel, aerogel glazing and Low-E glass.

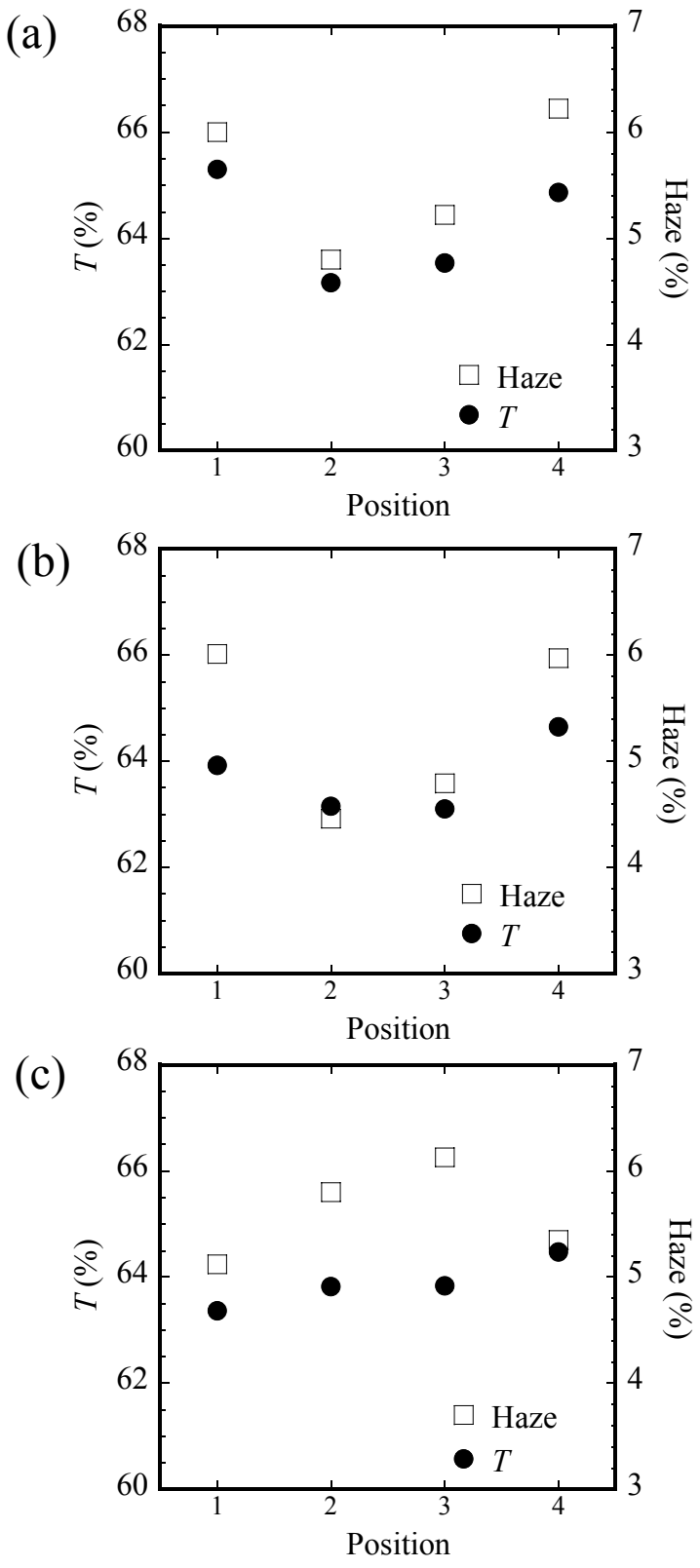

Figure 4: The transmission at 550 nm and haze ratio measured at regular interval on diagonal line with the spacer thickness of (a)10 mm, (b)9.5 mm (c) 9mm

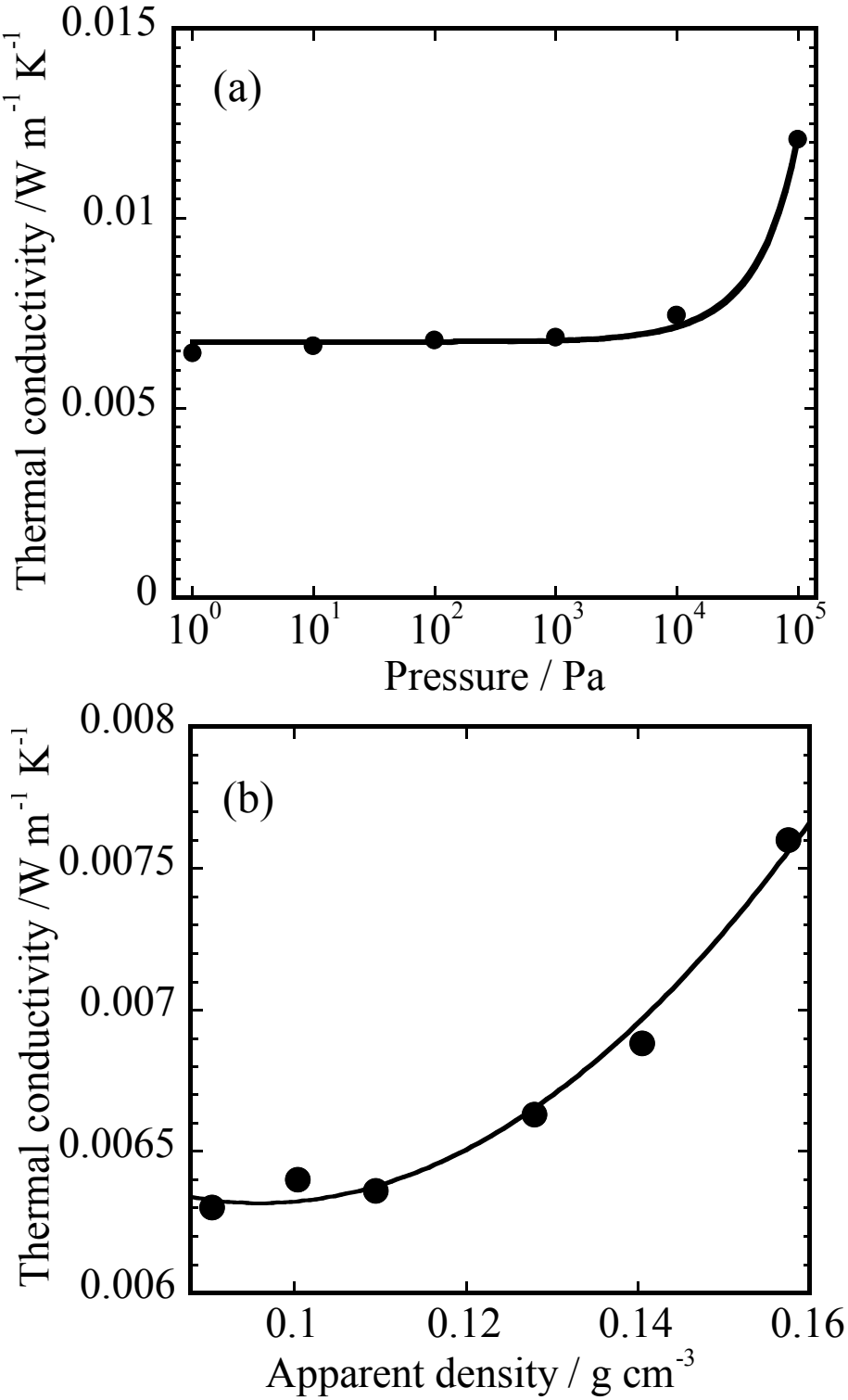

Figure 5: (a)pressure dependence of thermal conductivity for silica aerogels. (b) variation of thermal conductivity of aerogel s with density at 10Pa.

CHAPTER 5

Preparation and magnetic properties of oxygen deficient europium titanate thin films for the application of evacuated aerogel glazing

1. Introduction

It is known that tetravalent perovskite titanates show remarkable dielectric properties; for example, $BaTiO_3$ and $PbTiO_3$ are ferroelectric properties, and $SrTiO_3$ and $CaTiO_3$ are quantum paraelectrics. $EuTiO_3$ also has a perovskite structure with divalent Eu and tetravalent Ti, showing quantum paraelectric behavior. A difference between $EuTiO_3$ and other tetravalent perovskite titanates is the existence of localized magnetic ions in $EuTiO_3$; $EuTiO_3$ orders antiferromagnetically at 5.3 K [1]. When some of Eu^{2+} sites are replaced by the trivalent cations such as La^{3+} and Gd^{3+}, itinerant electrons are introduced into the triply degenerated t_{2g} orbitals of Ti 3d states. The itinerant carriers are strongly coupled with localized spin, leading to the ferromagnetic ordering of Eu spins [2]. Moreover, it has been reported that the dielectric constant of quantum paraelectrics $EuTiO_3$ depends strongly on a magnetic field [3]. In spite of such interesting properties, few studies have been reported on fabrication of $EuTiO_3$ thin films. One reason for this fact may be the difficulty in simultaneously controlling the valence states of Eu and Ti ions during the film growth. In this chapter, $EuTiO_{3-\delta}$ thin films are prepared on $SrTiO_3$ (STO) substrates by a pulsed laser deposition (PLD) method, and their magnetic properties are investigated.

2. Experimental procedure

$EuTiO_3$ thin films were deposited on STO (001) substrates by the PLD method. The STO substrates was subjected to ultrasonic agitation in distilled water for 1 min and subsequent annealed in air at 1000 ˚C for 2 h in order to obtain clean and well-defined surface. The $EuTiO_3$ ceramics target used for PLD was synthesized by sintering at 1200 ˚C under flowing gas of 95 vol% + 5 vol% H_2. The high density target and the flat surface STO substrate were set in a vacuum chamber with the background pressure of 10^{-6} Pa. A KrF exicimer laser (wavelength: 248 nm) was focused on the sintered $EuTiO_3$ target with a fluence of 2 J/cm^2 and a repetition rate of 5 Hz. The substrate temperature (T_s) was maintained at 700 ˚C during the deposition, and the oxygen pressure (P_{O2}) was varied between 10^{-6} and 10^{-4} Pa.

Crystal structure of films was investigated by x-ray diffraction (XRD) with Cu Kα radiation (SLX2500, Rigaku). The quantitative analysis of chemical composition and film thickness were performed by the Rutherford backscattering (RBS) using a 2.0 MeV He^{2+}. The measurements of magnetization were carried out using a superconducting quantum interference device (SQUID) magnetometer (MPMS2, Quantum Design).

3. Result and Discussion

Figure 1 shows RBS data on the thin film grown under P_{O2} = 1.0×10^{-6} Pa.

The open circles and the solid line indicate the experimental data and the best fit line from software SIMNRA program, respectively. The calculated cation ratio was Eu:Ti=1:1 which is in agreement with that of the target. Also, the calculated film thickness was ~ 100 nm.

Figure 2 shows out-of-plane XRD patterns for thin films grown at T_s = 700 ˚C under various P_{O_2}. The films grown under $P_{O_2} \leq 1.0\times10^{-4}$ Pa are composed of the (001)-oriented $EuTiO_3$ single phase with a perovskite-type structure. The lattice constant of film prepared under $P_{O_2} = 1.0\times10^{-6}$ Pa is 4.006 Å, which is much larger than that of bulk $EuTiO_3$ specimen prepared by solid state reaction (3.905 Å) [1]. According to conversion electron ^{151}Eu Mössbauer spectroscopy (not shown), almost all of the europium ions in the film existed as the divalent state. Hence, the increase in lattice constant along *c*-axis is mainly caused by the reduction of Ti^{4+} to Ti^{3+} during the deposition at lower P_{O_2} because the ion radius of Ti^{3+} (0.670 Å) is larger than that of Ti^{4+} (0.605 Å). Assuming that in-plane lattice parameter remains unchanged with the reduction of Ti^{4+} to Ti^{3+}, the chemical composition of film prepared under $P_{O_2} = 1.0\times10^{-6}$ Pa is calculated as $EuTiO_{2.87}$.

Figure 3 illustrates the temperature dependence of magnetization for the film grown under $P_{O_2} = 1.0\times10^{-6}$ Pa. The measurements were performed under field-cooled condition while an external magnetic field of 100 Oe was applied parallel to the film surface. In the figure, data for bulk $EuTiO_3$ specimen prepared by solid-state reaction are also shown for comparison. The bulk specimen orders antiferromagnetically at 5.5 K, while the magnetization of

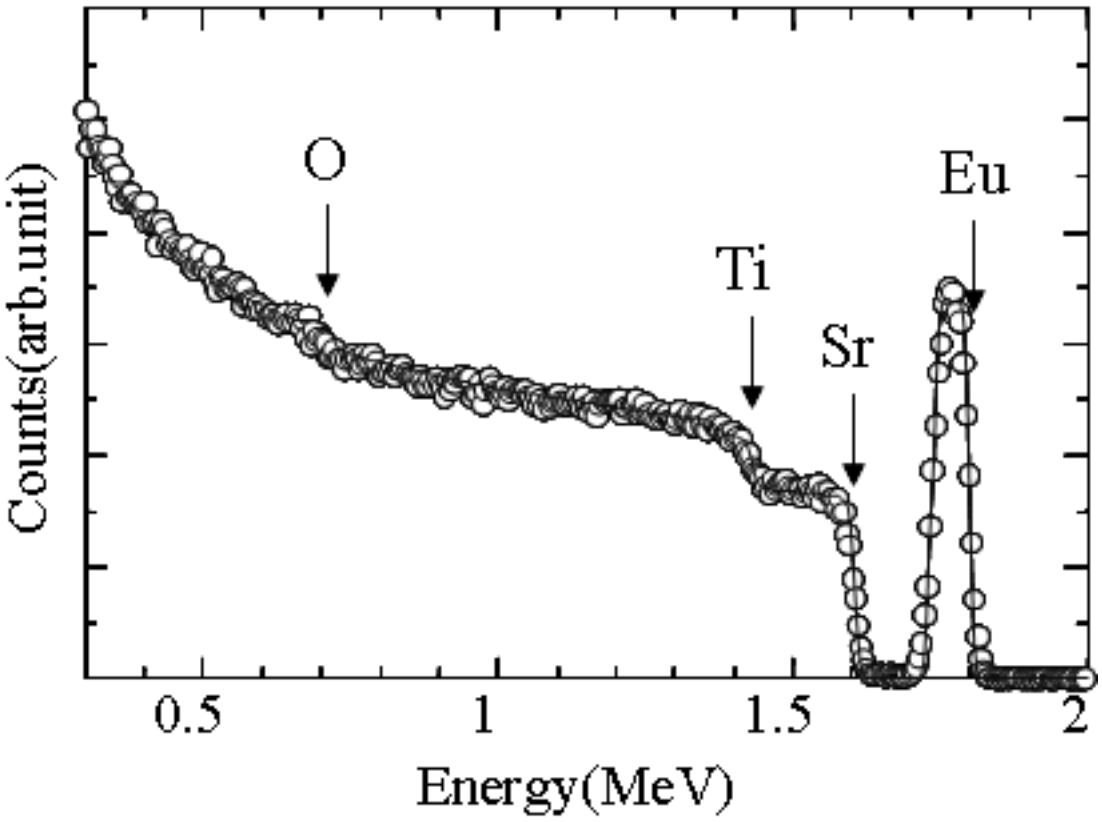

Figure 1: RBS scan of thin film grown under P_{O_2} = 1.0×10^{-6} Pa.

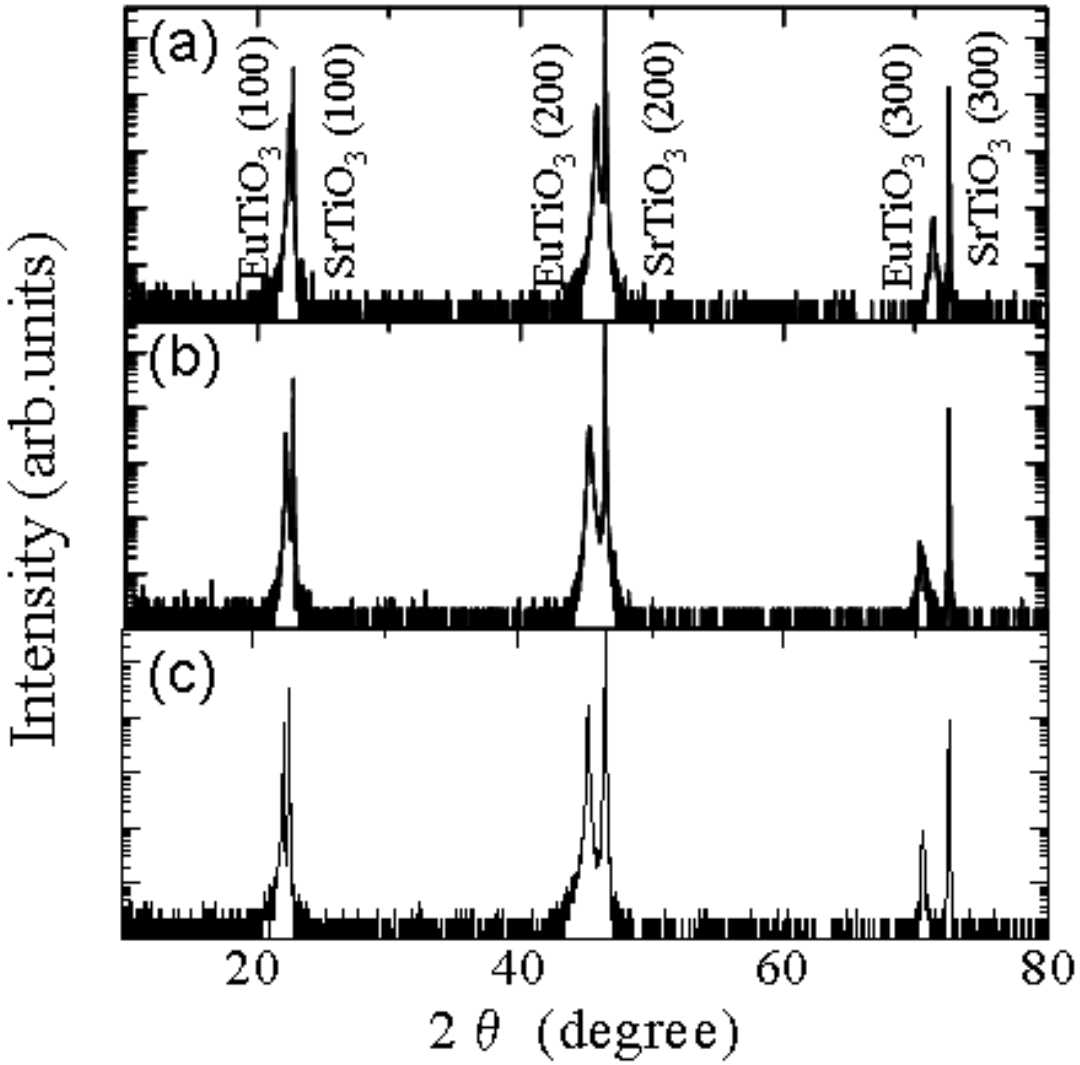

Figure 2: Out-of-plane XRD patterns for thin films grown under PO_2 = 1.0×10^{-4} Pa (a), 1.0×10^{-5} Pa (b), 1.0×10^{-6} Pa (c).

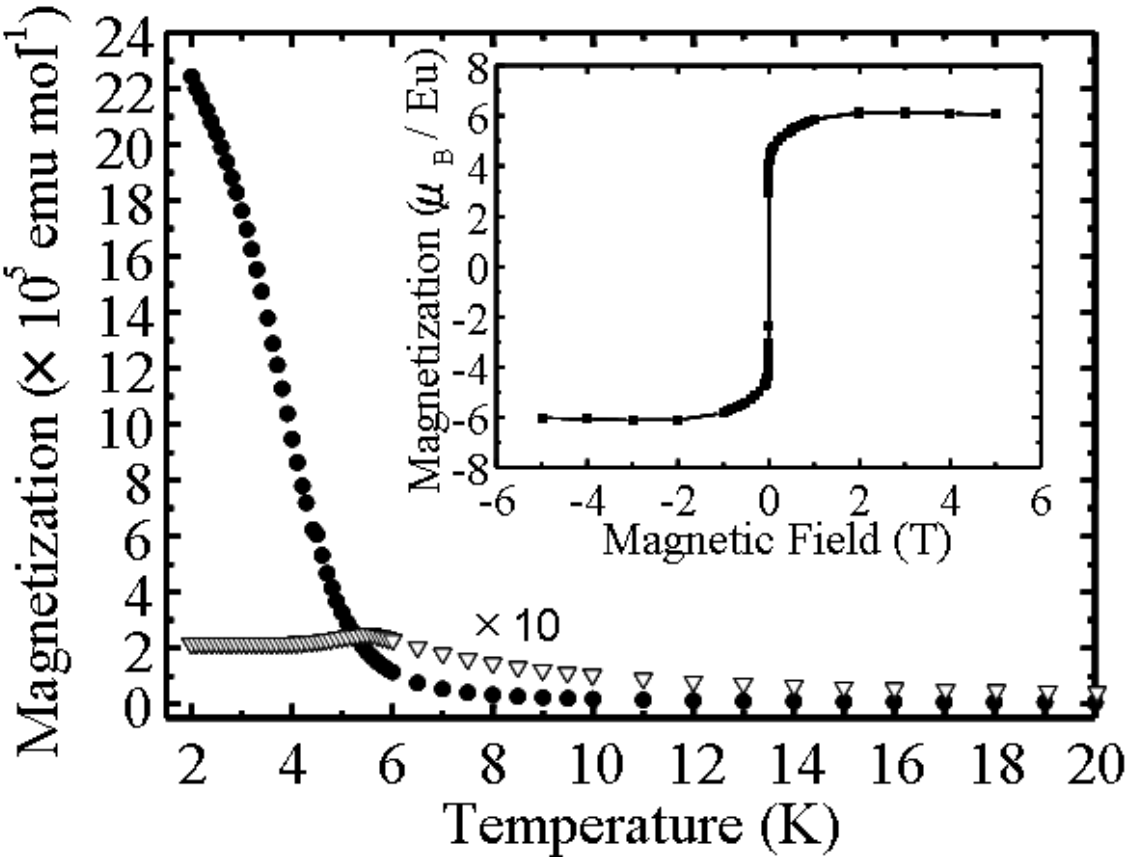

Figure 3: Temperature dependence of magnetization for the film grown under PO_2 = 1.0×10^{-6} Pa (closed circles). For comparison, data for bulk $EuTiO_3$ specimen prepared by solid-state reaction, which are magnified by a factor of 10, are also shown (open triangles). The inset shows the dependence of magnification at 2 K on external magnetic field.

oxygen deficient $EuTiO_{3-\delta}$ film shows a sharp increase at around 5 K indicating the ferromagnetic behavior. The magnetization at 2 K as a function of external magnetic field (see the inset of Fig.2) also confirms a ferromagnetic behavior. These results indicate that the oxygen deficient $EuTiO_{3-\delta}$ film is a ferromagnet with Curie temperature of 5 K.

In oxygen deficient $SrTiO_{3-\delta}$ [4] as well as La- and Gd- substituted $EuTiO_3$ [2], itinerant electrons are introduced into the triply degenerated t_{2g} orbital of Ti 3d states to bring about metallic conduction. A similar situation is expected for the present oxygen deficient $EuTiO_{3-\delta}$ film. One possible origin of the ferromagnetism is a Ruderman-Kittel-Kasuya-Yoshida (RKKY) interaction mechanism mediated by the Ti 3d itinerate electron as proposed for La- and Gd-substituted $EuTiO_3$ single crystal [2]. Under the deposition conditions at lower P_{O2} and higher T_s, however, the STO substrate is reduced to show electrical conduction, which make it difficult to evaluate only the transport properties such as $LaAlO_3$ (LAO) and $(LaAlO_3)_{0.3}(SrAl_{0.5}Ta_{0.5}O_3)_{0.7}$ (LSAT), which remains insulator even in the present deposition conditions, is now in progress to clarify the correlation between magnetism and transport properties.

4. Summary

$EuTiO_3$ thin films with a perovskite-type structure were epitaxially grown on STO (001) substrates at T_s =700 ˚C and $P_{O2} \leq 1.0\times10^{-4}$ Pa using the PLD method. The resultant films were identified as oxygen deficient $EuTiO_{3-\delta}$ ($\delta \leq 0.14$), exhibiting ferromagnetic behavior.

Reference

[1] Chia-Ling Chien, S. De Benedeti and F. De S. Barros, *Phys. Rev. B* **10** (1974), 3913

[2] T. Katsufuji and Y. Tokura, *Phys. Rev. B* **60** (1999), R15 021

[3] T. Katsufuji and H. Takagi, *Phys. Rev. B* **64** (2001), 054415

[4] W. Gong, H. Yun, Y. B. Ning, J. E. Greedan, W. R. Datars and C. V. Stager, *J. Solid State Chem*, **90** (1991) 320

CHAPTER 6

Preparation and magnetic properties of amorphous europium titanate thin films for the application of evacuated aerogel glazing

1. Introduction

Magnetic properties of oxide and fluoride glasses containing transition metal and/or rare-earth ions are interesting from a point of view of magnetism of solids where magnetic moments are randomly aligned. The spin glass (SG)-like magnetic transition of oxide and fluoride glasses has been extensively investigated so far [1-6]. In most insulating oxide and fluoride glasses, short-range antiferromagnetic (AFM) superexchange interactions via anions are dominant as demonstrated by the negative values of Weiss temperature (θ_W) [4-6]. The random distribution of magnetic ions, as well as the prevailing AFM interactions among magnetic ions, causes geometrical frustration in the alignment of magnetic moments at low temperatures, eventually leading to the SG transition. On the other hand, there are only a few reports concerning amorphous insulating compounds with positive values of θ_W, wherein ferromagnetic (FM) interactions are predominant [7,8]. Shoenes *et al.* reported that europium silicate glass with $Eu_{0.14}Si_{0.31}O_{0.55}$ composition where Eu^{2+} ions accounted for 27 % in cation ratio was paramagnet down to 1.5 K with a positive θ_W of 1 K in contrast to most amorphous oxides, although any explanation for the origin of the positive θ_W was not provided. Despite of the fascinating fact, the magnetic properties of Eu^{2+}-containing amorphous oxides

have been rarely investigated since then. Further studies on amorphous oxide systems with high concentration of Eu^{2+} are thus necessary to understand the magnetic interactions.

Recently, our research group have prepared various bulk oxide glasses with Eu^{2+} concentration of 10 to 45 % (in cation ratio) by using a melt-quenching method, and found that all the resultant glasses have positive θ_W values [9]. The result indicates that the FM interactions among Eu^{2+} ions are predominant in any oxide glasses containing high concentration of Eu^{2+} ions. In this work, it was focused on a binary europium titanate with an Eu^{2+} concentration of 50 % in cation ratio i.e., $EuTiO_3$. Although it is difficult to vitrify this system by the conventional melt-quenching technique, it was found accidentally, in the course of the research on thin film growth of crystalline $EuTiO_3$ using pulsed laser deposition (PLD) [10,11], that the glass formation could be achieved in the form of thin film through rapid cooling of the vapor phases.

In this chapter, it is particularly reported that the $EuTiO_3$ thin film prepared by PLD is identified to be amorphous by transmission electron microscope (TEM) observation as well as x-ray diffraction (XRD) analysis, and exhibits a positive value of θ_W, i.e., +8.7 K, which is the highest among the Eu^{2+}-containing amorphous solids reported so far. It has been also found the signature of a ferromagnetic-like transition at around 5 K for the amorphous $EuTiO_3$ thin films.

2. Experimental procedure

Amorphous $EuTiO_3$ thin films were deposited on silica glass substrates by a

PLD method. Polycrystalline $EuTiO_3$ was prepared by the solid-state reaction at 1400 ˚C for 12h under a flowing gas of 95 vol % Ar + 5 vol % H_2 and used as a target for PLD. The silica glass substrate and high-density target were set in a vacuum chamber with a base pressure of 10^{-6} Pa. A KrF excimer laser operated at a wavelength of 248 nm, a repetition frequency of 10 Hz, and an energy of 180 mJ was focused on the target. The film deposition was performed at room temperature under the base pressure (~10^{-6} Pa).

XRD measurements with Cu Kα radiation (Rint2500, Rigaku) and high-resolution TEM (HRTEM) observation (JEM-2100F, JEOL) were carried out to ascertain the amorphous nature of the resultant films. For the TEM observation, the cross-sectional specimen was prepared by an Ar ion milling at 5 kV using a liquid-nitrogen cooling system. The thickness of the thin film was examined by a surface profiler (Alpha-Step IQ, KLA-Tencor). Chemical composition of the films were examined by Rutherford backscattering (RBS) measurements and analyzed with the simulation program SIMNRA. In order to examine the valence state and local environment of Eu ions, ^{151}Eu conversion electron Mössbauer (CEM) spectroscopy was performed at room temperature using $^{151}Sm_2O_3$ with activity of 1.85 GBq as a 21.5 keV γ-ray source. The velocity calibration was done with the magnetic hyperfine spectrum of α-Fe foil obtained using ^{57}Co-doped Rh as a 14.4 keV γ-ray source. Mössbauer spectrum of EuF_3 was utilized as a standard of Doppler velocity. Magnetization measurements were carried out with a superconducting quantum interference device (SQUID) magnetometer (MPMS2, Quantum Design).

3. Results and Discussion

3.1 Structural characterization; XRD analysis, TEM observation, and CEM spectroscopy

Figure1 (a) shows the XRD pattern for the $EuTiO_3$ thin film prepared by PLD method. No sharp diffraction peaks ascribed to crystalline phases are observed, indicating the amorphous nature of as-deposited thin film. A broad peak around $2\theta = 20^\circ$ and a shoulder around $2\theta = 30^\circ$ arise from the silica glass substrate and thin film, respectively. The amorphous nature was further corroborated by HRTEM image and selected area electron diffraction (SAED) pattern, as depicted in Fig.1 (b). The molar ratio of Eu to Ti in the thin film was evaluated to be 1.01 through the analysis of RBS spectrum, which is very close to the target composition. The thickness of the thin film examined by a surface profiler is about 160 nm.

Figure 2 displays the room-temperature ^{151}Eu CEM spectrum for the amorphous $EuTiO_3$ thin film. The spectrum mainly consists of two peaks around -13 and 0.5 mm/s, which are assigned to the absorption bands due to Eu^{2+} and Eu^{3+}, respectively [12]. The intensity of absorption band is much stronger for Eu^{2+} than for Eu^{3+}, and the area of the former is about 97 % of the total absorption area. Given that the Debye temperature (θ_D) is usually lower for Eu^{2+} than for Eu^{3+} (e.g., θ_D =145 K and 261 K for Eu^{2+} and Eu^{3+} in a fluorozirconate glass, respectively [13]), it is expected that at least 97 % of Eu ions are present as the divalent state in the amorphous thin film. A close look at

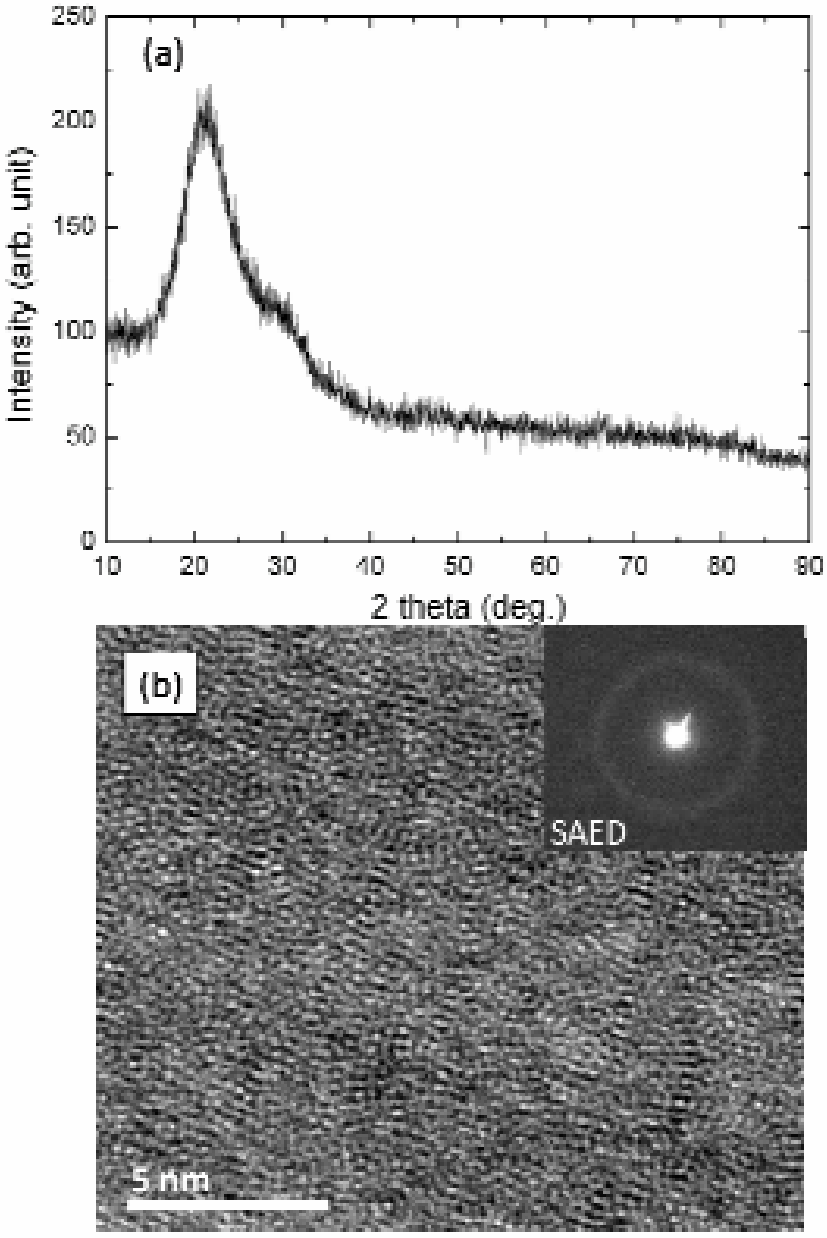

Figure 1. (a) XRD pattern of amorphous $EuTiO_3$ thin film prepared by the PLD method. (b) High-resolution transmission electron micrograph of the amorphous $EuTiO_3$ thin film. The inset shows SAED pattern.

Fig. 2 reveals that the Eu^{2+} absorption band is split due to the quadrupole interactions between the electric field gradient and the electric quadrupole moment of ^{151}Eu nucleus [12]. Therefore, we have analyzed the Eu^{2+} absorption band with the method developed by Shenoy and Dunlap [14]. For ^{151}Eu, I^* =7/2, I =5/2, and Q_e/Q_g = 1.34 [15], and thus, there are 12 possible transitions in the presence of quadrupole interactions. The γ-ray resonance energy between (I^*, I_z^*) and (I, I_z) is given by

$$R(I_z^*, I_z) = eV_{zz}[Q_eP(I^*, I_z^*) - Q_gP(I, I_z)] + \delta, \quad (1)$$

where e is the elementary charge, V_{zz} is the electric field gradient in the direction z, Q_e and Q_g are excited- and ground-state nuclear quadrupole moments, respectively, I^* and I are excited- and ground-state nuclear spins, respectively, I_z^* and I_z are z projections of excited- and ground-state nuclear spins, respectively, and δ is the isomer shift. $P(I^*, I_z^*)$ and $P(I, I_z)$ are written as

$$P(I, I_z) = \sum_{N=0}^{4} a_N(I, I_N)\eta^N \quad , \quad (2)$$

where η is the asymmetry parameter of the electric gradient, and $a_N(I,I_z)$ is the eigenvalue coefficient (see Ref. 14). The transmission intensity is expressed by

$$A(I^*, I_z^*, I, I_z) = \sum_{N=0}^{4} b_N(I^*, I_z^*, I, I_z)\eta^N \quad , \quad (3)$$

where $b_N(I^*,I_z^*,I,I_z)$ is the intensity coefficient (see Ref. 14). In the calculation of theoretical spectrum for Eu^{2+} absorption band, we assume that the absorption line corresponding to each transition is represented by a Lorentzian with a full width at half maximum of γ, which reflects the site-to-site variation of Eu^{2+}.

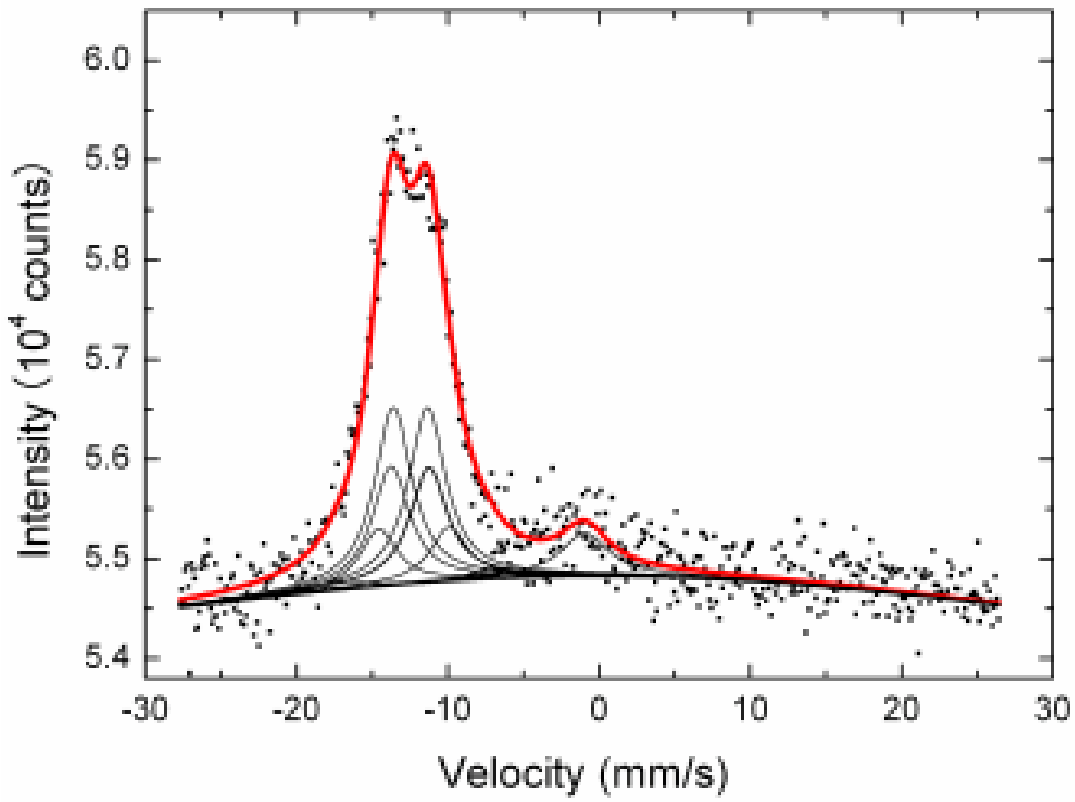

Figure 2: ^{151}Eu conversion-electron Mössbauer spectrum of amorphous $EuTiO_3$ thin film at room temperature. The closed squares represent the experimental data, and the solid line is the fit of theoretical curve using Eq. (1)-(3). The component line corresponding to the 12 transitions are also shown for the Eu^{2+} absorption peak at around -12 mm/s.

The magnetic hyperfine is also neglected interactions because the amorphous thin film is paramagnetic at room temperature as described below. For the Eu^{3+} absorption band, a single Lorentzian was simply used to reproduce the spectral shape due to the poor spectral resolution. The background curve was corrected with the equation proposed by Marshall *et al.* [16]. The fit of theoretical curve to the experimental spectrum yields δ = -12.45 mm/s, $eV_{zz}Q_g$ = -14.06 mm/s, η = 0.86, and γ = 3.02 mm/s. For oxide solids containing Eu^{2+}, the δ value reflects the electron density at the nucleus and can be a measure of the covalency of Eu^{2+}-O bond and/or the coordination number of oxide ions for Eu^{2+} [17]. The value of δ for the amorphous $EuTiO_3$ thin film is comparable to that for crystalline $EuTiO_3$ (-12.5 mm/s), indicating that the average coordination number of Eu^{2+} in amorphous $EuTiO_3$ thin films is 12. Moreover, the non-zero quadrupole interaction ($eV_{zz}Q_g$ = -14.06 mm/s) and non-zero asymmetry parameter (η = 0.86) indicate the deviation from cubic symmetry and the absence of axial symmetry for the coordination structure around Eu^{2+} in the amorphous thin film. In the case of Eu^{2+}, the quadrupole interaction parameter reflects the electric field gradient caused by the surrounding ligands, because, in the case of Eu^{2+} with $^8S_{7/2}$ ground state, resultant zero orbital angular momentum leads to no valence contribution [17]. The magnitude of $eV_{zz}Q_g$ for the amorphous $EuTiO_3$ thin film is comparable to those for the Eu^{2+}-comtaining bulk oxide glasses as reported previously ($eV_{zz}Q_g$ = -11.20 ~ -17.98 mm/s) [17,18].

3.2 Magnetic properties

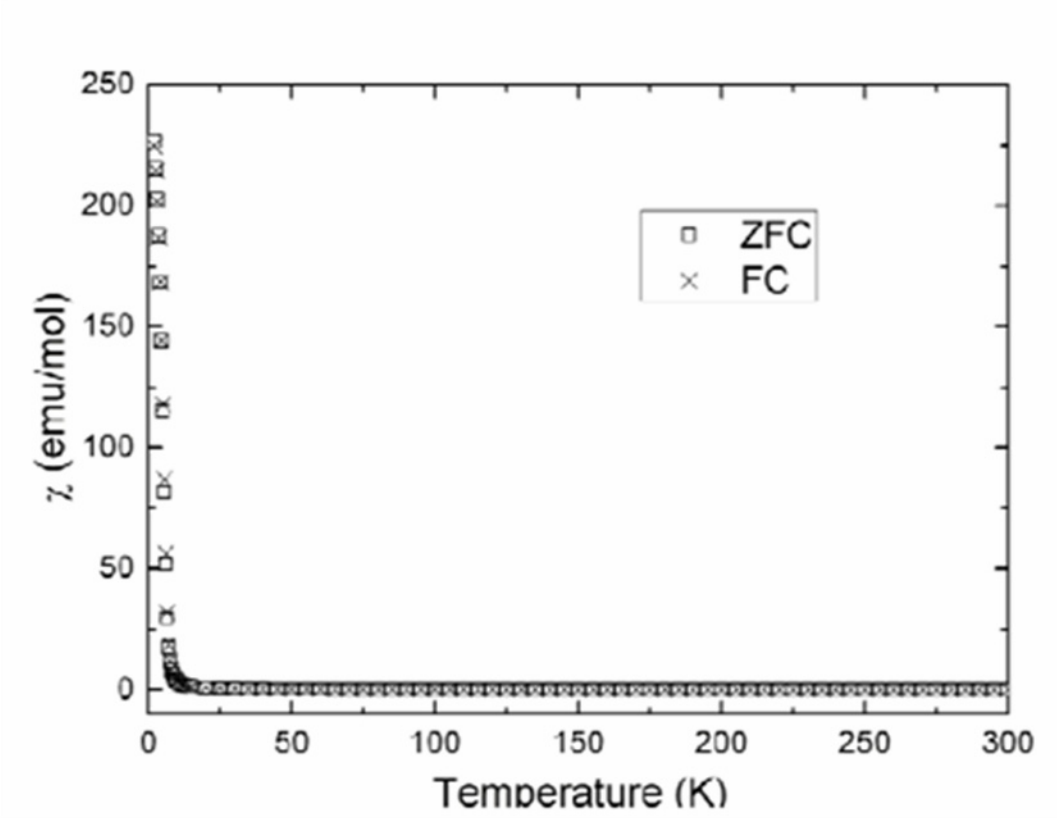

Figure 3: Temperature dependence of magnetic susceptibility, $\chi(T)$, of amorphous $EuTiO_3$ thin film at an external magnetic field of 100 Oe in a temperature region of 2 to 300 K. The crosses and open squares represent the field-cooled (FC) and zero-field cooled (ZFC) processes, respectively.

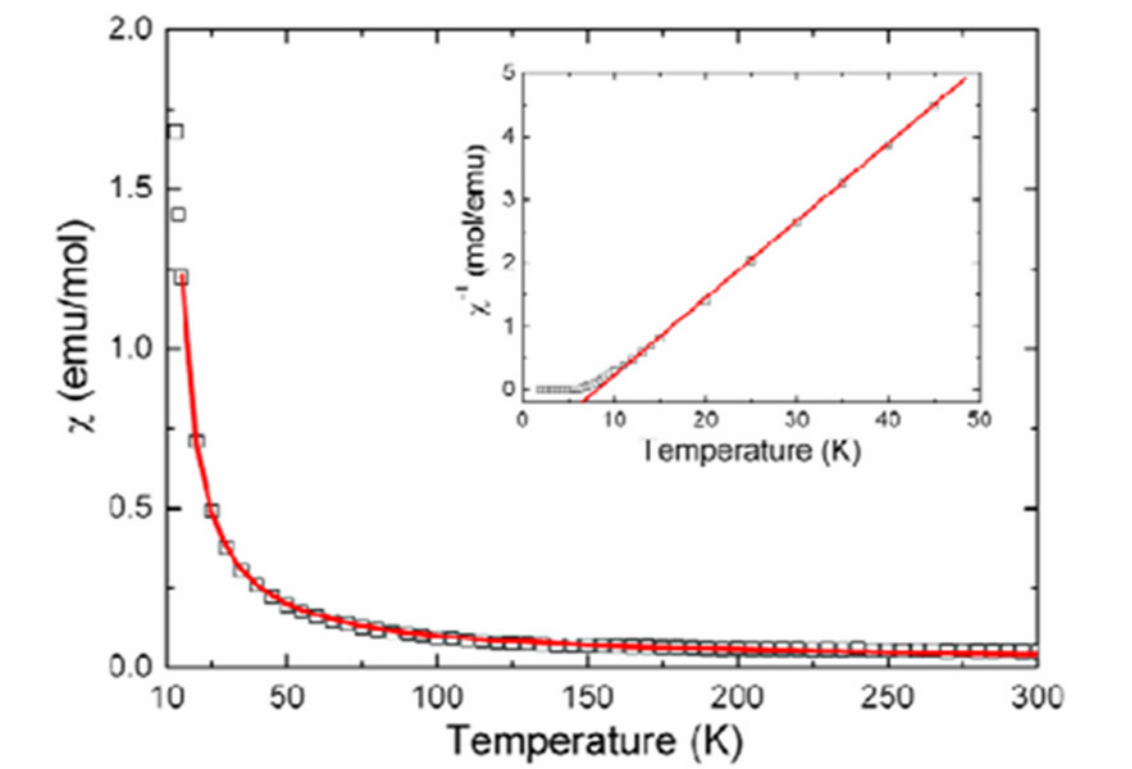

Figure 4: $\chi(T)$ curve (open squares) in the high-temperature region (10 K< T<300 K). The solid line is drawn by fitting the experimental data with the theoretical derived from Eq. (4)-(6). The inset shows the $\chi^{-1}(T)$ curve (open squares) as well as the fit of Curie-Weiss law to the experimental data (solid line).

Figure 3 shows the temperature dependence of magnetic susceptibility, $\chi(T)$, for the amorphous $EuTiO_3$ thin film measured at temperatures of 2 to 300 K. Both zero-field-cooling (ZFC) and field-cooling (FC) processes were carried out while an external magnetic field (H) of 100 Oe was applied along the out-of plane axis. No detectable difference in χ-T curve between the ZFC and FC measurements is observed in the whole temperature region. As depicted in the inset of Fig. 4, a linear relation is observed in the χ^{-1}-T curve above 10 K and is describable in terms of the Curie-Weiss law;

$$\chi = \frac{N_A \mu_{\mathrm{eff}}{}^2}{3k(T-\theta_w)} \quad , \tag{4}$$

where N_A is the Avogadro's number, μ_{eff} is the effective magnetic moment of Eu^{2+}, k is the Boltzman constant, and θ_w is the Weiss temperature. The intercept of the solid line shown in the inset of Fig. 4 is positive, suggesting that ferromagnetic interactions are dominant in the amorphous $EuTiO_3$ thin film. The upward deviation of χ^{-1}-T curves from the Curie-Weiss law, as observed at temperatures below 10 K, is indicative of the emergence of short-range ferromagnetic correlation at low temperatures. More precise analysis of the χ-T curve has been made in consideration of the participation of Eu^{3+} ions. The molar susceptibilities of the thin film can be expressed by

$$\chi_{\mathrm{mol}} = n\,\chi_{\mathrm{mol}}(Eu^{2+}) + (1\text{-}n)\,\chi_{\mathrm{mol}}(Eu^{3+}) + \chi_0 \,, \tag{5}$$

where n is the molar ratio of Eu^{2+} to the total europium ion, and χ_0 is the temperature-independent term. The magnetic susceptibility of Eu^{2+}, $\chi_{\mathrm{mol}}(Eu^{2+})$, can be caclculated by using the Curie-Weiss law described in Eq. (4). The ground state ${}^7F_0$ of Eu^{3+} is nonmagnetic, and the excited states ${}^7F_J$ (J=1, 2, ⋯, 6)

are close enough to give energy differences comparable to kT at room temperature. Taking into account the first three excited states, the magnetic susceptibilities of Eu^{3+}, $\chi_{mol}(Eu^{3+})$, can be written as [19]

$$\chi_{mol}(Eu^{3+}) = \frac{N_A \mu_B{}^2}{3kT} \cdot \frac{\frac{24}{a} + \left(13.5 - \frac{1.5}{a}\right)e^{-a} + \left(67.5 - \frac{2.5}{a}\right)e^{-3a} + \left(189 - \frac{3.5}{a}\right)e^{-6a}}{1 + 3e^{-a} + 5e^{-3a} + 7e^{-6a}}, \quad (6)$$

where $a = \lambda/kT$ is the ratio of the multiplet width (λ is a spin-orbit coupling constant) to the thermal energy. Eq. (6) indicates the contributions from the Van Vleck paramagnetism of Eu^{3+} and the Curie paramagnetism of the excited states of Eu^{3+}. If we take λ = 370 cm^{-1} as reported for $EuAlO_3$ [20] and μ_{eff} = 7.97μ_B which is the theoretical value, the χ-T curve in the paramagnetic region (> 10 K) is reasonably reproducible by the combination of Eq. (4)-(6) [see Fig. 3 (b)], which gives n =0.96 and θ_w =+8.7 K. The value of n coincides with that obtained from the Mössbauer effect measurement. The value of θ_w for the amorphous $EuTiO_3$ thin film is much higher than that of the binary silicate glass with $Eu_{0.14}Si_{0.31}O_{0.55}$ composition (θ_w = +1 K) reported by Shoenes *et al.*, presumably due to the higher concentration of Eu^{2+} ions in the present thin film. Here, it should be noted that there are only a few reports on insulating oxide and fluoride glasses with positive θ_w values, since most magnetic insulators demonstrate negative values of θ_w due to the predominant AFM interactions.

Figure 5 displays the χ-T curves in the low temperature region for the amorphous $EuTiO_3$ thin films. The χ value starts to increase rapidly as the film is cooled below 7 K. The inset of Fig. 5 shows the H-dependence of magnetization at 2 K. The M-H curve increases rapidly with increasing H in the

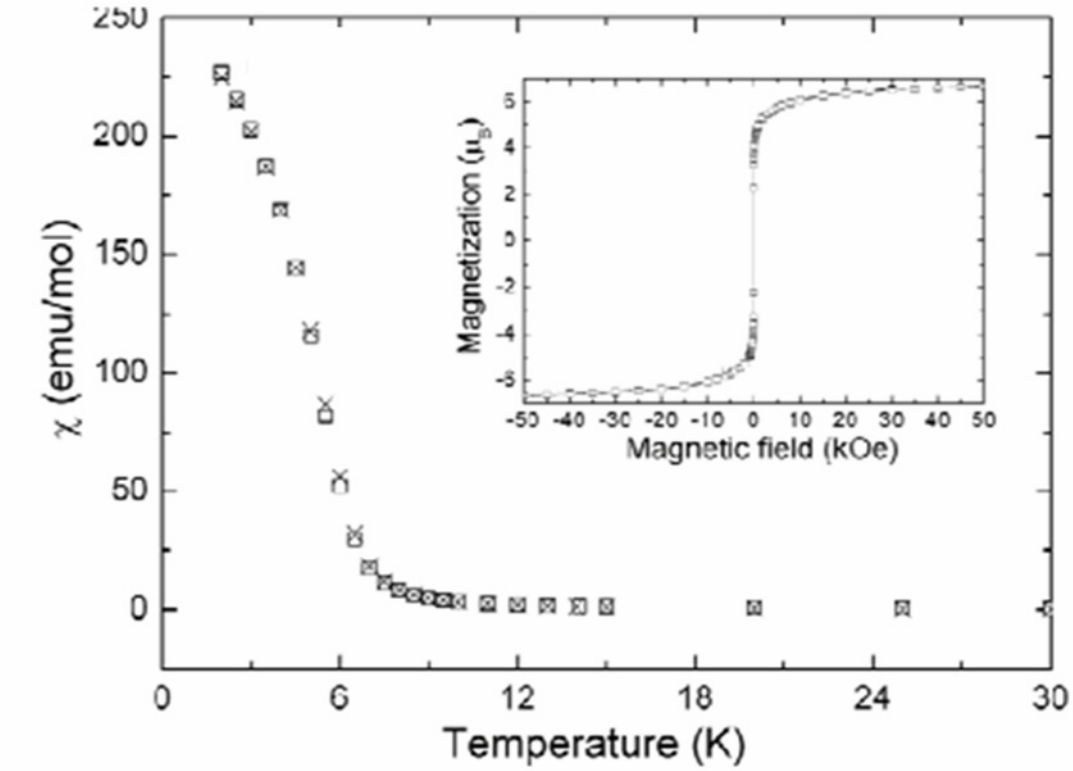

Figure 5: Enlarged view of the low-temperature region in the $\chi(T)$ depicted in Fig. 3. The inset shows field-dependence of magnetization at 2 K (open squares) and guide for the eye (solid line).

low-field region and tends to be saturated at a field higher than 1 T. The saturation magnetization reaches 6.68 μ_B/Eu, and is very close to the full spin moment of Eu^{2+} (7 μ_B), which again confirms that almost all of the Eu ions exist as Eu^{2+} in the present thin film. A close inspection of Fig. 5 reveals the presence of an inflection point in the χ-*T* curve at around 5 K, implying the presence of a ferromagnetic-like transition. A similar result was obtained for crystalline $EuTiO_3$ thin film grown on $SrTiO_3$ substrate where strain-induced ferromagnetism was observed [11]. Further characterization is necessary to better understand the low-temperature magnetic anomaly in this amorphous oxide system, which will be carried out in the near future.

4. Conclusion

Amorphous $EuTiO_3$ thin film has been deposited on silica glass substrate by the PLD method, and its structural and magnetic properties were examined. The resultant thin film was confirmed to be amorphous by XRD pattern, HRTEM image, and SAED pattern. ^{151}Eu CEM spectrum indicates that at least 97 % of Eu ions are present as the divalent state in the thin film. The amorphous $EuTiO_3$ thin film has a positive Weiss temperature (θ_w =8.7 K), indicating that the predominant magnetic interactions among Eu^{2+} ions are ferromagnetic. The ferromagnetic-like transition is also observed at around 5 K, although further investigation is required to clarify the nature of low-temperature magnetic ordering.

Reference

[1] H. Akamatsu, K. Tanaka, K. Fujita and S. Murai, *Phys. Rev. B* **74** (2006), 012411

[2] M. D. Mukadam, S. M. Yusuf, P. Sharma, S. K. Kulshreshtha and G. K. Dey, *Phys. Rev. B* **72** (2005), 174408

[3] P.Beauvillain, C. Dupas, J. P. Renard and P. Veillet, *Phys. Rev. B* **29** (1984), 4086

[4] J. L. Shaw, A.C. Wright, R.N. Sinclair, G. K. Marasinghe, D. Holland, M. R. Lees and C. R. Scales, *J. Non-Cryst. Solids* **345** (2004) 245

[5] K. Tanaka, H. Akamatsu, S. Nakashima and K. Fujita, *J. Non-Cryst. Solids* **354** (2008) 1346

[6] H. Akamatsu, K. Tanaka, K. Fujita and S. Murai, *J. Phys. C: condensed Matter* **20** (2008) 235216

[7] F. J. Litterst, *J. phusique* **36** (1975) L197

[8] J. Shoenes, E. Kaldis, W. Thöni and P. Wachter, *Phys. Stat. Sol*, **51** (1797) 173

[9] H. Akamatsu, K. Fujita, S. Murai and K. Tanaka, *Phys. Rev. B* **81** (2010), 014423

[10] K. Kugimiya, K. Fujita, K. Tanaka and K.Hirao, *J. Magn. Magn. Mater.* **310** (2007) 2268

[11] K. Fujita, N. Wakasugi, S. Murai, Y. Zong and K. Tanaka, *Appl. Phys. Lett.* **94** (2009) 062512

[12] F. Grandjean and G. J. Long, *Mössbauer Spectroscopy Applied to*

Inorganic Chemistry (Plenum Press, New York, 1989) p 513-597

[13] J. M. D. Coey, A. McEvoy and M. W. shafer, *J. Non-Cryst. Solids* **43** (1981) 387

[14] G. K. Shenoy and B. D. Dunlap, *Nucl. Instrum. Methods* **71** (1969) 285

[15] C. L. Chien, S. DeBenedetti and F. De Barros, *Phys. Rev. B* **10** (1974) 3913

[16] S. W. Marshall, J. A. Nelson and R. L. Wilenzick, *Commun. ACM* **8** (1965) 313

[17] K. Fujita, K. Tanaka, K. Hirao and N. Soga, *J. Am. Ceram. Soc.* **81** (1998) 1845

[18] K. Tanaka, K. Fujita, N. Matsuoka, K. Hirao and N. Soga, *J. Mater. Res.* **13** (1998) 1989

[19] J. H. Van Vleck, *The Theory of Electric and Magnetic Susceptibilities* (Clarendon, Oxford, 1932) p.248

[20] L. M. Homes, R. Sherwood and L. G. Van Uitert, *Phys. Rev.* **178** (1969) 576

SUMMARY

In this thesis, thermal and optical property of evacuated aerogel glazing, which is the candidate for the next generation window, was investigated. Thermal and optical and mechanical property of aerogel, which is core material of evacuated aerogel glazing, was also evaluated. Generally, the glass used for aerogel glazing is coated by functional thin films such as heat reflecting film, electrochromic film, thermalchromic film and magnetic film. It has been demonstrated that amorphous $EuTiO_3$ films as well as oxygen deficient $EuTiO_3$ epitaxial films showed ferromagnetic-like behavior. The results obtained in this study are summarized as follows.

In Chapter 1, thermal conductivity for porous silica powder and transparent silica aerogel as a function of gas pressure was evaluated. It was clarified that thermal conductivity of the porous ceramic material was lowered than that of simple vacuum at lower vacuum region (higher gas pressure), indicating that the porous ceramic materials had an advantage for the application of thermal insulator.

In Chapter 2, transparent aerogels were prepared using commercially available silicon oligomer and methyltrimethoxysilane precursor to examine their mechanical and optical properties. The preparation of highly transparent silica-based aerogel was successfully achieved by tuning the starting composition and appropriate treatment.

In Section 2.1, transparent aerogels using silicon oligomer as precursor have been synthesized and the effect of the concentration of water and ethanol on

optical and mechanical property of resultant aerogel was investigated. Total pore volume and density measurement confirmed that the density of aerogel decreased with increasing the concentration of ethanol and water. FE-SEM observation indicated that aerogels from silicon oligomer possessed skeletons of aggregated globules and small pores. With decreasing the concentration of ethanol at starting condition, the microstructure of aerogels became slightly homogeneous, which affected optical transmittance and uniaxial compression behavior. With increasing H_2O/Si ratio, the domain size of aerogel became finer, leading to higher optical transparency as high as 92 % at 550 nm for 1cm thick aerogel and stiffer character against the uniaxial compression.

In Section 2.2, transparent silica-based aerogels using methyltrimethoxysilane and non-ionic surfactant by supercritical drying process have been prepared. Non-ionic surfactant was successfully used for forming wet-gels composing of the three dimensional-connected thinner fibers of silica skeletons with ~ 10 nm in diameter. It was found that the surfactants were effectively removed from the wet-gels by soaking in hot water without changing the gel size, resulting in the preparation of high transparent aerogels after supercritical drying. The transparency of aerogels increased up to 65% at 400 nm wavelength for 10 mm thickness of sample composing of the fiber skeletons or pores with ~ 15 nm of diameter. The formation process of wet- and aero-gels using the small angle X-ray scattering experiments has been also elucidated.

In Chapter 3, Silica aerogels with different density and thickness have been prepared by controlling the starting composition and influence of density and thickness on thermal conductivity under evacuated and atmospheric condition

was examined. FE-SEM observation and nitrogen adsorption confirmed that aerogel with different density had similar pore diameter. Absorption coefficient calculated by optical transmittance revealed that aerogels with different thickness had similar morphology. Measurement of thermal conductivity of aerogels indicate non-evacuated and evacuated aerogel showed minimum value at the density of 0.14 and 0.10 $g \cdot cm^{-3}$, respectively. For evacuated aerogel as well as non-evacuated aerogel, thickness dependence of thermal conductivity was observed, which was attributed to low extinction coefficient of silica aerogel.

In Chapter 4, Prototypes of evacuated aerogel glazing have been assembled in a vacuum chamber and its optical and thermal property was examined. The glazing prototypes with aerogel's thickness of 10 mm had a measured *U*-value of 0.62 W/ ($m^2 \cdot K$) and optical transmittance of 64%.

In Chapter 5, $EuTiO_3$ thin films with a perovskite-type structure were epitaxially grown on STO (001) substrates at T_s =700 ˚C and $P_{O_2} \leq 1.0 \times 10^{-4}$ Pa using the PLD method. The resultant films were identified as oxygen deficient $EuTiO_{3-\delta}$ ($\delta \leq 0.14$), exhibiting ferromagnetic behavior.

In Chapter 6, amorphous $EuTiO_3$ thin film has been deposited on silica glass substrate by the PLD method, and its structural and magnetic properties were examined. The resultant thin film was confirmed to be amorphous by XRD pattern, HRTEM image, and SAED pattern. ^{151}Eu CEM spectrum indicates that at least 97 % of Eu ions are present as the divalent state in the thin film. The amorphous $EuTiO_3$ thin film has a positive Weiss temperature (θ_w =8.7 K), indicating that the predominant magnetic interactions among Eu^{2+} ions are ferromagnetic. The ferromagnetic-like transition is also observed at around 5 K,

although further investigation is required to clarify the nature of low-temperature magnetic ordering.

LIST OF PUBLICATIONS

CHAPTER 1

“Development of silica porous powder and aerogel for the application of thermal insulator”

Kazuma Kugimiya, Mitsue Ogawa, Hideaki Matsubara, and Kazuyuki Hirao

IOP conference series; Materials Science and Engineering, in print

“Fabrication of novel heat insulator using porous ceramics materials”

Kazuma Kugimiya, and Hideaki Matsubara

Ceramics engineering and science proceedings, **31**, 91-98 (2010)

CHAPTER 2

“Synthesis and characterization of transparent silica aerogels using silicon oligomer”

Kazuma Kugimiya, Hideaki Matsubara, Sakae Tanemura, and Kazuyuki Hirao

Journal of Sol-Gel Science and Technology, submitted

“Synthesis and characterization of transparent silica-based aerogels using methyltrimethoxysilane precursor”

Masayuki Nogami, Shohei Hotta, Kazuma Kugimiya, and Hideaki Matsubara

Journal of Sol-Gel Science and Technology, 56, 107 (2010)

CHAPTER 3

“Thermal conductivity of silica aerogel under evacuated condition”

Kazuma Kugimiya, Mitsue Ogawa, and Hideaki Matsubara

IOP conference series; Materials Science and Engineering, in print

CHAPTER 4

“Fabrication and characterization of evacuated aerogel glazing”

Kazuma Kugimiya, Yoshitaka Matsuyama, Hideaki Matsubara, and Nobuhiro Shinohara

Journal of Non-Crystalline Solids, submitted

CHAPTER 5

“Preparation and magnetic properties of oxygen deficient $EuTiO_{3-\delta}$ thin films”

Kazuma Kugimiya, Koji Fujita, Katsuhisa Tanaka, and Kazuyuki Hirao

Journal of Magnetism and Magnetic Materials, **310**, 2268-2270 (2007)

CHAPTER 6

“Preparation and magnetic properties of amorphous $EuTiO_3$ thin films”

Yanhua Zong, Kazuma Kugimiya, Koji Fujita, Hirofumi Akamatsu, Kazuyuki Hirao, and Katsuhisa Tanaka

Journal of Non-Crystalline Solids, **356**, 2389-2393 (2010)

Acknowledgement

The present thesis has been carried out under the direction of Professor Kazuyuki Hirao at Graduate School of Engineering, Kyoto University.

First of all, the author wishes to express his sincere gratitude to Professor Kazuyuki Hirao for his continuous encouragement and valuable advice all through the duration of the present work. The author is also grateful to Professor Katsuhisa Tanaka and Professor Kiyotaka Miura for guidance and discussion in preparation of the present thesis. The author also appreciates Dr. Hideaki Matsubara and Dr. Sakae Tanemura for informative discussions. Coutinuous encouragement given by Professor Setsuhisa Tanabe and Associate Professor Kazuki Nakanishi is also appreciated. The author is greatly indebted to Associate Professor Koji Fujita for his informative discussion, helpful advice, and sincere supports. The author also thanks Dr. Kazuyoshi Kanamori, Dr. Masayuki Nishi, Mr. Shunsuke Murai, Dr. Seisuke Nakashima, Dr. Hajime Hojo, Dr. Junko Konishi, and Dr. Haruko Saito for helpful assistance.

Experimental supports for Mössbauer spectroscopy measurements by Dr. Mitsuo Tosaki are greatly acknowledged. The author would like to thank Dr. Hidetsugu Tsuchida and Professor Akio Ito for RBS measurements. The author also thanks Dr. Hirofumi Akamatsu, Mrs. Sakiko U. Goto and Dr. Chiwon Moon for their experimental supports and fruitful discussions.

Hearty thanks are made to all the students of Hirao's laboratory, Tanaka's laboratory, and Tanabe's laboratory for their collaboration and everyday activities. Especially his colleagues, Mr. Kohei Higashi, Mr. Takayuki Hirao, and Mr.

Yoshitaka Suzumura contributed to my happiest time. The author also would like to thank the member of JFCC and NEDO project of ”Development of multi-ceramic film for new thermal insulator” for helpful assistance and fruitful discussion.

Finally, the author would like to express his sincere gratitude to his parents Kazuo Kugimiya and Machiko Kugimiya, for their understanding, supports, and hearty encouragements.

Nagoya, 2011 Kazuma Kugimiya